A Comprehensive Model for Filtration and Adsorption of Intermediate Nanoparticles

by

Maryam Razavi

A thesis
presented to the University of Waterloo
in fulfillment of the
thesis requirement for the degree of
Doctor of Philosophy
in
Mechanical and Mechatronics Engineering

Waterloo, Ontario, Canada, 2020

Examining Committee Membership

The following served on the Examining Committee for this thesis. The decision of the Examining Committee is by majority vote.

External Examiner	Dr. Hongbo Zeng Professor, Department of Chemical and Materials Engineering University of Alberta
Supervisors	Dr. Zhongchao Tan Professor, Department of Mechanical & Mechatronics Engineering University of Waterloo
	Dr. Zhao Pan Assistant Professor, Department of Mechanical & Mechatronics Engineering University of Waterloo
Internal Member	Dr. Ehsan Toyserkani Professor, Department of Mechanical & Mechatronics Engineering University of Waterloo
	Dr. John Wen Professor, Department of Mechanical & Mechatronics Engineering University of Waterloo
Internal-external Member	Dr. Zhongwei Chen Professor, Department of Chemical Engineering University of Waterloo

AUTHOR'S DECLARATION

I hereby declare that I am the sole author of this thesis. This is a true copy of the thesis, including any required final revisions, as accepted by my examiners.

I understand that my thesis may be made electronically available to the public.

Abstract

Nanoparticles have been extensively studied in environmental research because of their great impact on human health and the environment. Airborne particles are recognized as the second largest risk factor for non-communicable diseases worldwide in 2018 after tobacco smoking, which also is associated with inhaled particles. Intermediate particles, which bridge gas molecules and aerosol particles, are a major fraction of environmental airborne particles. However, no regulations are available for controlling nanoparticles, despite that such regulations for the nanoparticle emissions are needed for global health and wellbeing. Understanding the behavior of intermediate particles and their separation from the air are important to the policy-making and technology development for the protection of human health and the environment.

Separation and deposition of entities underlie the adsorption and filtration processes. Adsorption is a well-known method for the separation of molecules, and filtration is for the separation of airborne particles. Despite the efforts on the theoretical analyses of adsorption and filtration, a holistic framework for the separation of a whole range of entities is needed to unify their mechanisms of separation.

This research aims to develop a comprehensive model for the separation of entities including gas molecules, intermediate nanoparticles, and regular nanoparticles, from the air. The specific contributions to the field include

1. Modeling the transport of entities to the nanofiber surface by considering both convective diffusion and interfacial interaction due to the van der Waals force.
2. Modeling the deposition of intermediate nanoparticles onto clean fibers.
3. Modeling the effects of time and concentration on the deposition of all entities onto nanofibers.

The first model calculates the rate of particles, transported to the fiber surfaces. The rate of collision based on convective diffusion and interfacial interactive diffusion is calculated by boundary layer analysis around a single fiber. In addition to airflow, the entities are under another streamflow due to the van der Waals force. This model is validated using experimental data from the literature for nanoparticles.

The second model is developed by considering the interfacial interaction on the adhesion of intermediate nanoparticles on clean fiber. Brownian diffusion, which has been considered as the mechanism of filtration of sub-100 nm particles, is not affirmative for intermediate nanoparticles. In this model, the interfacial interaction plays an important role in the adhesion and detachment of intermediate nanoparticles. Adhesion probability is determined as a function of particle size and interfacial interaction energy.

The third, kinetic model is an expansion of the second one by considering surface coverage, which depends on time and particle concentration. This kinetic model applies to both gas molecules, and intermediate nanoparticles, by considering their surface coverage. Concentration and time may play an interchangeable role in surface coverage and deposition of entities. This kinetic model is validated using experimental data of adsorption and the filtration of intermediate particles in the literature.

Finally, the preceding theoretical analyses were used to guide the engineering applications in two case studies. One is the transport and removal of airborne dental particles in a dental office (Appendix A), and the other, facial masks for the filtration of nano/micro-particles (Appendix B). Both studies shed light on the engineering applications of aerosol dispersion and filtration, although they are not directly related to interfacial behavior.

Acknowledgments

I would like to thank my co-supervisors, Drs. Zhongchao Tan and Zhao Pan for their patient guidance, incredible support, and encouragement. I would like to thank my Ph.D. examination committee members, Drs. Hongbo Zeng (Univ. of Alberta), Zhongwei Chen, Ehsan Toyserkani, and John Wen.

I would also like to thank Greg Friday for his technical support. In addition, my warm gratitude goes to all members of Air Pollution and Green Energy Lab during the tenure of my Ph.D. studies, including Joerg Ahne, Raheleh Givehchi, Haiming Wang, Yifu Li, Milad Khodabakhshi, Wala Bkari, and Fangyan Sun. It was also a great pleasure to work with some fantastic coop students and undergraduate research assistants: Connor Peter McCallum, Allison Irvine, Noelle Wong, Theodor schlotzhauer, and Claire Parrott.

I wish to thank my parents, Farkhondeh and Javad, and my brothers Alireza and Amirhossein. Thanks for your constant unconditional support, and encouragement. Words cannot express my gratitude for everything that you have done for me.

Above all, I would like to thank my beloved friend, schoolmate, and husband, Hamed, for his understanding and love in the past few years. I owe you everything.

Table of Contents

List of Figures

List of Tables

List of Symbols

Notation	Term	Unit
A	Hamaker constant	J
A_{bet}	Specific surface area	m^2/g
a	Contact radius	m
C_c	Slip correction factor	-
d_f	Fiber diameter	m
d_p	Particle diameter	m
D	Diffusion coefficient of particles	m^2/s
E_{int}	Interaction energy	J
E	Young's moduli	Pa
e	Unit of charge	C
e_r	Restitution coefficient	-
F_{vdw}	Van der Waals force	N
f_c	Charge fraction	-
F	The flux of molecules striking the surface	$\#/(sm^2)$
h	Planck's constant	Js
H	Hardness	Pa
k	Overall effective mass transfer coefficient	1/s
k_b	Boltzmann's constant	J/K
Kn_p	Particle Knudsen number	-
Ku	Kuwabara hydrodynamic factor	-
L	Thickness of filter	m
L_{eff}	Effective length	m
LOD	Limit of detection	$\#/m^3$
m	Filter weight	g
m_p	Particle weight	-
n	Particle number concentration	$\#/m^3$
n_0	Particle number concentration outside CBL	$\#/m^3$
n_r	Particle number concentration at the fiber surface	$\#/m^3$

N	The rate of particles entering the boundary layer in each θ	#/s
N_t	The total rate of particles entering the boundary layer	#/s
N_f	The rate of particles entering the boundary layer in each θ from the air flow	#/s
N_{vdw}	The rate of particles entering the boundary layer in each θ from van der Waals force	#/s
N_{down}	Downstream number concentration	#/m^3
N_{up}	Upstream number concentration	#/m^3
Pe	Peclet number	-
P_i	Probability of state *i*	-
P_a	Probability of adhesion on an empty site	-
P_b	Probability of bouncing from an empty site	-
P_c	Probability of proceeding to the next site from an empty site	-
P'_a	Probability of adhesion on a filled site	-
P'_b	Probability of bouncing from a filled site	-
P'_c	Probability of proceeding to the next site from a filled site	-
P	Overall detection efficiency	-
p	Pressure	Pa
q	Mass concentration at the surface at time t	-
q_e	Maximum mass concentration at the surface	-
Q	Flow rate	m^3/s
Q_e	Electric charge	C
Q_F	Quality factor	1/Pa
r	Polar coordinates component	m
r_e	Separation of minimum potential energy	
R_f	Fiber radius	m
R_p	Particle radius	m
r_{ad}	Adsorption rate	#/s
r_{des}	Desorption rate	#/s
S_0	Initial adhesion probability	-
Stk	Stokes number	-

t	Time	s
T	Temperature	K
u	Aerosol face velocity	m/s
u_r	Velocity component in polar coordinates	m/s
u_θ	Velocity component in polar coordinates	m/s
U	Electric dipole moment	Cm
v	Electric absorption (ionization) frequency	s^{-1}
v_{vdw}	Van der Waals velocity	m/s
V_{im}	Impact velocity	m/s
V_{cr}	Critical velocity	m/s
w	Pair potential	j
y	Surface coverage	-
z_0	Equilibrium or minimum distance between bodies	m
Z_p	Particle electrical mobility	m
Greek letters		
α	Solidity of filter	-
α	Electric polarizability	$C^2m^2J^{-1}$
β	Mobility of particles	-
β_r	Aerosol to sheath flow ratio	-
ε_0	Dielectric permeability of free space	$C^2J^{-1}m^{-1}$
δ	Deformation	m
η	Total filtration efficiency	-
η_0	Single fiber filtration efficiency	-
η_{ad}	Adhesion probability	-
η_c	Collision efficiency	-
η_{samp}	Penetration efficiencies through a sampling line	-
η_{char}	Penetration efficiencies through the charger	-
η_{DMA}	Penetration efficiencies through DMA	-
η_e	Penetration efficiencies through electrometer	-
μ_{air}	Kinetic viscosity of air	Kg/(ms)

μ	Dimensionless deposition parameter	-
μ_t	Tabor's parameter	-
σ_A	The density of adsorption sites	#/m^2
ν	Poisson's ratio	-
ψ	Stream function	m^2/s
ψ_f	Stream function of air flow around a nanofiber	m^2/s
ψ_{vdw}	Stream function of air flow around a nanofiber	m^2/s
ρ	CBL thickness	m
ρ_p	Particle density	Kg/ m^3
ρ_f	Fiber density	Kg/ m^3
θ	Polar coordinates component	-
λ	Mean free path	m
τ_P	Relaxation time	s

Chapter 1
Introduction

1.1 Research background

Airborne nanoparticles, as part of particle matter (PM), have a great impact on human health and the environment [1-4]. PM is recognized as the second largest risk factor for non-communicable diseases worldwide in 2018 after tobacco smoking, which is primarily inhalable particles too [5]. Larger nanoparticles mostly deposit in the alveolar region of the respiratory system and damage cardiovascular systems [6], while smaller ones impact the neural system [7], cause DNA damage, neuroinflammation, brain structure changes, cognitive deficits, and Alzheimer [6, 8-10].

Generated aerosols are one of the most considerable routes in the transmission of infectious diseases [11-15]. The infectious microorganisms include pneumonic plague, Legionella pneumophila, tuberculosis, influenza viruses, herpes viruses, SARS virus (a form of coronavirus), pathogenic streptococci, and staphylococci [11, 16]. Recently, COVID-19 joins this list [15]. World Health Organization (WHO) states that particles smaller than 5 μm in diameter remain in the air for long periods and be transmitted to other places. Intermediate nanoparticles play a critical role in both health because of their abundance and lingering longer time in the air [17].

In addition, nanoparticles impact climate through radiative effects [18]. Intermediate particles with sizes of single-digit nanometers, which bridge gas molecules and aerosol particles, are a major fraction of environmental airborne particles that are responsible for the aforementioned health and environmental problems [17].

Intermediate nanoparticles can be generated by combustion, condensation, friction, and so on. Combustion is a major source of intermediate nanoparticles. Measurements show that 20–54% of the total particle concentration in the ambient air are carbonaceous sub-3 nm nanoparticles [19, 20]. These

concentrations are higher for those produced in high-temperature combustion [21]. Intermediate nanoparticle generation will be a serious challenge because high-temperature combustion is an essential part of the future of combustion technologies. The number concentrations of intermediate nanoparticles are much higher than the soot particles generated from combustion processes. Intermediate metal nanoparticles are also generated from the melting of engine fragments [22]. Sliding contacts are also another source of intermediate nanoparticles [23]. As an example of sliding contacts, up to 80% of the particles by number generated from the brake friction pairs are 1.3–4.4 nm [23]. In addition to the primary intermediate nanoparticles, secondary intermediate nanoparticles are formed by condensation of volatile organic compounds (VOCs) generated by traffic [19]. Intermediate nanoparticles remain in the size that they are generated [18].

No standard and regulation are available for intermediate nanoparticles despite well-established regulations for PM2.5 and gas emissions. Establishing transportation emission policies in some countries had made some progress toward reducing the impact of transportation sector on air pollution [24]. Clean air policies were established to mitigate primary PM2.5 emissions (responsible for almost half of air pollution) and secondary aerosols, which are oxidized from precursor emissions such as sulfur dioxide (SO2), nitrogen oxides (NOx), ammonia (NH3), and non-methane volatile organic compounds (NMVOCs) as well as ozone (O3), carbon oxides (CO2), and carbon monoxide (CO) [24, 25]. To evaluate the effectiveness of existing policies, the Institute for Health Metrics and Evaluation (IHME) and the World Health Organization (WHO) have been assessing annually the global impact of ambient air pollution on health since 2012 [24]. A clear understanding of pollutant behaviors is essential to knowledge-based policy-making as well as related technologies for air cleaning to alleviate global health issues.

Moreover, nano-sized materials have garnered attention because of their unique properties and distinct functionalities in basic and applied sciences [26], such as drug delivery, biomedicine, energy

and environmental, nanoelectronics, heterogeneous catalysts surface coating, ultra-smooth surface manufacturing industry, surface metallization and surface cleaning [27-34]. Therefore, it is vital to collect, characterize, explore, or synthesis of whether engineered, fundamental research on their behavior and interactions.

Separation and deposition of entities, including gas molecules, intermediate nanoparticle, and larger aerosol particles, underlie in the principles of gas adsorption and air filtration. Adsorption is a well-known method for the separation of molecules, and filtration is for the separation of airborne particles. Despite the decades of theoretical research on filtration and adsorption, a holistic framework is still missing for the whole range of entities: there is a gap between the theories of adsorption and filtration.

1.2 Research motivation

The separation of nanoparticles from the air is achieved by particle transport followed by particle-surface adhesion. According to conventional air filtration theories, the filtration efficiency of intermediate nanoparticles would approach 100% because of Brownian diffusion (Figure 1-1.a). These theoretical analyses based on convective diffusion have not been verified for a wide range of particles and fiber sizes. In addition, some researchers attempted to investigate the effects of interfacial interaction on the transport of nanoparticles to nanofiber surfaces [35, 36]; however, their models are not experimentally validated. Nonetheless, the assumption of 100% adhesion probability may become uncertain for intermediate nanoparticles colliding on nanofibers. This lack of fundamental knowledge of adhesion is also pointed out in several review papers [37-41].

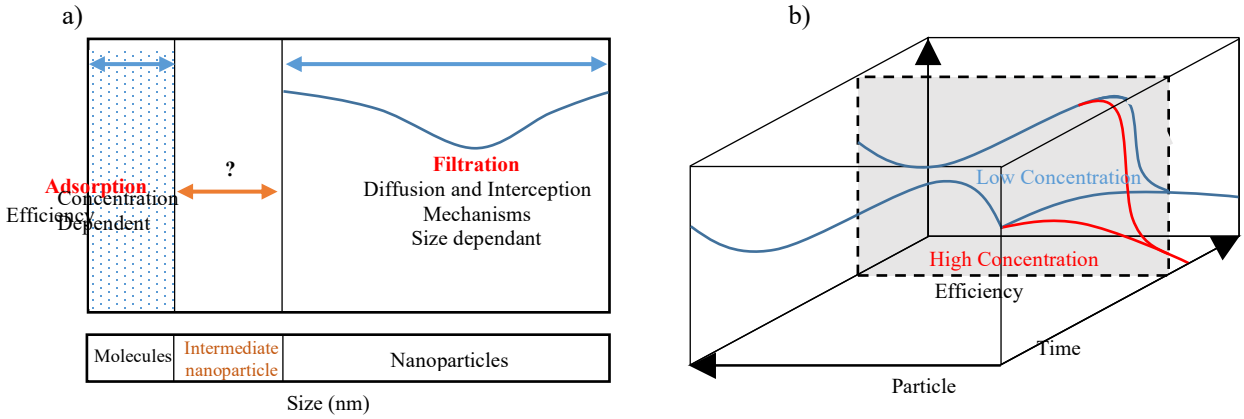

Figure 1-1 Knowledge gap between filtration and adsorption, b) hypothesis for deposition model

There are several models developed for adhesion of intermediate nanoparticles on surfaces based on interfacial forces [42-45]. For example, Dahneke proposed that intermediate nanoparticles are bound to the surface by molecular attraction [42]. Additionally, Hiller and Loeffler state that the filtration efficiency of intermediate nanoparticles strongly depended on the interaction energy between particles and single fibers[43]. Wang [44] extend their works and Wang and Kasper [45] developed a thermal rebound model for sub-10 nm particles. Later, Mouret *et al*. [46] proposed that the thermal rebound might happen only for sub-1 nm particles. These earlier studies, however, have not been validated yet.

To better understand particle deposition due to interfacial forces, we need to revisit the concept of van der Waals force, which may bridge the gap between molecules and nanoparticles. The van der Waals force is considered as the main factor in the adhesion of sub-micro systems [47, 48] and the adsorption of molecules on surfaces [49-51]. In a physisorption process, the molecules in the gas-phase (or liquid) are adsorbed because of the van der Waals force between the adsorbed molecules and the solid surfaces [52-55]. Intermediate nanoparticles are expected to have similar deposition behavior like gas molecules. Non-perfect adhesion has been considered in several adsorption models, where only a fraction of striking molecules are adsorbed because of the weakened interfacial interaction at the

intermediate size [54, 56]. For example, Chernyakov proposed that the filtration efficiency of intermediate nanoparticles drops because of desorption. In his model, the residence time of particles in the bond state is considered, where the efficiency reduction takes place due to desorption for long times of filter operation [57], although experimental results [58] showed a reduction of efficiency even for short times of operation.

In addition to the size dependency of interfacial interaction, time and initial concentration may also affect the deposition of intermediate particles on nanofibers. In kinetic adsorption, both time and initial concentration are influential parameters on the deposition rate on the adsorbate. The concentration dependency of nanoparticle filtration has been observed in the filtration of aerosol particles [36, 58, 59]. These findings are contrary to conventional filtration theories, which claim that concentration and operation time do not affect the filtration efficiencies of nanoparticles. Therefore, the roles of both initial concentration and time (*i.e.*, kinetic behavior) on the interfacial interaction should be considered for the analysis of this behavior. This thesis presents a comprehensive model for the deposition of entities from a few Angstroms to tens of nano-sizes to address the knowledge gaps listed above (Figure **1-1**.b).

1.3 Research objectives

The main objective of this research is to develop a comprehensive model for the deposition of entities from molecular to nano-sizes. The following tasks were completed to achieve this goal:

1. Modeling the transport of entities to the nanofiber surface by considering connective diffusion of nanoparticles and particle-fiber interfacial interaction.
2. Modeling the deposition of intermediate nanoparticles onto clean fibers.
3. Modeling the effects of time and concentration on the deposition of all entities onto nanofibers.

1.4 Research approach

Figure 1-2 shows the overall structure of this thesis, which is organized into seven chapters. Chapter 1, the current chapter, provides an overview of the research problem and describes the motivation, opportunities, and objectives of the research. These factors form the context of the comprehensive review presented in Chapter 2. The literature review covers the background knowledge about the properties of intermediate nanoparticles, filtration models, adsorption kinetics and isotherms, and interfacial interaction of entities.

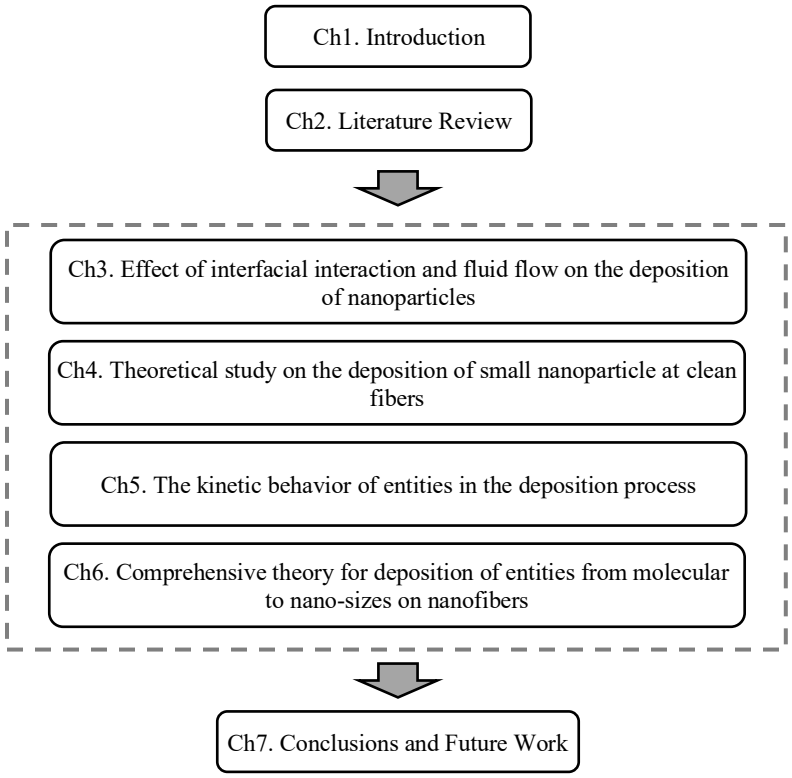

Figure 1-2 Thesis structure

Chapter 3 presents a model for the rate of particles diffusing to the surface of a single fiber. The rates of collision based on convective diffusion and interfacial interactive diffusion are obtained using

boundary layer analysis around a single fiber. At last, this model is validated using experimental data from the literature.

Chapter 4 is mainly focused on the deposition of intermediate nanoparticles. An analytical model is developed for the deposition of intermediate nanoparticles on a clean nanofiber surface. This model is developed based on interfacial interactions between intermediate nanoparticles and the surface along with the transport mechanisms for deposition of intermediate nanoparticles adhesion probability. Adhesion probability is based on the interfacial interaction of intermediate nanoparticles between intermediate nanoparticles and the nanofiber surfaces.

In Chapter 5, the model from Chapter 4 is extended by the consideration of surface coverage. The adhesion probability from the previous chapter is improved by considering the surface coverage over time. This kinetic model is also validated using experimental data of gas adsorption and the filtration of intermediate particles. Prior to comparing the model to the experimental data, the role of instrument on the uncertainty of measurement for the filtration of sub 2 nm nanoparticles is investigated to determine the reliability of the measurements; The error of filtration efficiency associated with the limit of detection (LOD) of the system due to the noise level is characterized.

Chapter 6 presents a comprehensive model for all state-of-the-art theories, including gas adsorption, intermediate nanoparticle filtration, and normal aerosol filtration. The new model is developed by considering the quasi-steady deposition of entities, kinetic behavior of adhesion, and interfacial interaction. Finally, major findings and future directions are discussed in Chapter 7.

Chapter 2
Literature review

2.1 Summary

This chapter provides an overview of the characteristics of nanoparticles and their environmental and health impacts. These characteristics include entity size, stability, concentration, and so on. Moreover, the deposition of nanoparticles in the filtration and adsorption are reviewed. The interfacial interaction of entities is also summarized in this chapter. A better understanding of the characteristics of nanoparticles and their interfacial interactions may help in the development of a model for the deposition of nanoparticles.

2.2 What are intermediate nanoparticles

Nanotechnology is vital in many disciplines including electronics, energy, environmental protection technologies, and drug delivery. According to the Royal Society and Royal Academy of Engineering Nanoscience and nanotechnologies are defined as following [60]:

> "*Nanoscience is the study of phenomena and manipulation of materials at atomic, molecular and macromolecular scales, where the properties differ significantly from those at a larger scale*"; likewise, "*Nanotechnologies are the design, characterization, production, and application of structures, devices, and systems by controlling shape and size at nanometer scale*".

Nanomaterials are the elements of nanotechnology with at least one dimension less than 100 nm. Examples include nanoparticles, nanofibers, nanotubes, composite materials, and nanostructured surfaces. Specifically, nanoparticles are defined as particles with a diameter of less than 100 nm [61]. In this study, intermediate nanoparticles are defined as the intermediate nanoparticles in between molecules and nanoparticles.

Nanoparticles suspended in the air (nano-aerosols) originate from both industrial and natural sources, and both categories are subdivided into primary and secondary ones. Primary industrial sources include hot processes (*e.g.*, smelting, refining, and welding), combustion processes (*e.g.,* transportation and carbon black manufacture), and bioaerosols (*e.g.*, viruses and endotoxins). Additionally, natural sources include sea spray, volcanic activity, forest fires, and soil dust. Secondary nanoparticles are formed by condensation of vapors and gases. This process which is called atmospheric nucleation generates a considerable source of aerosol nanoparticles in the atmosphere [19, 23, 62, 63]. In some systems, unwanted nanoparticles need to be removed. Engineered nanoparticles with unique properties are another source of nanoparticles, which are deliberately synthesized [37, 64] for special applications such as drug delivery, biomedicine, energy, and environmental protection technologies [30-32].

2.2.1 Intermediate nanoparticle characteristics

2.2.1.1 Size of ambient nanoparticles

Figure 2-1 shows the classification of nanoparticles into nucleation and Aitken-modes. In the nucleation mode, particles are smaller than tens of nanometers. These particles are important for the formation and growth of larger ones. Their surface to volume ratio is high., Most nucleation-mode particles in the atmosphere consist of sulfates, nitrates, and organic compounds. They are formed by homogeneous nucleation processes that occur at ambient temperatures. The second category is Aitken-mode in the size range of 10 to 100 nm which overlaps with the nucleation mode. Aitken-mode particles are formed by coagulation and condensation of nucleation-mode particles. Depending on their nature, they may grow in size as they form chains [63].

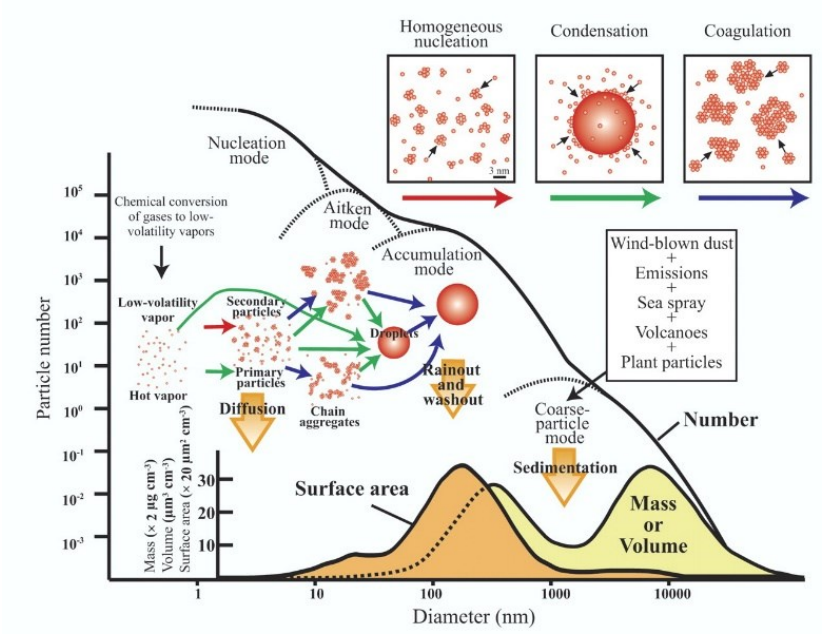

Figure 2-1 The size distribution of aerosol particles (used with permission [63])

2.2.1.2 Properties of nanoparticles

Nanoparticles exhibit unique physical and chemical properties because of their distinctive surface structures. Their mechanical, electronic, optical, electrical, and thermal behavior are different from those of bulk materials [37, 61, 65, 66]. The fraction of atoms at the surface to the total number of atoms of nanoparticles increases as the size of nanoparticles decreases. This characteristic causes variation of nanoparticle properties from their bulk. Some researchers argue that the deviation of properties from bulk begins at a size in the range of 20–30 nm. However, the exact size depends on the structure of the particles [37, 61, 65, 67]. Size-dependent mechanical properties of nanoparticles play a major role in the deformation of particles after collision. Therefore, mechanical properties such as hardness, elastic modulus, and interfacial adhesion need to be well understood. Although bulk properties were used in previous theories [30], the mechanical properties of nanoparticles are size-dependent and do not have clear behavior [30, 68]. In the majority of them, the strongest size has been

defined where the elastic modulus is maximum. It means that a particle with the strongest size resists the most against the deformation. In contact models, however, bulk elastic modulus has been used which is not size-dependent.

Nanomaterials can become harder or softer, depending on their structure, as the particle size decrease. Crystalline structures exhibit more hardness than amorphous structures. The reduced number of bonds makes amorphous structures softer. In viscoelastic materials with soft surfaces, adhesion enhances with larger contact area. For hard materials, the adhesion force is lower than the value predicted by contact models because of less contact area., On the other hand, the contact area exceeds the contact models for soft materials.

The mechanical properties of nanoparticles are also temperature dependant. The elastic region is more temperature-dependent than the elastic region. The coefficient of restitution (COR) which is defined as the ratio of the rebound velocity to the collision velocity, indicates the loss of kinetic energy through collision. However, the hardness of a nanoparticle with a surface in the collision is not fully understood yet and further research is required.

2.2.1.3 Structure and stability

The surface energy of intermediate nanoparticles is greater than larger ones and they are thermodynamically unstable. The crystallographic change and rearrangement of surface atoms lead to a decrease in the excess of surface free energy and subsequently stabilize them. The interfacial reactivity and other unique properties of nanoparticles are attributed to these structural changes [67]. Global bond order parameters such as Steinhart's bond order characterize the structural change in nanoparticles that are subject to collisions [69, 70]. Lattice parameter depends on particle size, and sub -10 nm particles exhibit bimodal behavior [27, 69].

The particle shape is another important parameter for the movement of the particle with respect to a surface. Spherical particles slide or roll on the surface, but non-spherical ones may tumble on a corner or edge; thus, non-spherical particles interact with a surface in a different way. For instance, cubic particles could detach when they contact the edge of a surface; however, the effects of shape effect on collision increase with decreasing particle size [71, 72].

Xu et al. reported the crystal defects and deformation of nanoparticles with an average size of 60 nm in diameter[29]. Molecular dynamics (MD) simulation illustrates that the crystalline nanoparticle structure has crystal facets, steps, and sharp edges on their surfaces, which result in rough particle surface. Despite some atomic roughness, amorphous nanoparticles have smooth surfaces.

2.2.1.4 Concentration of nanoparticles

It has been proven that nanoparticles have the largest particle number concentrations. Recent studies show that a large fraction of atmospheric aerosol particles is in the range of 1.3-10 nm [19, 23] [73]. These intermediate nanoparticles are generated by combustion, condensation, friction, and so on. Measurements show that 20–54% of the total particle number concentration in ambient air are carbonaceous sub-3 nm nanoparticles [19, 20]. The concentrations are higher for those produced in high-temperature combustion [21]. Intermediate nanoparticle emission will become a growing challenge because high-temperature combustion is an essential part of the future of combustion technologies. Intermediate metal nanoparticles are also generated from the melting of engine fragments [22] and sliding contacts [23]. As an example of sliding contacts, up to 80% of the particles by number emitted from brake friction pairs are in the size range of 1.3–4.4 nm [23]. In addition to the primary intermediate nanoparticles, secondary intermediate nanoparticles are formed by the condensation of volatile organic compounds (VOCs) [19]. Intermediate nanoparticles remain in the size that they are generated [18]. By increasing the concentration of nanoparticles in different sources, the negative

impacts of nanoparticles on human health and the environment have increased, which is discussed in the following section.

2.2.2 Environmental and health impact of intermediate nanoparticles

The particle size and surface area of nanomaterials are important factors causing health impacts through inhalation [61, 74]. The probability of inhaled particles with the size of 100 nm is almost 90% [75, 76] (Figure 2-2) and 50% in the alveolar region subsequent entry into the bloodstream. Nanoparticles have 2-5 times greater deposition in the alveolar region of lungs than larger particles do [74]. Exposure to nanoparticles causes health issues such as lung cancer, pulmonary and cardiovascular diseases, heart disease, asthma, and increased mortality [77, 78]. Larger nanoparticles have higher deposition probability in the alveolar region of the respiratory system. Subsequent entry of them into the blood-stream causes health issues such as lung cancer, pulmonary and cardiovascular diseases, heart disease, asthma, and increased mortality [77, 78], while smaller nanoparticles are mostly deposited in the head airways cause brain diseases such as Alzheimer [6].

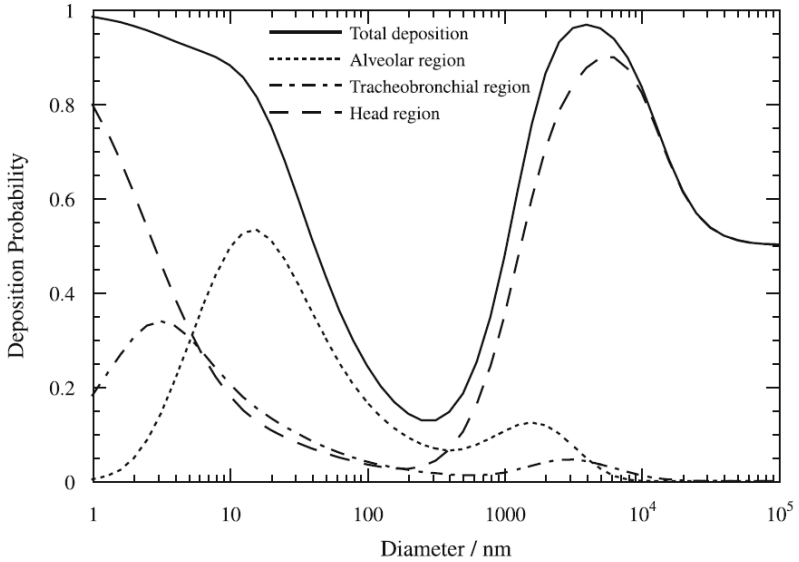

Figure 2-2 Deposition model for an adult breathing through their nose at 25 l/min with permission from [68]

2.3 Nanoparticle filtration by nanofibrous filters

Nowadays, using fibrous media to remove the fine particles from an air stream is the most promising technology. They are used in many applications, including respiratory protection, air cleaning, processing of nuclear wastes, purification processes, dust collection at power plants, clean rooms, and so on [79, 80]. Low basis weight, high permeability, tight pore size, and large surface area to volume ratio of nanofibers improve filtration performance by increasing the probability of nanoparticle deposition. They also operate at high flow rates with low-pressure drops [38, 79, 81-83].

Nanofibrous filters can be produced by various methods such as electrospinning, melt-blown technique, and multicomponent fiber spinning. Among them, electrospinning is the most prevalent method which can produce fibers as small as 40nm. Overall, a nanofibrous filter can be engineered for a wide range of diameters (40-2000 nm) and filter porosity in the range of 80–90% [81, 83].

High removal efficiency and low pressure-drop are desirable in every filtration application. Filters with higher efficiencies and lower pressure drops have better quality factors. The quality factor of a filter is calculated using

$$Q_F = \frac{-\ln(1-\eta)}{\Delta P} \tag{2-1}$$

where η is the total efficiency and ΔP is the pressure drop over the filter. The removal efficiency of a filter is the fraction of particles that can be captured by the filter.

$$\eta = 1 - \frac{N_{down}}{N_{up}} \tag{2-2}$$

where N_{down} and N_{up} are downstream and upstream concentrations, respectively. Based on classical filtration theories and the single-fiber efficiency model, total filtration efficiency is a function of single fiber efficiency [84]:

$$\eta = 1 - \exp\left(\frac{-4\alpha\eta_0 L}{\pi d_f(1-\alpha)}\right) \tag{2-3}$$

where η_0 is the single fiber efficiency, α is the solidity of the filter, L is the thickness of the filter, and d_f is the mean fiber size. In Equation (2-3), it is assumed that the filter has a uniform packing density, that all fibers are straight and have the same diameter, that all fibers are perpendicular to the flow direction, and that single-fiber efficiency remains unchanged with the depth of the filter [38]. Without this assumption, Equation (2-3) overestimates the total efficiency.

Several mechanisms play a role in capturing particles by a single fiber. Diffusion, interception, inertial impaction, and electrostatic interaction from those mechanisms are taken to account while particles cross the filter media. Figure 2-3a shows the contribution of each mechanism in filtration efficiency for particles larger than 10 nm. Nanoparticles are captured by Brownian diffusion mechanisms which become more dominant with decreasing particle size [81].

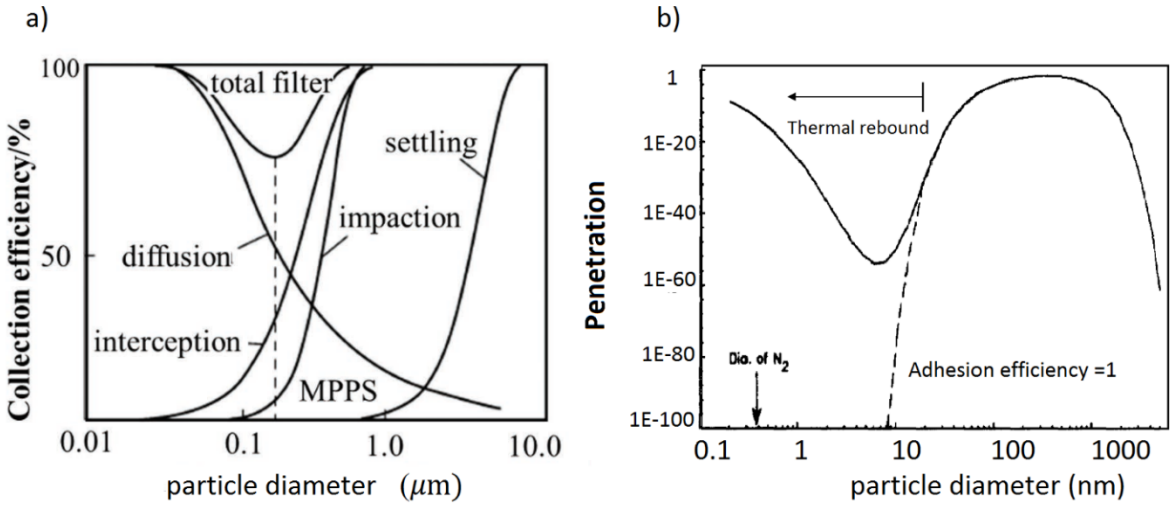

Figure 2-3 a) filtration mechanisms as a function of particles size larger than 10nm (reproduced from [81]-open-access reference), b) penetration mechanisms of particles which including thermal rebound (with permission from [45])

A single-fiber efficiency is defined as the ratio of the numbers of particles collected by a fiber of unit length to that in the gas stream. Not all particles collide on the surface result in adhesion; only a fraction of them adhere to the surface because of the interaction between the particles and the surface. The single-fiber efficiency is a product of collision efficiency, η_c, and adhesion efficiency, η_{ad}:

$$\eta_0 = \eta_{ad}\eta_c \tag{2-4}$$

In classical filtration models, the adhesion efficiency is assumed to be equal to unity, whereas the collision efficiency would be the same as single-fiber efficiency.

2.3.1 The collision of particles with the fibers

There are various approaches to the estimation of the collector efficiency [85, 86]. The first approach is that individual mechanisms add together, and collection efficiency calculated as:

$$\eta_c = \sum_{i=1}^{N} \eta_i \tag{2-5}$$

where N is the total number of mechanisms and η_i is the efficiency of mechanism i. In the additivity rules, by adding the efficiencies due to various mechanisms altogether, the efficiency is overestimated because a particle could be considered captured twice by two mechanisms[85]. The second approach collection efficiency is calculated from penetration which is the product of penetrations due to N mechanisms:

$$1 - \eta_c = \prod_{i=1}^{N} (1 - \eta_i) \tag{2-6}$$

Interception and Brownian diffusion are widely accepted as the main mechanisms for nanoparticles. Different expressions for these two mechanisms are proposed empirically and theoretically which is reviewed by Givechi and Tan [82]. Depending on the size range, dominant mechanisms can represent the overall efficiency [38]. However, no single mechanism is validated for intermediate nanoparticles.

Podgórski and Bałazy (2008) demonstrated that single-fiber efficiency should be a function of three dimensionless parameters: Peclet number (Pe) Stokes number (Stk) and interception parameter (R). Pe, Stk, and R determine the mechanisms of inertial impaction, interception, and diffusion respectively [87, 88]. These dimensionless parameters are given as:

$$\eta_0 = f(\mathrm{Pe}, \mathrm{Stk}, \mathrm{R}), \tag{2-7}$$

$$\mathrm{Pe} = \frac{u\, d_f}{D}, \tag{2-8}$$

$$\mathrm{Stk} = \frac{u\, \tau_P}{d_f}, \text{and} \tag{2-9}$$

$$R = \frac{d_P}{d_f} \tag{2-10}$$

where d_f is the mean fiber diameter, u is face velocity, D is the diffusion coefficient of particles with the size d_P and τ_P is the Relaxation time[38, 82].

2.3.2 Adhesion of particles to the fibers

Several researchers investigated the deposition of intermediate nanoparticles, and they claim that the transport of particles is not the only dominant mechanism of deposition. After a collision, the particles may detach from the surface and return to the airflow. Dahneke proposed that particles of an intermediate size approaching gas molecules are bound to the surface by molecular attractions. The probability of detachment based on interaction energies was defined in this model [42]. In addition, Hiller and Loeffler [43] stated that the filtration efficiency of particles of a few nanometers strongly depends on the interaction energy between the particles and the single fibers. For the first time, they introduced adhesion efficiency to be multiplied by single-fiber efficiency. Later, Wang [44] extended these earlier works, and Wang and Kasper [45] proposed the thermal rebound model for sub-10 nm particles.

According to the thermal rebound theory, the adhesion efficiency is determined from the interaction between the particles and the filter media, where van der Waals force is responsible for this interaction. Adhesion of particles to the surface strongly depends on adhesion energy and Hamaker and the JKR theory are used in this hypothesis. Based on this hypothesis, when the impact velocity of particles becomes greater than a critical value, the nanoparticles will rebound from the surface. Effectiveness of collisions (R) is defined as the ratio of impact velocity to the critical velocity ($R = \overline{V_{im}}/V_{cr}$), where $\overline{V_{im}}$ is mean thermal impact velocity from Boltzmann distribution. The thermal impact velocity is given as [45]:

$$\overline{V_{im}} = \left[\frac{48k_bT}{\pi^2\rho_p d_p^3}\right]^{1/2} \tag{2-11}$$

where k_b is the Boltzmann constant, T is the temperature, ρ_p is the density of the particle, and d_p is the particle size. The critical velocity, V_{cr} is calculated from energy conservation:

$$V_{cr} = \left[\frac{2E_{int}}{m_p {e_r}^2}\right]^{1/2} \tag{2-12}$$

where E_{int} is the adhesion energy between the nanoparticles and the surface. Therefore, adhesion efficiency is defined as the distribution of impact velocity where it is higher than critical velocity over the integral of the whole distribution of impact velocity. Adhesion efficiency is determined as:

$$\eta_{ad} = \frac{\int_0^{V_{cr}} f(V_{im})dV_{im}}{\int_0^{\infty} f(V_{im})dV_{im}} \tag{2-13}$$

Or

$$\eta_{ad} = \int_0^{1/R} \frac{32x^2}{\pi^2} \exp\left(\frac{4x^2}{\pi}\right) dx \tag{2-14}$$

Adhesion energy from different contact models is applied in thermal rebound theory, which is presented in the next section.

2.3.3 Theoretical models of contact

The interaction between a particle and a surface has been considered in many studies. The Bradley-Hamaker model considered the interaction between two rigid spheres due to the van der Waals forces, and this model fails to consider the adhesion force resulting from the impaction. Hertz's theory was published on the interaction of two spherical surfaces where there is no external force. Johnson Kendall Roberts (JKR) theory considered elastic interaction of two deformable large bodies. Derjaguin Muller Toporov (DMT) described small and hard bodies. Figure 2-4 shows rigid and deformable surfaces in contact.

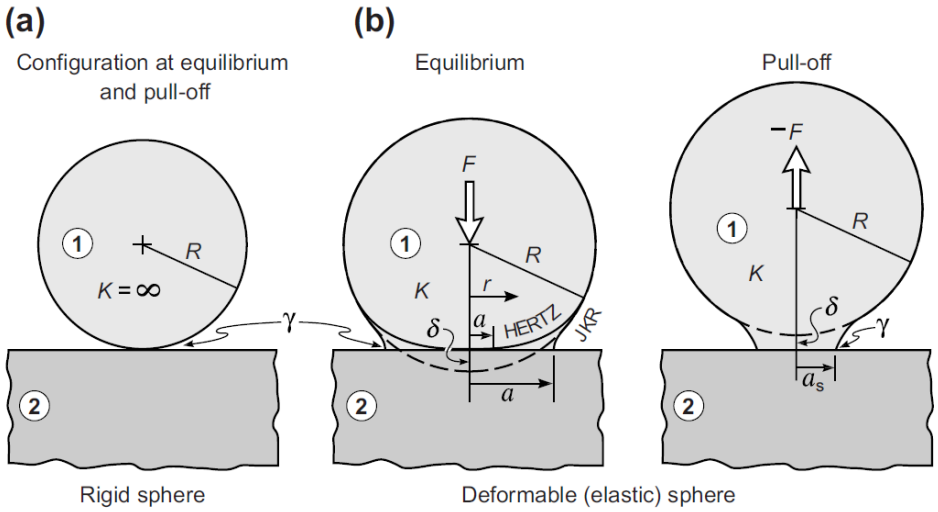

Figure 2-4 Deformations of (a) rigid and (b) elastic sphere (with permission from [51])

Tabor defined a physical parameter to compare DMT and JKR theories. Tabor's parameter μ_t is defined as a ratio of the elastic displacement of a surface to the effective range of surface forces at the pull-off point [46, 89, 90].

$$\mu_t = \frac{R^{*1/3}\Delta\gamma^{2/3}}{Z_0 E^{*2/3}} \tag{2-15}$$

where E^* is the reduced Young's modulus and R^* is the reduced radius for a particle and a surface:

$$\frac{1}{E^*} = \frac{3}{4}[((1-\nu_1^2)/E_1) + ((1-\nu_2^2)/E_2)] \tag{2-16}$$

$$\frac{1}{R^*} = \frac{1}{R_1} + \frac{1}{R_2} \tag{2-17}$$

Table 2-1 summarizes the contact radius, deformation, and the adhesion force for two contacting spheres according to the Hertz, JKR, and DMT theories. In this table, F is the external force, H is the hardness of the deformed material, E and ν are Young's moduli and Poisson's ratio, respectively. The difference between these contact models lies in the pressure distribution across the contact surface, which is illustrated in Figure 2-5 for the JKR, DMT, and MP models, respectively [91].

Table 2-1 Relations between the contact radius, the contact radius due to adhesion force without an external load, the deformation and the adhesion force for two spheres contacting each other in the Hertz, JKR, and DMT contact models [30] (open-access reference)

	BH	Hertz	JKR	DMT	MP
contact radius, a	-	$\left(\frac{R^*F}{E^*}\right)^{1/3}$	$\left\{\frac{R^*}{E^*}(F + 3\pi R^*\gamma + (6\pi R^*\gamma F + (3\pi R^*\gamma)^2)^{1/2})\right\}^{1/3}$	$\left[\frac{R^*}{E^*}(F + 2\pi R^*\gamma)\right]^{1/3}$	$\left(\frac{F+2\pi\gamma R^*}{\pi H}\right)^{1/2}$
deformation, δ	-	$\frac{a^2}{R^*}$	$\frac{a^2}{R^*} - \left(\frac{8\pi a\gamma}{3E^*}\right)^{1/2}$	$\frac{a^2}{R^*}$	-
contact radius without an external load, $\boldsymbol{a_0}$	-	*0*	$\left(\frac{6\pi R^{*2}\gamma}{E^*}\right)^{1/3}$	$\left(\frac{2\pi R^{*2}\gamma}{E^*}\right)^{1/3}$	$\left(\frac{2R^*\gamma}{H}\right)^{1/2}$
$\boldsymbol{F_{ad}}$	-	0	$\frac{3\pi R^*\gamma}{2}$	$2\pi R^*\gamma$	-
$\boldsymbol{E_{ad}}$	$\frac{AR_1}{6z_0}$		$\left[\frac{81}{4}\pi^7 R_1^4 \sigma_{p,s}^5 (K_s + K_p)^2\right]^{1/3}$	-	-

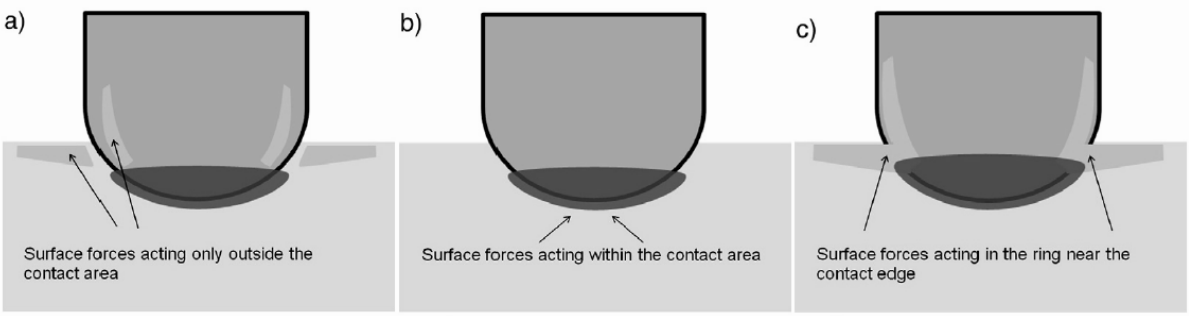

Figure 2-5 a) JKR, b) DMT, and c) MP model (reproduced with permission from [91])

Figure 2-6 shows that, for a small value of Tabor's parameter, the Bradley-Hamaker and the DMT models have a good approximation for adhesion energy, and JKR is more applicable for larger values. For nanoparticles (sub-100nm) the Tabor's parameter is less than 0.1 and it applies to the Bradley-Hamaker and DMT models.

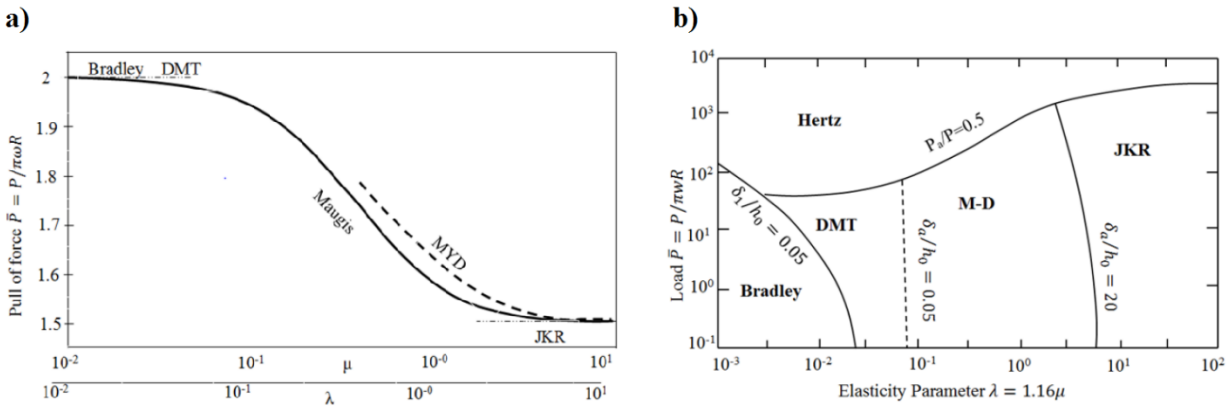

Figure 2-6 a)Tabor parameter for different contact models, b) map of different contact models [82] (open-access reference)

The JKR model studied soft spheres and the DMT model was provided for hard spheres. Maugis described the intermediate regime between the JKR and the DMT models. Plastic deformation was considered in the interaction of particles in the Maugis model. Figure 2-6b illustrates the pull-off force

based on the elasticity parameter ($\lambda = 1.16\,\mu$). Different elastic models are presented in this map. These models were also summarized in Raheleh and Tan's paper [51, 82, 89, 92-95].

Current contact models are derived based on continuum contact mechanics, although nanoparticles have a soft and discrete structure. Assuming nanoparticles as a continuum media is against the nature of nanoparticles. Deformation and dislocation of atoms on the surface of nanoparticles could cause major fluctuation in the contact force [96, 97].

2.4 Gas adsorption

Adsorption is one of the efficient and simple methods in separation or purification processes, and air quality control used in many applications; Desulfurization of biogas [98] to prevent operational problems, such as corrosion and environmental problems such as global warming or acid rain [99] is one of the applications of adsorption. Removal of toxic metals, dyes, and pesticides in aqueous media from industrial effluents [100-102], and removal of VOCs from the air [103-105] are other applications of this method. The common VOCs are BTX (benzene, toluene xylene), dichloromethane, trichloroethylene, and formaldehyde.

A successful adsorption process depends on the performance of the adsorbents. Examples of the adsorbent include activated carbon, sewage–sludge [106], silica gel [107], molecular sieves, polymeric adsorbents,[108] waste pomace, rice husk, sawdust, mustard oil cake, and mushrooms [101], Alumina, and Zeolite [54]. The surface atoms of a solid, which are coordinatively unsaturated with respect to the bulk atoms, become saturated due to the interaction with molecules of the environment.

In the adsorption process, molecules in the gas phase (or liquid) striking the adsorbent surface may either bounce back into the gas-phase or get adsorbed onto solid sites. The process is called chemisorption when the interaction between the adsorbed molecules and the surface leads to a chemical bond the process is called chemisorption; otherwise, the process is classified as physisorption. After

adsorption, the free energy of the system consisting of the clean surface and gas-phase molecules is lowered. Adsorbate energetics is given by the potential energy of adsorbate and it can be expressed by using quasi-one-dimensional Lennard-Jones potential, which describes the interaction between a surface and a gas-phase molecule that is approaching the surface as a superposition of a long-range attractive force and a short-range repulsive force [52, 53]. The interaction between adsorbate and adsorbent could result from van der Waals and double layer repulsion [109]. For gaseous media, where no reaction takes place, van der Waals is dominant.

2.4.1 Isotherm adsorption models

Adsorption equilibria information is the most important piece of information in an adsorption process. It can be used in the study of adsorption kinetics of single component, adsorption equilibria of multicomponent systems, and adsorption kinetics of multicomponent systems [54]. Adsorption isotherm is also used to compare the adsorption capacity of adsorbents for given substances [110].

Equilibrium relationships, generally known as adsorption isotherms due to the van der Waals, are classified by Brunauer and his co-workers into five characteristic types shown in Figure 2-7 [111]. Type I is the well-known Langmuir adsorption isotherm, and type II is the S-shaped or sigmoid isotherm; however, no names have been attached so far to the three other types. Types II and III are closely related to Types IV and V, only in the former cases the adsorption increases as the vapor pressure of the adsorbed gas is approached, whereas in the latter cases the maximum adsorption is attained, or almost attained, at some pressure lower than the vapor pressure of the gas [111].

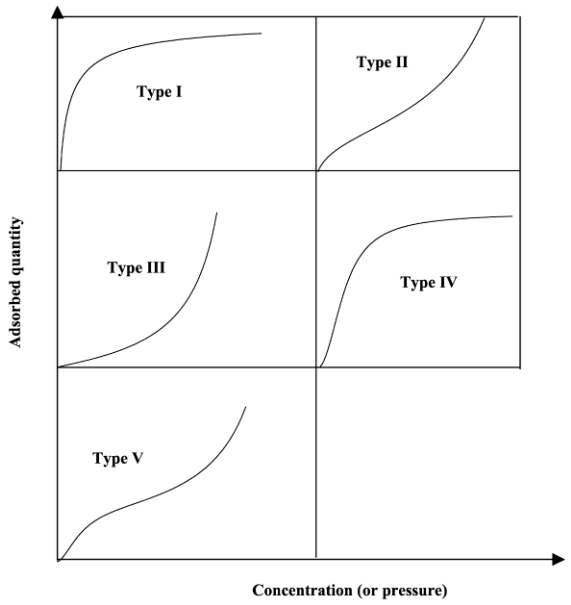

Figure 2-7 Classification of adsorption isotherms into five characteristic types (with permission from [110])

Foo and Hameed reviewed theoretical and empirical models of adsorption isotherms. They include Langmuir, Freundlich, Brunauer–Emmett–Teller, Redlich–Peterson, Dubinin–Radushkevich, Temkin, Toth, Koble–Corrigan, Sips, Khan, Hill, Flory–Huggins and Radke–Prausnitz isotherm [112]. Langmuir model is the basic isotherm adsorption model, which was proposed in (1918). It is a coherent model of adsorption onto a flat surface on the basis of kinetics; there is a continuous bombardment of molecules onto the surface and simultaneous evaporation (desorption) of molecules from the surface. As a result, it maintains zero accumulation at the surface at equilibrium. The assumptions of the Langmuir model are:

1. The surface is homogeneous and adsorption energy is constant over all the sites.
2. Adsorption on the surface is localized, which means that the adsorbed gas molecules are adsorbed at definite, localized sites.

3. Each site can accommodate only one gas molecule.

The Langmuir theory is based on a kinetic principle, that is the rate of adsorption, r_{ad} is equal to the rate of desorption, r_{des} from the surface [54]:

$$r_{ad} + r_{des} = 0 \tag{2-18}$$

The rate of adsorption, which is the striking rate, F at the surface multiplied by a sticking coefficient, S, sometimes called the accommodation coefficient is given by:

$$r_{ad} = FS \tag{2-19}$$

where F is the flux of molecules striking the surface per unit time and unit area. S is the sticking probability. Base on kinetic gas theory F is described as:

$$F = p/\sqrt{2\pi k_b T} \tag{2-20}$$

where p is the pressure. Since sticking probability depends on surface coverage, it is the product of initial sticking probability, a Boltzmann term with activation energy for adsorption E_{ad} and the function, $f(y)$. Substituting Equation (2-20) into Equation (2-19) gives:

$$r_{ad} = \frac{p}{\sqrt{2\pi k_b T}} s_0 \exp(-\frac{E_{ad}}{k_b T}) f(y) \tag{2-21}$$

It has been assumed in first-order Langmuir isotherm that sticking probability is proportional to the clean sites: $f(y) = 1 - y$. For second-order Langmuir isotherm, incident molecule consume two adsorption sites: $f(y) = (1 - y)^2$.

The desorption rate is given by the Polanyi-Wigner equation by:

$$r_{des} = -\nu(y)\, {\sigma_A}^n \exp\left(-\frac{E_{des}(y)}{k_b T}\right) y^n \tag{2-22}$$

where $\nu(y)$ is the frequency factor and σ_A is the density of adsorption sites.

2.4.2 Kinetic adsorption models

Except for adsorption capacity, the kinetic performance of a given adsorbent is also important engineering applications. From a kinetic analysis, the solute uptake rate, which determines the residence time required for completion of adsorption, may be established. In addition, one can determine the scale of an adsorption apparatus based on the kinetics. Generally, adsorption kinetics is the base to determine the performance of any flow-through systems [108].

Adsorption kinetic models are classified as adsorption reaction models and adsorption diffusion models. Both models are applied to describe the kinetics of adsorption; however, they are quite different. Adsorption diffusion models are normally developed following these three steps: (1) diffusion across the liquid film surrounding the adsorbent particles, i.e., external diffusion or film diffusion; (2) diffusion in the liquid contained in the pores and/or along the pore walls, which is so-called internal diffusion or intra-particle diffusion; and (3) adsorption and desorption between the adsorbate and active sites, i.e., mass action. However, adsorption reaction models originated from chemical reaction kinetics are based on the whole process of adsorption without considering these three steps [108].

A dynamic adsorption breakthrough process is based on material balance, gas phase, intra-fiber mass transfer, adsorption equilibrium, boundary conditions, and initial conditions [103]. The kinetic models are used to predict breakthrough behaviors. The breakthrough curve is a concentration-over-time profile.

Two commonly used empirical models in adsorption are Pseudo-first-order (PFO) and pseudo-second-order (PSO) models [113, 114]. Although PFO adsorption is considered as a diffusion-control model [115] and the PSO provides the best correlation of the experimental data of reaction control adsorption [116, 117], these statements are generally inaccurate when validated by a wide range of experimental data [114]. PFO and PSO constant rates are empirical and they depend on the process

conditions. The rate constant of PFO is decreased with increasing initial concentration [118-120]. Moreover, small particle size causes a reduction in the constant rate of PFO [121].

The PFO and PSO models lack a theoretical basis, and they provide little insight into the controlling mechanisms [114]. Later on, a study attempted to establish a theoretical basis for them [122]. According to this research, PFO fits better for high initial concentration, and PSO is applicable to low initial concentration cases. There are other adsorption–diffusion models including pore diffusion models such as Crank model [123], Vermeulen model [124] and its linear form Dumwald-Wagner model [125], Weber-Morris IPD model [126], Bangham model [127], and external diffusion model as Linear Film Diffusion model [106], which is the transport of adsorptive from the bulk phase to the external surface of the adsorbent, mixed surface reaction and diffusion-controlled kinetic model (MSRDCK) [128], and multi-exponential model [129].

2.5 Interfacial interaction between entities

2.5.1 Intermolecular interaction

Intermolecular forces can be attractive or repulsive, short-ranged or long-ranged, strong or weak, isotropic or directional, *etc.*. Generally, different types of interactions are listed in Table 2-2, where, $w(r)$ is the interaction free energy or pair-potential (J); Q_e, electric charge (C); r is the center to center distance (m); U, electric dipole moment (Cm); α, electric polarizability ($C^2m^2J^{-1}$); k_b, Boltzmann constant ($1.381 \times 10^{-23} JK^{-1}$); T, absolute temperature (K); h, Planck's constant ($6.626\ \ 10^{-34}$ Js); v, electric absorption (ionization) frequency (s^{-1}); and ε_0, dielectric permeability of free space ($8.85\times 10^{-12}\ C^2J^{-1}m^{-1}$). The force $F(r)$ is obtained by $F = -dw(r)/dr$. Covalent interaction occurs when two atoms or molecules connect with chemical bonds. Covalent forces are strong short-range in the order of interatomic separations (0.1–0.2 nm). Interactions with a purely electrostatic origin, while one of the molecules is changed. They are often strong and long-range. Especially when two molecules are charged, it decays slowly over distance (*1/r*).

Table 2-2 Types of interactions and their pair-potentials w(r) between two atoms, ions, or small molecules in a vacuum (reproduced from [51] with permission)

	Type of interaction	Interaction energy *w (r)*
Covalent, metallic	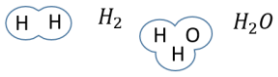	Complicated, short-range
Charge-charge	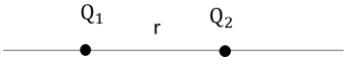	$+Q_1Q_2/4\pi\varepsilon_0 r$ (Coulomb energy)
Charge-dipole	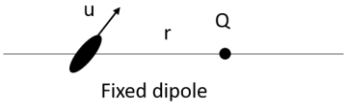	$-Q_e U\ \cos\theta/4\pi\varepsilon_0 r^2$
	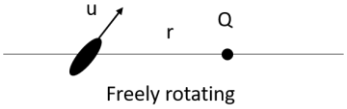	$-{Q_e}^2U^2/6(4\pi\varepsilon_0)^2k_bTr^4$
Dipole-dipole	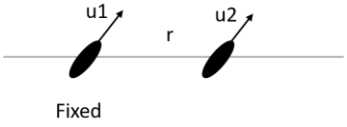	$\frac{-U_1U_2[2\cos\theta_1\ \cos\theta_2-\sin\theta_1\sin\theta_2\cos\phi]}{4\pi\varepsilon_0 r^3}$
	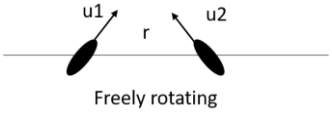	$-{U_1}^2{U_2}^2/3(4\pi\varepsilon_0)^2k_bTr^6$ (Keesom energy)
Charge-non-polar	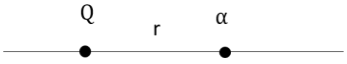	$-{Q_e}^2\alpha/2(4\pi\varepsilon_0)^2r^4$
Dipole-no-polar	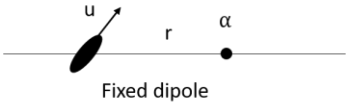	$-U^2\alpha\ (1+3\cos^2\theta)/2(4\pi\varepsilon_0)^2r^6$
	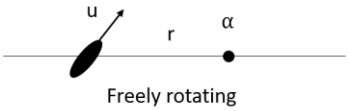	$-U^2\alpha/(4\pi\varepsilon_0)^2r^6$ (Debye energy)
Two non-polar molecules	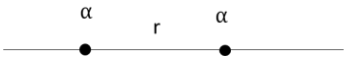	$-\frac{3}{4}\frac{h\nu\alpha^2}{(4\pi\varepsilon_0)^2r^6}$ (London dispersion energy)
Hydrogen bond	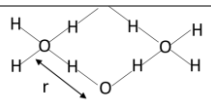	Complicated, short-range, energy roughly proportional to $-1/r^2$

Dipole-dipole, dipole-nonpolar, and two non-polar molecular interaction are from other types of intermolecular forces originated from quantum mechanics due to the electric field of electron clouds on other molecules. The contribution of these three forces is known as the van der Waals force. They are long-range and act from 0.2 nm to 100 nm but decay very fast ($1/r^6$). The hydrogen bonding interaction is a special case of dipole-dipole interaction, where one of the atoms are hydrogen. Due to the bond length, this kind of interaction is stronger than the dipole-dipole interaction.

Van der Waals force consists of three different interactions between dipoles: the Keesom interaction (orientation force), the Debye interaction (induction force), and the London interaction (dispersion force). The Keesom interaction is the interaction between the permanent dipole moment of polar molecules. This interaction energy is given as:

$$w(r) = \frac{-U_1^2 U_2^2}{3(4\pi\varepsilon_0)^2 k_b T r^6} \tag{2-23}$$

The Debye interaction is the interaction between the permanent dipole moment of the polar molecule and the induced dipole moment. It is given as:

$$w(r) = \frac{-U^2 \alpha_0}{(4\pi\varepsilon_0\varepsilon)^2 r^6} \tag{2-24}$$

The London interaction is due to the induced instantaneous dipole polarization [130], given by:

$$w(r) = \frac{-\frac{3}{4}\alpha_0^2 h\nu}{(4\pi\varepsilon_0)^2 r^6} \tag{2-25}$$

where α_0 is the electronic polarizability ($\mathrm{C^2 m^2 J^{-1}}$), h is the Planck constant (6.626×10^{-34} Js) and ν is the orbiting frequency of electron (s^{-1}). All these three forces are proportional to $1/r^6$. Van der Waals force is equal to:

$$w_{vdw}(r) = -\frac{C_{vdw}}{r^6} = -\frac{C_{ind} + C_{orient} + C_{disp}}{r^6} \tag{2-26}$$

For dissimilar molecules, van der Waals interaction is an intermediate value between the interactions of similar molecules for both dissimilar molecules; however, for highly polar dissimilar molecules Equation (2-26) is no longer valid. Moreover, the London theory of dispersion forces has deficiencies. It cannot handle the interactions of molecules in a solvent, and it also assumes one absorption frequency for all molecules. Moreover, London equation is not consistent with the experiment for the molecules larger than 0.5 nm.

McLachlan (1963)'s general theory overcome these deficiencies. He proposed an expression for van der Waals force including induction, orientation, and dispersion forces.

$$w(r) = -\frac{C_{vdw}}{r^6} = -\frac{6k_bT}{(4\pi\varepsilon_0)^2 r^6} \sum_{n=0}^{\infty} \frac{\alpha_1(iv_n)\alpha_2(iv_n)}{\varepsilon_3^2(iv_n)} \tag{2-27}$$

where $\alpha_1(iv_n)$ and $\alpha_2(iv_n)$ are the polarizabilities of molecules 1 and 2, and $\varepsilon_3\ (iv_n)$ is the electric permittivity of medium 3 at different frequencies (v). The total polarizability of a molecule as a function of imaginary frequencies (iv_n) is:

$$\alpha(iv_n) = \frac{U^2}{3k_bT(1 + \frac{v_n}{v_{rot}})} + \frac{\alpha_0}{1 - \kappa\left(\frac{v_n}{v_I}\right) + \left(\frac{v_n}{v_I}\right)^2} \tag{2-28}$$

The first term of Equation (2-28) is due to the rotating of dipoles and the second term is a fixed electrical polarity, where v_{rot} is the rotational relaxation frequency for the molecule average, v_I is the ionization frequency and κ is the damping coefficient.

2.5.2 Nanoparticle interactions

Interaction potentials between macroscopic bodies have the same origin of intermolecular potential. With the assumption of only attractive interaction potential between two atoms or small molecules

($w(r) = -C/r^n$) and additivity, the interaction potential between macroscopic bodies will be the sum of all the molecules in body 1 interactions with all molecules in the body 1 (Figure 2-8). Therefore, the interaction potential between a molecule and a flat surface is:

$$w(D) = -2\pi C\rho \int_{z=D}^{z=\infty} dz \int_{x=0}^{x=\infty} \frac{xdx}{(z^2+x^2)^{\frac{n}{2}}} = \frac{2\pi C\rho}{(n-2)} \int_D^{\infty} \frac{dz}{z^{n-2}} \qquad (2\text{-}29)$$

$$= -\frac{2\pi C\rho}{(n-2)(n-3)D^{n-3}} \qquad for\ n > 3$$

where ρ is the number density of molecules in the solid (m^{-3}), and D is separation distance. For n=6 van der Waals force Equation (2-29) is reduced to:

$$w(D) = -\frac{\pi C\rho}{6D^3} \qquad (2\text{-}30)$$

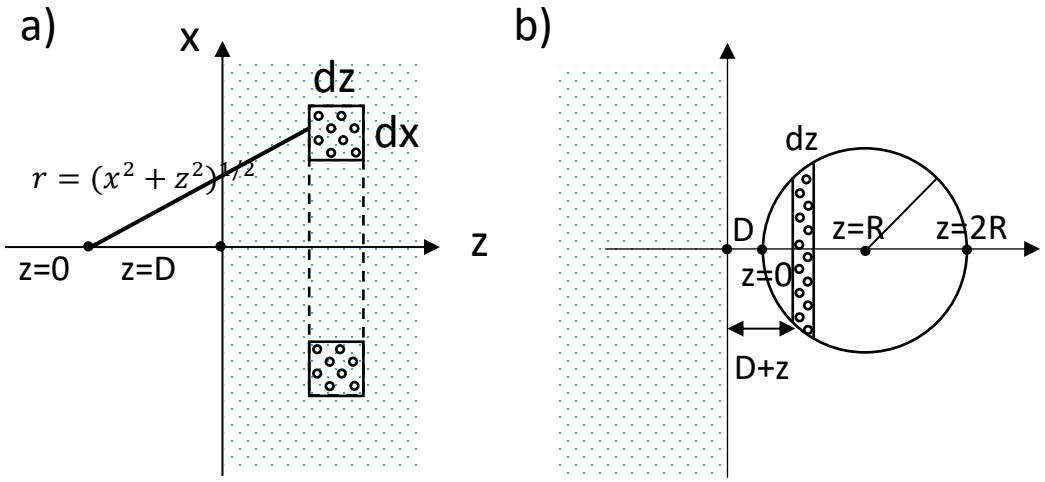

Figure 2-8 Interaction potential between, a) a molecule and a flat surface, b) a spherical particle and a flat surface (reproduced with permission from [51])

With the same procedure, the interaction between a spherical particle and a surface or other two macroscopic bodies is obtained. Van der Waals interaction energy W and force F between some macroscopic bodies of different geometries are listed in Table 2-3. A is the Hamaker constant which is determined by:

$$A = \pi^2 C \rho_1 \rho_2 \tag{2-31}$$

Table 2-3 Van der Waals interaction energy W and force F between macroscopic bodies of different geometries (reproduced from[51] with permission)

The geometry of bodies with surface D apart (D<<R)	Van der Waals interaction	
	Energy, W	Force, $F = -dW/dD$
Two atoms and small molecules	$-C/r^6$	$-6\,C/r^7$
Two flat surfaces (per unit area)	$-A/12\pi D^2$	$-A/6\pi D^3$
Two spheres or macromolecules of radius R_1 and R_2	$\frac{-A}{6D}\left(\frac{R_1 R_2}{R_1+R_2}\right)$	$\frac{-A}{6D^2}\left(\frac{R_1 R_2}{R_1+R_2}\right)$
Sphere or macromolecule of radius R near a flat surface	$-AR/6D$	$-AR/6D^2$
Two parallel cylinders or rods of radius R_1 and R_2 (per unit length)	$\frac{-A}{12\sqrt{2}D^{3/2}}\left(\frac{R_1 R_2}{R_1+R_2}\right)^{1/2}$	$\frac{-A}{8\sqrt{2}D^{5/2}}\left(\frac{R_1 R_2}{R_1+R_2}\right)^{1/2}$
A cylinder of radius R near a flat surface (per unit length)	$\frac{-A\sqrt{R}}{12\sqrt{2}D^{3/2}}$	$\frac{-A\sqrt{R}}{8\sqrt{2}D^{5/2}}$
Two cylinders or filament of radius R_1 and R_2 crossed at 90^0	$\frac{-A\sqrt{R_1 R_2}}{6D}$	$\frac{-A\sqrt{R_1 R_2}}{6D^2}$

The expressions for different geometries listed in Table 2-3 are valid for $d \gg R$. Hamaker (1937) derived a general equation for van der Waals interaction energy or pair potential between two spheres for all separations as:

$$w(D) = -\frac{A}{6}\left\{\frac{2R_1R_2}{(2R_1+2R_2+D)D} + \frac{2R_1R_2}{(2R_1+D)(2R_2+D)} + \ln\frac{(2R_1+2R_2+D)D}{(2R_1+D)(2R_2+D)}\right\} \quad (2\text{-}32)$$

The additivity of van der Waals interaction has been ignored in the derivation of the interaction potential between macroscopic geometries; however, the influence of neighboring atoms on the interaction between any pair of atoms is substantial, especially when bodies interact in condensed media[131]. Lifshitz's theory (1956) tries to avoid additivity by solving the problem by continuum mechanics. In this theory, all expressions for interaction remain unchanged except for the Hamaker constant. The Hamaker constant is derived in terms of bulk properties as their dielectric constants and refractive indices.

$$A \approx \frac{3}{4}k_bT\left(\frac{\varepsilon_1-\varepsilon_2}{\varepsilon_1+\varepsilon_3}\right)\left(\frac{\varepsilon_2-\varepsilon_3}{\varepsilon_1+\varepsilon_3}\right) + \frac{3h}{4\pi}\int_{v1}^{\infty}\left(\frac{\varepsilon_1(iv)-\varepsilon_3(iv)}{\varepsilon_1(iv)+\varepsilon_3(iv)}\right)\left(\frac{\varepsilon_2(iv)-\varepsilon_3(iv)}{\varepsilon_2(iv)+\varepsilon_3(iv)}\right)dv \quad (2\text{-}33)$$

For the same adsorption frequency, the expression will be simplified to:

$$A_{total} = A_{v=0} + A_{v>0} = \frac{3}{4}\,k_bT\left(\frac{\varepsilon_1-\varepsilon_3}{\varepsilon_1+\varepsilon_3}\right)\left(\frac{\varepsilon_2-\varepsilon_3}{\varepsilon_2+\varepsilon_3}\right) + \frac{3h\nu_e}{8\sqrt{2}}\frac{(n_1^2-n_3^2)(n_2^2-n_3^2)}{(n_1^2+n_3^2)^{1/2}(n_2^2+n_3^2)^{1/2}\{(n_1^2+n_3^2)^{1/2}+(n_2^2+n_3^2)^{1/2}\}} \quad (2\text{-}34)$$

Deriving the Hamaker constant for macroscopic bodies from this theory agreed well with experiments [51]. However, it deviated for interaction between intermediate nanoparticles. Hamaker constants of metal nanoparticles vary with their sizes due to the scattering of free conducting electrons and consequent size dependency of the dielectric permittivity [131-134].

2.6 Knowledge gaps

Separation and deposition of entities underlie the principles of gas adsorption and air filtration. In conventional filtration models, diffusion is the dominant mechanism of nanoparticles filtration. It is worth noting that particle diffusion triggers the collision of particles to the single fiber's surface through a steady process. Based on the classical filtration models, all particles that collide on the surface will adhere to it, and the total efficiency of a filter media is determined by a correlating mass balance to single-fiber efficiency. The theoretical filtration models cannot predict the filtration efficiency for a wide range of parameters, including particle size, fiber size, material property, and face velocity. Moreover, when the size of the particles approaches intermediate sizes, the deposition procedure on the nanofibrous filter is still unclear.

When particles approach the size of gas molecules, their behavior might be different from a normal aerosol. Molecules can be collected on a surface by adsorption. In adsorption, molecules in the gas-phase (or liquid phase) are deposited on the solid adsorbent surface because of their interfacial interaction. In kinetic adsorption models, three steps are known for mass transfer through continuous mode, including Step 1: external diffusion, Step 2: pore diffusion, and Step 3: adsorption/desorption. Step 3 is the attachment of the adsorbate to the internal surface of the adsorbent. In the diffusion-driven kinetic adsorption models, diffusion is a dynamic process. Diffusion is investigated throughout the media and the velocity is assumed constant. The diffusion is analyzed on the basis of mass balance, when mass concentration is the intended parameter and the size of entities is an insignificant parameter. The mass transfer coefficient between bulk gas and surface is mostly assumed constant. Despite the clear and smooth surface of activated carbon nanofibers [135], the second step (pore diffusion) is considered for the deposition on the surface of activated carbon fibers in some studies. A proper model is needed for the adsorption of entities on nanofibers. The third step is dominant in the adsorption in the reaction control models.

The adsorption isotherm models consider adhesion coefficient or adhesion probability for imperfect adhesion, where only a fraction of striking molecules can be adsorbed. Moreover, the importance of initial concentration on deposition has been shown in experimental studies and kinetic adsorption models. Although the uptake capacity of adsorption increases with initial concentration, the adsorption efficiency decreases.

The deposition of intermediate nanoparticles should be interpreted with neither complete filtration nor adsorption. The interfacial interaction due to van der Waals force may bridge the gap between molecules and normal nanoparticles, as the particle size approaches molecular scale, the action of interfacial interactions before and after collision becomes crucial. However, the effects interfacial interactions on the deposition of intermediate nanoparticles are not clear. Addressing all the current knowledge gaps may provide a better understanding of the deposition of entities on the fibers.

2.7 Conclusions

This chapter discusses the nanoparticle filtration, adsorption, intermolecular, and inter-particular interfacial interaction. The assumption of 100% adhesion probability becomes uncertain for intermediate nanoparticles colliding on nanofibers. This lack of fundamental knowledge of adhesion is also pointed out by several studies. To address the aforementioned knowledge gap, a theoretical model is required to consider the interfacial interaction between particles and surface in the deposition of intermediate nanoparticles on the nanofibers.

Chapter 3
Effects of interfacial interaction and air flow on the deposition of nanoparticles

3.1 Summary

This chapter presents a model to predict the rate of particles diffusing to the surface of a single fiber. The rate of collision based on convective diffusion and interfacial interactive diffusion is obtained using boundary layer analysis around a single fiber. In addition to the airflow, particles are under another streamline due to the van der Waals force. This model is validated using experimental data in literature.

3.2 Introduction

Filtration using fibrous media is used in many industries, including respiratory protection, air cleaning, processing of nuclear wastes, dust collection at power plants, and clean rooms [79, 80]. Low basis weight, high permeability, tight pore size, and large surface area to volume ratio of nanofibers improve filtration performance by increasing the probability of nanoparticle deposition. They also operate at high flow rates with low-pressure drops [38, 79, 81-83]. Nanofibrous filters can be produced by various technologies such as electrostatic spinning, melt-blown technique, and multicomponent fiber spinning. Among them, electrospinning technology is the most prevalent method which can produce fibers of diameter as small as 40nm. Generally, the nanofibrous filters can be engineered for a wide range of diameters (40-2000 nm) and 80–90% filter porosity [81, 83].

The total filtration efficiency of nanofibrous filters can be calculated based on classical filtration models that was first proposed by Spumy and Pich [84], where the total filtration efficiency is derived from single-fiber filtration efficiency by a one-dimensional analysis. It is assumed that the filter has a uniform packing density, that all fibers are straight with the same diameter, that all fibers are perpendicular to the flow direction, and that the single-fiber efficiency remains unchanged along with

the depth of the filter [38]. In all aerosol filtration models, it is assumed that the fiber is clean [38]. Aerosol particles are deposited on the fiber by different mechanisms such as diffusion, inertia, interception, or a combination of them. The total single-fiber efficiency due to these mechanisms can be calculated using additivity rules or independence rules, however, several models considered a combination of these mechanisms; for instance, the simultaneous action of convective diffusion and interception is considered in [136-138], simultaneously. In the additivity rules, by adding the efficiencies due to the various mechanisms the total efficiency is overestimated [85]. According to the independence rules, the total penetration is equal to the product of penetration for the individual mechanisms.

Brownian diffusion is considered as an effective mechanism of filtration for nanoparticles. The single-fiber efficiency due to convective Brownian motion is calculated from the convective diffusion equation, where the flow field around the fiber plays a major role.

Friedlander [139] and Natanson [140] investigated the mechanism of diffusion using various flow field models around an isolated fiber from [141] and [142], respectively. Kuwabara [143] and Happel [144] derived a cell model for the flow field for a system of parallel fibers for low Reynolds number by considering the effect of neighboring fibers interference in the flow field. Pich (1965) derived a single-fiber efficiency model using a modified Happel-Kuwabara flow field considering the slip effect at the surface of the fiber [145]. Stechkina and Fuchs (1966) used the Happel-Kuwabara flow filed while believing that due to the low Knudsen number the slip effect at the surface should not be taken into consideration [136]. Yeh and Liu also modified the Happel-Kuwabara flow field allowing for slip effects to determine single-fiber efficiency. However, they concluded that the Kuwabara's flow field provides a good approximation for the flow around the fiber when Reynolds number is less than 1[138]. Spielman and Goren [146] calculate the pressure drop and filtration efficiency for airflow through fibrous media based on the Brinkman flow field [147]. The Brinkman flow field also considers a group

of fibers. Lee and Liu [148] determined a single-fiber efficiency based on the well-accepted Kwabara flow field. Hunt, Thajudeen, *et al*. determined single-fiber efficiency without restricted boundary conditions by considering the particle deposition as a collision phenomenon [149]. In addition to the theoretical models for single-fiber efficiency due to the diffusion, several empirical models were developed [150-155]. However, none of the aforementioned theoretical models were verified for a broad range of fiber and particle and fiber sizes, especially for nano fibers.

The effects of interfacial interaction on the transport of nanoparticles to the nanofiber surface are barely investigated. Van der Waals, as well as other transport or collision mechanisms, can move the particles to the surface causing collision; the effects of van der Waals forces on the filtration of nanoparticles have been investigated [35, 36]. Nanoparticles are transported to nanofiber mat based on van der Waals force at low face velocities around 1 cm/s [35] or where the ratio of fiber to particle size approaches unity [36], even by considering the retardation effect [156]. However, no validated model has been reported yet.

This study aimed to develop a new transport model for nanoparticles. The rate of collision on the fiber surface based on convective diffusion and interfacial interactive diffusion is obtained using boundary layer analysis around a single fiber. This model is verified with 31 experimental data from the literature for a variety of parameters.

3.3 Model Development

Considering a single fiber in stationary air containing nanoparticles with a free-stream particle concentration, n_0 in Figure 3-1a, the nanoparticles close to the surface gradually collide on and adhere to the fiber. After a while, more nanoparticles are diffused to the fiber surface driven by the radial concentration gradient. Considering a particle-laden flow (with free stream particle concentration n_0) passing a cylindrical single fiber (Figure 3-1b), the concentration of the flow around the fiber is

decreased due to the deposition of particles on the fiber. As a result, a concentration boundary layer (CBL), is developed around the fiber (Figure 3-1c). Within the CBL, nanoparticles could diffuse to the fiber surface due to the concentration gradient between the mainstream and fiber surface. In the CBL, the concentration gradient drives particle to diffuse towards the fiber surface, and there is no radial flux due to the diffusion outside the CBL.

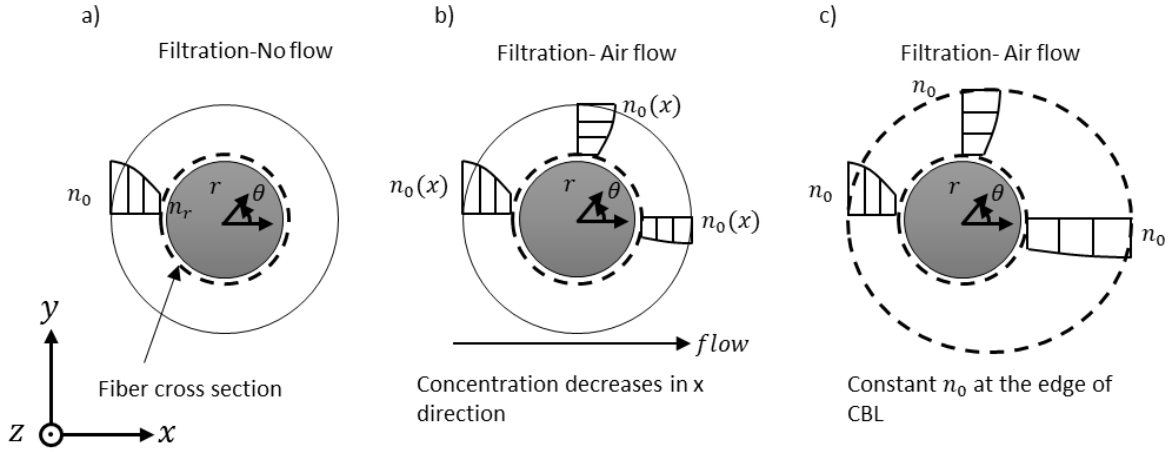

Figure 3-1 The model for collision of nanoparticles on a single fiber a) no airflow, b) in the presence of airflow, and c) with concentration boundary layer around the single fiber

Convection of nanoparticles to the CBL leads to their diffusion to the fiber surface. In other words, the streamflow brings the nanoparticles into the boundary layer and then they collide on the fiber surface, due to the concentration gradient in the CBL. This process is mathematically described by [139]:

$$u_r \frac{\partial n}{\partial r} + \frac{u_\theta}{r} \frac{\partial n}{\partial \theta} = D \left(\frac{\partial^2 n}{\partial r^2} + \frac{1}{r} \frac{\partial n}{\partial r} + \frac{\partial^2 n}{r^2 \partial \theta^2} \right) \quad (3\text{-}1)$$

where n is the number concentration; u_r and u_θ are radial and tangential velocity components, respectively; D is the diffusion coefficient. The concentration gradient is zero on the edge of the CBL, and concentration is almost equal to the concentration in the free stream. : $\frac{\partial n}{\partial r} = 0,\ n = n_0(\theta)$ at $r = \rho(\theta)$. The concentration at the bottom of CBL (*i.e.,* fiber surface), is assumed to be constant and $n_r \neq 0$. The concentration at the fiber surface is assumed zero in other classical filtration models and all nanoparticles that collide on the fiber surface are assumed to adhere to it. In this model, however, the adhesion probability is not unity molecules and intermediate nanoparticles. Since the upstream air flow rate is constant and nanoparticles constantly enter the CBL, then it can be assumed that the rate of nanoparticles colliding on the surface is constant ($n = n_r$ at $r = R_f$).

Because of the thin boundary layer around the fiber, the third term on the right-hand side (RHS) of Equation (3-1) is ignored. Therefore, it is can be simplified as:

$$u_r \frac{\partial n}{\partial r} + \frac{u_\theta}{r}\frac{\partial n}{\partial \theta} = \frac{D}{r}\frac{\partial}{\partial r}\left(r\frac{\partial n}{\partial r}\right) \tag{3-2}$$

The chain rule for coordinate system transforming from (r, θ) to (ψ, θ) gives:

$$\frac{\partial n}{\partial \theta} = \frac{\partial n}{\partial \psi}\frac{\partial \psi}{\partial \theta} + \frac{\partial n}{\partial \theta}\frac{\partial \theta}{\partial \theta} = r u_r \frac{\partial n}{\partial \psi} + \frac{\partial n}{\partial \theta} \tag{3-3}$$

$$\frac{\partial n}{\partial r} = \frac{\partial n}{\partial \psi}\frac{\partial \psi}{\partial r} + \frac{\partial n}{\partial \theta}\frac{\partial \theta}{\partial r} = -u_\theta \frac{\partial n}{\partial \psi} \tag{3-4}$$

$$\frac{\partial}{\partial r}\left(r\frac{\partial n}{\partial r}\right) = \frac{\partial}{\partial \psi}\left(r\frac{\partial n}{\partial r}\right)\frac{\partial \psi}{\partial r} = -u_\theta \frac{\partial}{\partial \psi}\left(r\frac{\partial n}{\partial r}\right) \tag{3-5}$$

Substituting Equations (3-3), (3-4), and (3-5) in Equation (3-1) gives:

$$u_r\left(-u_\theta \frac{\partial n}{\partial \psi}\right) + \frac{u_\theta}{r}\left(r u_r \frac{\partial n}{\partial \psi} + \frac{\partial n}{\partial \theta}\right) = -u_\theta \frac{D}{r}\frac{\partial}{\partial \psi}\left(r\frac{\partial n}{\partial r}\right) \tag{3-6}$$

Or

$$\frac{\partial n}{\partial \theta} = -D\frac{\partial}{\partial \psi}\left(r\frac{\partial n}{\partial r}\right) \tag{3-7}$$

Integration from both sides of Equation (3-7) with respect to ψ gives:

$$\int \frac{\partial n}{\partial \theta}\, d\psi = -\int D\frac{\partial}{\partial \psi}\left(r\frac{\partial n}{\partial r}\right) d\psi \tag{3-8}$$

According to Leibniz integral rules:

$$\frac{\partial}{\partial \theta}\int_0^{\psi_\rho(\theta)} n(\psi,\theta)\, d\psi = n_0\frac{\partial \psi_\rho(\theta)}{\partial \theta} - n_r\frac{\partial \psi_{Rf}(\theta)}{\partial \theta} + \int_0^{\psi_\rho(\theta)}\frac{\partial n}{\partial \theta}\, d\psi \tag{3-9}$$

where $\psi_{Rf}(\theta) = 0$. The LHS of Equation (3-8) is replaced with Equation (3-9):

$$\frac{\partial}{\partial \theta}\int_0^{\psi_\rho(\theta)} n(\psi,\theta)d\psi - n_0\frac{\partial \psi_\rho(\theta)}{\partial \theta} = -\int D\frac{\partial}{\partial \psi}\left(r\frac{\partial n}{\partial r}\right) d\psi \tag{3-10}$$

The RHS of Equation (3-10) is replaced with:

$$-\int D\frac{\partial}{\partial \psi}\left(r\frac{\partial n}{\partial r}\right) d\psi = -D\left[\left(\rho(\theta)\frac{\partial n}{\partial r}\right)_{\psi_\rho(\theta)} - \left(R_f\frac{\partial n}{\partial r}\right)_{R_f}\right] \tag{3-11}$$

Since $\left(\frac{\partial n}{\partial r}\right)_{\psi_\rho(\theta)} = 0$ at the edge of the CBL, Equation (3-10) becomes:

$$n_0\frac{\partial \psi_\rho(\theta)}{\partial \theta} - \frac{\partial}{\partial \theta}\int_{n_r}^{n_0}\psi dn - n_0\frac{\partial \psi_\rho(\theta)}{\partial \theta} = D\left(R_f\frac{\partial n}{\partial r}\right)_{R_f} \tag{3-12}$$

$$-\frac{\partial}{\partial \theta}\int_{n_r}^{n_0}\psi dn = DR_f\left(\frac{\partial n}{\partial r}\right)_{R_f}$$

The rate of nanoparticles entering the boundary layer at θ is defined as $N = \int_{n_r}^{n_o}\psi\, dn$. The gradient of N shows the number of nanoparticles striking the fiber surface. The total rate of nanoparticles colliding on the surface is obtained by integrating the gradient of rate for particle movement to the surface to the unit length of fiber:

$$N_t = 2\int_0^{\pi} \frac{\partial N}{\partial \theta}\, d\theta \tag{3-13}$$

Defining dimensionless quantities $\rho' = \frac{\rho}{R_f}$, $n' = \frac{n-n_r}{n_0-n_r}$, $r' = \frac{r}{R_f}$, and $\psi' = \frac{\psi}{u\,R_f}$, Equation (3-12) becomes:

$$-\frac{\partial}{\partial \theta}\int_0^1 \psi'\, dn' = \frac{D}{u\,R_f}\frac{dn'}{dr'}\Big|_{r'=1} \tag{3-14}$$

Or

$$-\frac{\partial N'}{\partial \theta} = \frac{D}{u\,R_f}\frac{dn'}{dr'}\Big|_{r'=1} \tag{3-15}$$

Two stream functions contribute to the diffusion in Equation (3-13). The rate of nanoparticles to the fiber due to each flow is considered separately because each of them has a specific boundary layer thickness. Then, the combined effect will be considered for collision efficiency. The collision efficiency of nanoparticles that diffused to the fiber when they enter the boundary layer either by van der Waals force or convection is calculated from the product of penetrations due to individual stream flows by independence rules:

$$\eta_c = 1 - (1 - C'_d\, N'_{t-vdw})(1 - C_d\, N'_{t-f}) \tag{3-16}$$

where C'_d and C_d are correction factors. N'_{t-f} is the dimensionless total rate of collision due to convection and N'_{t-vdw} is the dimensionless total rate of collision due to the van der Waals force. The dimensionless rate of collision N' times a correction factor shows the collision efficiency due to each stream. The correction factors are necessary because the dimensional rates surpass unity. The correction factors can be determined by comparing experiments to the model, which will be discussed in Results section. The dimensionless total rates of nanoparticles colliding on the fiber surface due to the convection and van der Walls force are determined in 3.3.1 and, respectively.

3.3.1 Derivation of collision rate based on airflow

The contribution of convection to the dimensionless rate of nanoparticles moving to the surface is given as:

$$N'_f = \int_0^1 \psi'_f \, dn' \tag{3-17}$$

The stream function of airflow over the fiber, ψ_f, is approximated using the Kuwabara flow field by considering randomly-distributed fibers [143]. The dimensionless stream function is given as:

$$\psi'_f = \frac{1-\alpha}{\mathrm{Ku}\, r'}(r'-1)^2 \sin(\theta) \tag{3-18}$$

where Ku is the Kuwabara hydrodynamic factor, and α is the solidity of filter:

$$\mathrm{Ku} = -0.5 \ln \alpha - 0.75 - 0.25\alpha^2 + \alpha \tag{3-19}$$

Substituting the dimensionless stream function of Kuwabara flow (Equation (3-18)) into Equation (3-14) gives:

$$N'_f = \int_0^1 \frac{1-\alpha}{\mathrm{Ku}\, r'}(r'-1)^2 \sin(\theta)\, dn' \tag{3-20}$$

$$= \frac{(1-\alpha)\ \sin(\theta)}{\mathrm{Ku}} \int_0^1 \frac{(r'-1)^2}{r'} dn'$$

The concentration gradient near the fiber surface can be estimated using Fick's second law ($\frac{dn'}{dr'} = \frac{1}{r' \ln(\rho')}$). Thus, Equation (3-20) gives:

$$N'_f = \frac{(1-\alpha)\ \sin(\theta)}{\mathrm{Ku}\ \ln(\rho')} \int_0^1 \frac{(r'-1)^2}{r'} \frac{1}{r' \ln(\rho')} dr' \tag{3-21}$$

$$= \frac{(1-\alpha)\ \sin(\theta)}{\mathrm{Ku}\ \ln(\rho')} \left[\rho' - \frac{1}{\rho'} - 2\ln(\rho')\right]$$

A logarithm can be approximated by Taylor series expansion while a variable, say *x*, is close to unity:

$$\ln(x) = (x-1) + \frac{(x-1)^2}{2} + \frac{(x-1)^3}{3} + \cdots$$

Or

$$\ln(x) = \left(1 - \frac{1}{\mathrm{x}}\right) + \frac{1}{2}\left(1 - \frac{1}{\mathrm{x}}\right)^2 + \frac{1}{3}\left(1 - \frac{1}{\mathrm{x}}\right)^3 + \cdots$$

Therefore $\ln(\rho')$ can be approximated as $(\rho' - 1)$ or $\left(1 - \frac{1}{\rho'}\right)$ then:

$$N'_f = -\frac{(1-\alpha)\sin(\theta)}{\mathrm{Ku}} \cdot \frac{(\rho' - 1)}{\rho'} \tag{3-22}$$

Or

$$\frac{(\rho' - 1)}{\rho'} = -\frac{N'_f \,\mathrm{Ku}}{(1-\alpha)\sin(\theta)} \tag{3-23}$$

Substituting concentration gradient into Equation (3-15) gives:

$$-\frac{\partial N'}{\partial \theta} = \frac{D}{u\, R_f} \frac{1}{\ln(\rho')} \tag{3-24}$$

The term $\ln(\rho')$ in Equation (3-24) is replaced with Equation (3-23), thus:

$$\frac{N'_f \,\mathrm{Ku}}{(1-\alpha)\sin(\theta)} \frac{\partial N'_f}{\partial \theta} = \frac{D}{u\, R_f} \tag{3-25}$$

Rearrangement of Equation (3-25) gives:

$$N'_f \, dN'_f = \frac{D\,(1-\alpha)\sin(\theta)}{\mathrm{Ku}\, R_f\, u}\, d\theta \tag{3-26}$$

Getting integral from both sides of Equation (3-26) gives:

$$\frac{{N'_f}^2}{2} = -\frac{D\,(1-\alpha)}{\mathrm{Ku}\, R_f u}\cos(\theta) + c_0 \tag{3-27}$$

By assuming a negligible rate at $\theta = 0$, the constant c_0 can be determined:

$$c_0 = \frac{D\,(1-\alpha)}{\mathrm{Ku}\,R_f u} \tag{3-28}$$

The dimensionless rate of nanoparticles moving to the fiber surface is calculated as:

$$N'_f = \sqrt{\frac{4\,D\,(1-\alpha)}{u\,R_f\,\mathrm{Ku}}[1-\cos(\theta)]} \tag{3-29}$$

Integration of the gradient of rate for particle movement to the surface ($\frac{\partial N'}{\partial \theta}$) over the fiber surface gives the total dimensionless gradient of the rate of moving to the unit length of the fiber.

$$\begin{aligned} N'_{t-f} &= 2\int_0^{\pi} \frac{\partial N'_f}{\partial \theta}\, d\theta \\ &= 4\sqrt{\frac{(1-\alpha)}{\mathrm{Pe\ Ku}}} \end{aligned} \tag{3-30}$$

where Pe is the Peclet number:

$$\mathrm{Pe} = \frac{d_f u}{D} \tag{3-31}$$

In this equation, D is the diffusion coefficient. In the Einstein relation for the diffusion coefficient, it is assumed that Brownian particles do not interact with each other [157]:

$$D = \frac{k_b\,T C_c}{3\pi d_p \mu} \tag{3-32}$$

where C_c the slip correction factor is considered for nanoparticles based on Cunningham correlation in the gas flow [158]:

$$C_c = 1 + \mathrm{Kn_p}\left[1.257 + 0.4\exp\left(-\frac{1.1}{\mathrm{Kn_p}}\right)\right]^{1/3} \tag{3-33}$$

where $\mathrm{Kn_p}$ is the particle Kundesn number ($\mathrm{Kn_p} = \frac{2\lambda}{d_p}$).

3.3.2 Derivation of collision rate based on van der Waals force

Contribution of van der Waals force to the rate of nanoparticles moving to the surface is given as:

$$N'_{vdw} = \int_0^1 \psi'_{vdw}\, dn' \tag{3-34}$$

The stream function due to van der Waals force is obtained using the velocity components $u_r = -v_{vdw}$ and $u_\theta = 0$.

$$-v_{vdw} = \frac{1}{r}\frac{\partial \psi_{vdw}}{\partial \theta} \tag{3-35}$$

$$0 = -\frac{\partial \psi_{vdw}}{\partial r} \tag{3-36}$$

The stream function is determined from Equations (3-35) and (3-36) as:

$$\begin{aligned} \psi_{vdw} &= \int -r\, v_{vdw}\, d\theta + f(r) \\ &= -r v_{vdw}\, \theta + c_0 \end{aligned} \tag{3-37}$$

Since at $r = R_f$, $\psi_{vdw} = 0$, Equation (3-37) becomes:

$$\psi_{vdw} = -r v_{vdw}\, \theta + R_f\, v_{vdw} \big| r = R_f\, \theta \tag{3-38}$$

Van der Waals velocity, v_{vdw} is the product of particle mobility and van der Waals force acting on the particle.

$$v_{vdw} = \beta\, F_{vdw} \tag{3-39}$$

where β is the mobility of the nanoparticles ($\beta = \frac{C_c}{3\pi\mu d_p}$), and F_{vdw} between two bodies with radii of R_f and R_p is given by [156]:

$$F_{vdw} = \frac{A}{6\left[r - \left(R_p + R_f\right)\right]^2}\left(\frac{R_p R_f}{R_p + R_f}\right) \tag{3-40}$$

The particle is assumed as a spherical body and the fiber has a cylindrical shape; however, the fiber is assumed spherical in this analysis with the same curvature in both plains (x and y axis's in Figure 3-1) perpendicular to the flow for several reasons. First, in the process to estimate the rate of collision (Figure 3-1), the deposition is investigated in 2D and is symmetric in the z-direction. Therefore, assuming a cylindrical body for fiber would complicate the model. Second, the fiber is not completely perpendicular to the air flow direction; they might have a curvature in the z-direction and it is not completely cylindrical. As a result, assuming the fiber as a spherical body seems more realistic rather than a flat surface or a cylindrical body. Therefore, Equation (3-40) can be applied to the model, and refinement can be carried out in future studies.

Substituting $\mathrm{v_{vdw}}$ from Equations (3-39) and (3-40) and dimensionless quantities into Equation (3-38), the dimensionless form of stream function due to van der Waals is obtained as:

$$\psi'_{vdw} = \frac{\beta A\theta}{6uR_f}\left(\frac{R_p R_f}{R_p + R_f}\right)\left[\frac{-r'}{\left(r' - \left(\frac{R_p}{R_f} + 1\right)\right)^2} + \left(\frac{R_f}{R_p}\right)^2\right] \tag{3-41}$$

Or

$$\psi'_{vdw} = A_1\theta\left[\frac{-r'}{\left(r' - \left(\frac{R_p}{R_f} + 1\right)\right)^2} + \left(\frac{R_f}{R_p}\right)^2\right] \tag{3-42}$$

where $A_1 = \frac{\beta A}{6uR_f}\left(\frac{R_p R_f}{R_p + R_f}\right)$. Substituting Equation (3-42) into Equation (3-34) gives:

$$N'_{vdw} = \int_0^1 A_1\theta \left[\frac{-r'}{\left(r' - \left(\frac{R_p}{R_f} + 1\right)\right)^2} + \left(\frac{R_f}{R_p}\right)^2 \right] dn' \tag{3-43}$$

Equation (3-43) is transformed to:

$$N'_{vdw} = \int_0^1 A_1\theta \left[\frac{-r'}{\left(r' - \left(\frac{R_p}{R_f} + 1\right)\right)^2} + \left(\frac{R_f}{R_p}\right)^2 \right] \frac{1}{r' \ln(\rho')} dr' \tag{3-44}$$

$$= \frac{A_1\theta}{\ln(\rho')} \left[\frac{R_f}{R_p} + \left(\frac{R_f}{R_p}\right)^2 \ln(\rho') \right]$$

$$= \frac{A_1\theta}{\ln(\rho')} \left(\frac{R_f}{R_p}\right) + A_1\theta \left(\frac{R_f}{R_p}\right)^2$$

where $\frac{1}{\ln(\rho')}$ is obtained by rearranging Equation (3-44):

$$\frac{1}{\ln(\rho')} = \frac{N'_{vdw}}{A_1\theta\left(\frac{R_f}{R_p}\right)} - \left(\frac{R_f}{R_p}\right) \tag{3-45}$$

and Equation (3-15) becomes:

$$-\frac{\partial}{\partial\theta} N'_{vdw} = \frac{D}{u\, R_f} \left[\frac{N'_{vdw}}{A_1\theta\left(\frac{R_f}{R_p}\right)} - \left(\frac{R_f}{R_p}\right) \right] \tag{3-46}$$

Equation (3-46) is an ordinary differential Equation (ODE) in the form of:

$$\frac{\partial N'_{vdw}}{\partial\theta} = -a\, \frac{N'_{vdw}}{\theta} + b \tag{3-47}$$

where *a* and *b* are:

$$a = \frac{D}{u\, R_f A_1 \left(\frac{R_f}{R_p}\right)} \tag{3-48}$$

$$b = \frac{D}{u\, R_p} \tag{3-49}$$

Equation (3-47) is solved by changing variable $\frac{N'_{vdw}}{\theta} = u'(\theta)$. Then the first derivative is:

$$\frac{\partial N'_{vdw}}{\partial \theta} = \frac{\partial u'}{\partial \theta}\ \theta + u' \tag{3-50}$$

With this new variable, Equation (3-47) becomes:

$$\frac{\partial N'_{vdw}}{\partial \theta} = -a\, u' + b \tag{3-51}$$

Combining both Equations (3-50) and (3-51) and rearranging them gives:

$$-\frac{d\theta}{\theta} = \frac{du'}{(a+1)u' - b} \tag{3-52}$$

Equation (3-52) is solved as:

$$-\ln(\theta) + c_0 = \frac{\ln[(a+1)u' - b]}{a+1} \tag{3-53}$$

Thus, by replacing $\frac{N'_{vdw}}{\theta} = u'(\theta)$ in Equation (3-53), the dimensionless rate of nanoparticles moving to fiber surface is calculated as:

$$N'_{vdw} = \frac{\theta\left(c_1 \theta^{-(a+1)} + b\right)}{a+1} \tag{3-54}$$

The dimensionless total rate of nanoparticles colliding on the surface of a single fiber per unit length is:

$$N'_{t-vdw} = 2\int_0^{\pi} \frac{\partial N'_{vdw}}{\partial \theta}\, d\theta = \frac{2\pi\left(c_1\pi^{-(a+1)} + b\right)}{a+1} \tag{3-55}$$

The present model is rearranged as a function of Pe and R:

$$N'_{t-vdw} = \frac{c_1\pi^{\left(-\frac{6k_bT}{A}(R+1)\right)}}{\frac{6k_bT}{A}(R+1)+1} + \frac{2\pi \mathrm{Pe}^{-1}}{\frac{3k_bT}{A}R(R+1)+\frac{R}{2}} \tag{3-56}$$

3.4 Results and discussion

The transport of nanoparticles based on convection and of van der Waals force is validated by the experimental data available in the literature. If nanoparticles adhere to the surface 100%, then the single-fiber efficiency is reduced to transport mechanisms ($\eta_0 = \eta_c$). In the classical filtration models, Pe number is a widely accepted dimensionless parameter to determine single-fiber efficiency due to the diffusion of nanoparticles. According to previous empirical and theoretical models, $\eta_0 \sim \mathrm{Pe}^{-m}$, where $m = -\frac{2}{3}$ [148, 151, 153, 154] or $m = -0.43$ [155]. They are plotted in Figure 3-2a against the experimental data [155, 159-165]. It can be observed that the experimental data do not necessarily scale with a certain power of Pe. In the present model, parameter R (the ratio of particle to fiber sizes) also plays an important role in the diffusion of entities. Figure 3-2b shows the single-fiber efficiency derived from the same experimental data *vs* parameter R. This new presentation reveals that the deposition of entities is separated into three regimes based on R.

Figure 3-3 shows the role of Pe number and the model validation for each regime. When R is small [$R < O(10^{-4})$], the dimensionless rate of collision due to van der Waals dominants the deposition mechanism. As a result, Equation (3-16) is reduced to $\eta_c = C'_d N'_{vdw}$, and the corresponding single-fiber efficiency equals to the non-dimensional particle collision rate: $\eta_0 \propto N'_{t-vdw} \sim \mathrm{Pe}^{-1}$. Figure 3-2a shows that the experimental single-fiber efficiencies of the first regime are parallel to the solid line,

which represents a Pe^{-1} scaling law. The dimensionless rate of particle collision based on van der Waals interaction from Equation (3-56) is validated in Figure 3-3d. For high Pe cases (also high in R), the experimental data deviate from model.

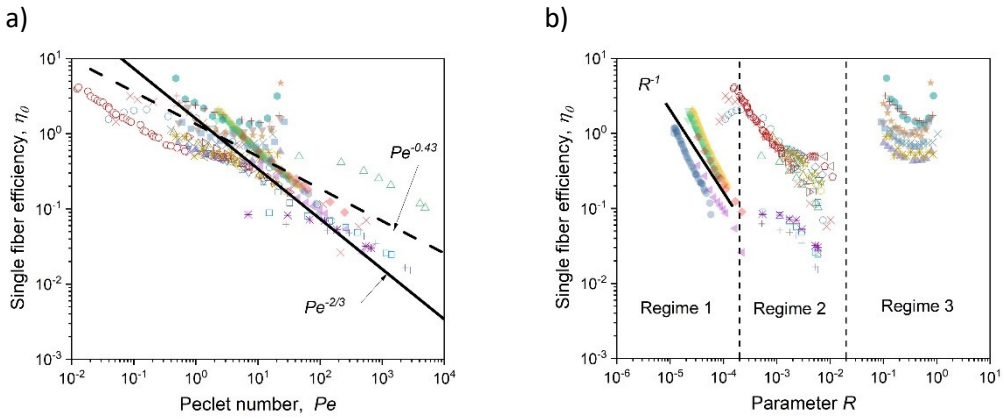

Figure 3-2 The experimental data versus a) Pe, and b) R

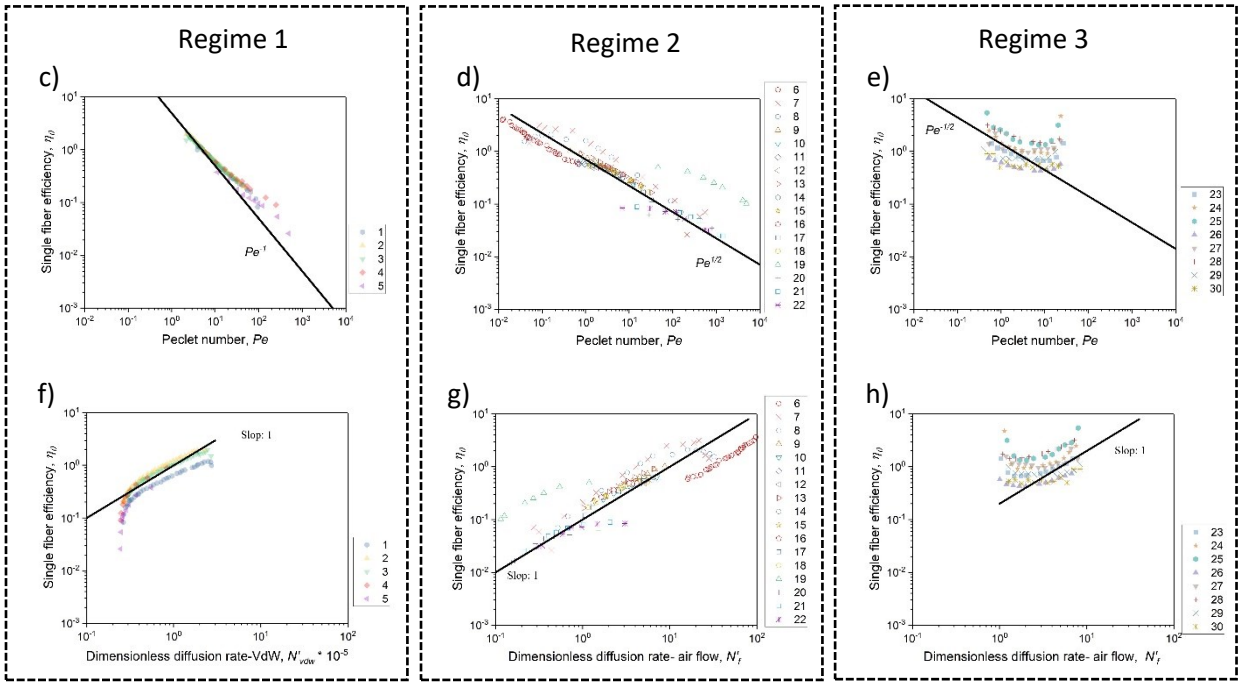

Figure 3-3 The single-fiber efficiency of experimental data versus Pe number in a) regime1, b) regime 2, and c) regime 3, The single-fiber efficiency of experimental data versus diffusion rates in group d) regime1, e) regime 2, and f) regime 3

Figure 3-4 shows the dimensionless rate of collision based on van der Waals as a function of Pe and R. The lines represent the rates for three fiber diameters. For all fiber diameters, the rate is negligible and relatively constant for high R and Pe values (larger particles). The green iso-surface shows the constant value of this rate. With decreasing Pe number and increasing R (Intermediate particles), the rate starts to increase sharply after a specific point (shown by asterisks). All asterisks on the green solid line have the same particle size. There is a critical particle size beyond which the dimensionless rate of collision based on van der Waals becomes negligible. This critical size is unique and depends on the operating parameters and properties. The dimensionless rate of collision based on van der Waals is negligible for the data that deviate from the linear behavior in the first regime. These data are on the boundary of first and second regimes.

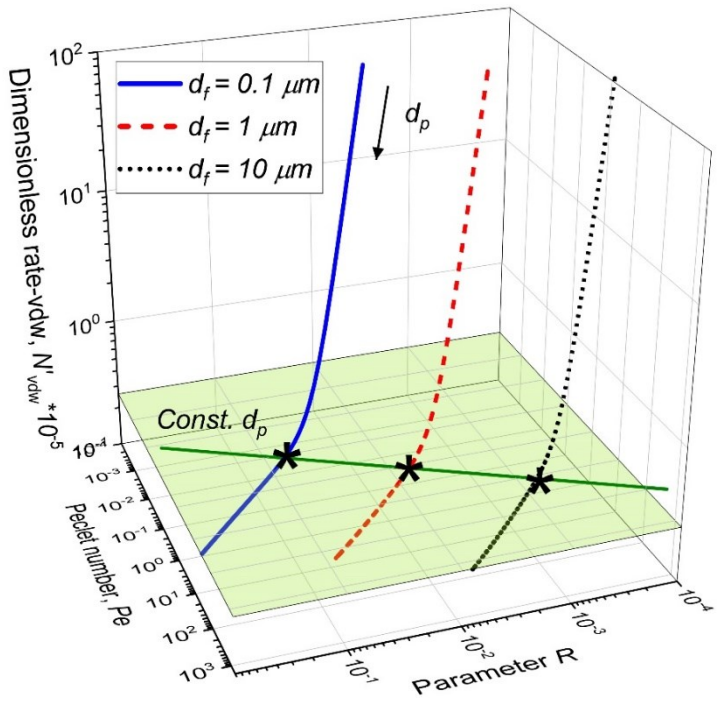

Figure 3-4 The dimensionless rate of collision -vdw versus Pe and R

Table 3-1 Properties and parameters from experimental data

		Particle properties			Filter properties					Operating parameters	
No	**Ref**	**material**	**Hamaker constant (J)**	**Particle diameter (nm)**	**Fiber material**	**Fiber diameter, d_f (m)**	**Filter thickness, L (m)**	**Solidity, α**	**Hamaker conctant (J)**	**u (m/s)**	**T (K)**
1	[159]	WOx	2.12E-19	1.2-6	stainless steel	0.000102	0.000204	0.297	3E-19	0.15	293
2	[159]	WOx	2.12E-19	1.2-6	stainless steel	0.00005	0.0001	0.313	3E-19	0.15	293
3	[159]	WOx	2.12E-19	1.2-6	Nickel	0.000054	0.000108	0.335	4E-19	0.165	293
4	[160]	Silver	3.1E-19	2.9-20	stainless steel	0.00009	0.000203	0.3105	3E-19	0.0493	350
5	[160]	Silver	3.1E-19	2.9-20	stainless steel	0.00009	0.000812	0.3105	3E-19	0.0935	350
6	[161]	NaCl	7E-20	6.2-48	stainless steel	0.00004	0.00008	0.075 assumed	3E-19	4.55E-05	293
7	[162]	NaCl	7E-20	0.9-120	fiber glass	1.18E-05	0.0004	0.0588	8.5E-20	0.025	293
8	[162]	NaCl	7E-20	0.9-67	fiber glass	9.1E-06	0.0004	0.0588	8.5E-20	0.025	293
9	[155]	Silver	3.1E-19	3-20	fiber glass	4.9E-06	0.00074	0.039	8.5E-20	0.053	293
10	[155]	Silver	3.1E-19	4.8-20	fiber glass	3.3E-06	0.00074	0.047	8.5E-20	0.053	293
11	[155]	Silver	3.1E-19	5-20	fiber glass	2.9E-06	0.00069	0.049	8.5E-20	0.053	293
12	[155]	Silver	3.1E-19	9-20	fiber glass	1.9E-06	0.00053	0.05	8.5E-20	0.053	293
13	[155]	Silver	3.1E-19	3-20	fiber glass	4.9E-06	0.00074	0.039	8.5E-20	0.1	293
14	[155]	Silver	3.1E-19	3.9-20	fiber glass	3.3E-06	0.00074	0.047	8.5E-20	0.1	293
15	[155]	Silver	3.1E-19	5-20	fiber glass	2.9E-06	0.00069	0.049	8.5E-20	0.1	293
16	[155]	Silver	3.1E-19	8-21	fiber glass	1.9E-06	0.00053	0.05	8.5E-20	0.1	293
17	[163]	Silver	3.1E-19	4-30	fiber glass	3.3E-06	0.00074	0.047	8.5E-20	0.15	293
18	[163]	Silver	3.1E-19	4-30	fiber glass	2.9E-06	0.00069	0.049	8.5E-20	0.15	293
19	[164]	NaCl	7E-20	8-95	polyester	0.000016	0.00045	0.118	6.5E-20	0.25	298

20	[164]	NaCl	7E-20	8-95	Polyester	0.000016	0.0045	0.118	6.5E-20	0.145125	298
21	[164]	NaCl	7E-20	8-95	polyester	0.000016	0.0045	0.118	6.5E-20	0.072562	298
22	[164]	NaCl	7E-20	8-95	polyester	0.000016	0.0045	0.118	6.5E-20	0.034014	298
23	[165]	WOx	2.12E-19	10-125	PVA	1.83E-07	0.000012	0.0267	3.7E-19	0.069769	293
24	[165]	WOx	2.12E-19	10-125	PVA	1.64E-07	0.000008	0.0303	3.7E-19	0.070028	293
25	[165]	WOx	2.12E-19	10-125	PVA	1.45E-07	0.000006	0.031	3.7E-19	0.070079	293
26	[165]	WOx	2.12E-19	10-125	PVA	1.62E-07	0.00001	0.0153	3.7E-19	0.068961	293
27	[165]	WOx	2.12E-19	10-125	PVA	1.63E-07	0.000014	0.0362	3.7E-19	0.070457	293
28	[165]	WOx	2.12E-19	10-125	PVA	1.52E-07	0.000004	0.0203	3.7E-19	0.069313	293
29	[165]	WOx	2.12E-19	10-125	PVA	1.22E-07	0.000017	0.0245	3.7E-19	0.069612	293
30	[165]	WOx	2.12E-19	10-125	PVA	1.47E-07	0.000029	0.0388	3.7E-19	0.070647	293

By increasing R, to the range of $O(10^{-4}) < R < O(10^{-2})$, the dimensionless rate of collision based on convective diffusion dominants the deposition mechanism, and the corresponding single-fiber efficiency is proportional to the dimensionless particle collision rate: $\eta_0 \propto N'_{t-f} \sim \mathrm{Pe}^{-1/2}$. As shown in Figure 3-3b, experimental data in the second regime is parallel with the solid line, which represents a scaling law of $\mathrm{Pe}^{-1/2}$. The dimensionless rate of collision based on air flow from Equation (3-30) is validated in Figure 3-3e. Deviation from linear behavior for smaller Pe is due to the drop of adhesion probability.

By further increasing R, to $O(10^{-2}) < R$, the interception mechanism becomes important in addition to the diffusion due to the convection. The efficiency due to the interception mechanism is proportional to $\frac{R^2}{1+R}$ [82]. In Figure 3-3c, the experimental single-fiber efficiencies in the third regime are parallel to the solid line, which represents a $\mathrm{Pe}^{-1/2}$ scaling law. The dimensionless rate of particle collision based on convection is validated in Figure 3-3f. For higher values of R, it deviates from linear behavior is likely due to increasing efficiency by the interception mechanism, which is out of the scope of this study because they are mainly for large aerosol particles.

3.5 Conclusions

This chapter presents a model for the transport of nanoparticles from the stream to the fiber surface. This model explains the transport of nanoparticles based on diffusion, considering two flow fields around a fiber. Convective diffusion and interfacial interactive diffusion due to van der Waals force are obtained using boundary layer analysis around a fiber. The dominant mechanism for the transport of nanoparticles depends on Pe and R. When $R < O(10^{-4})$, the dimensionless rate of collision due to van der Waals dominates the deposition mechanism. The dimensionless rate of collision based on van der Waals becomes negligible by increasing the particle size beyond a critical diameter. This critical size depends on the properties of particle and fiber. The collision efficiency based on this mechanism is proportional to Pe^{-1}.

For $O(10^{-4}) < R < O(10^{-2})$, the dimensionless rate of collision based on airflow dominates the deposition mechanism. The collision efficiency based on this rate is proportional to $\mathrm{Pe}^{-1/2}$. For $O(10^{-2}) < R$, interception becomes important in addition to the convective diffusion. The model is validated for nanoparticles by the experimental data in literature.

Chapter 4
Theoretical study on the deposition of intermediate nanoparticle at clean fibers

4.1 Summary

This chapter introduces the deposition model for intermediate nanoparticles on the clean nanofibrous filter. The model is developed considering the interfacial interaction between intermediate nanoparticles with nanofibers. The interfacial interaction with the surface plays a major role in the adhesion and the detachment of intermediate nanoparticles. Adhesion probability is calculated as a function of size and interaction energy bases on the partition function.

4.2 Introduction

Separation of nanoparticles from the air typically falls in the field of air filtration. According to conventional filtration models, the filtration efficiency of intermediate nanoparticles approaches 100% due to high Brownian diffusion rate. However, when the size of the particles approaches intermediate sizes, their deposition on nanofibrous filters is still unclear. Lack of fundamental study of filtration and transition between molecules and nanoparticle behavior are frequently mentioned in several review articles [37-41], no consistent analysis has been proposed yet. Several studies have tried to understand the adhesion of intermediate nanoparticles by considering interfacial interaction when the particles hit a surface. Nonetheless, none of them has been experimentally validated.

Several studies that investigated the deposition of intermediate nanoparticles claim that the transport of particles is not the only dominant mechanism of deposition. After collision, particles might detach from the surface and return to the air flow. For example, Dahneke proposed that particles with intermediate size approaching gas molecules are bound to the surface by molecular attractions, and the probability of detachment based on interaction energies was defined in his model [42]. Hiller and

Loeffler [43] stated that the filtration efficiency of particles of a few nanometers strongly depended on the interaction energy between particles and single fibers. For the first time, they introduced adhesion efficiency to be multiplied by single-fiber efficiency. Wang [44] extend these earlier works and Wang and Kasper [45] developed the thermal rebound model for sub-10 nm particles. According to this model, if the thermal velocity of intermediate nanoparticles surpasses a critical value, they will rebound from the surface. They calculated adhesion efficiency based on the critical velocity. Mouret *et al.* [46] believed that thermal rebound might happen for sub-1 nm particles, based on a more accurate expression for interaction energy. However, the thermal rebound model has not been experimentally validated [82]. On the other hand, quite a few experimental studies stated that thermal rebound could be a reason for efficiency reduction for nanoparticles [166-168]. To investigate the thermal rebound, critical velocity, which is the minimum velocity for rebound occurring, should be addressed properly. The critical velocity can be derived from on initial kinetic energy, acting adhesion force, energy dissipation and deformation modes [45, 169-172], although there is a discrepancy between different models [173].

To understand the deposition of intermediate nanoparticles from the interfacial force point of view, we need to revisit the concept of van der Waals force. The van der Waals force is considered as the main factor in the adhesion of sub-micro systems [47, 48] and the adsorption of molecules on surfaces [49-51]. In physisorption, molecules in the gas-phase are deposited because of the van der Waals force between the molecules and the surface [52-55]. Interfacial interaction should play an important role in the adhesion of intermediate nanoparticles too. Intermediate nanoparticles are expected to inherit similar characteristics as gas molecules because of their size overlap.

Imperfect adhesion has been considered in adsorption models, where only a fraction of striking molecules are adsorbed because of the weakened of interfacial interaction at the small size [54, 56]. For example, Chernyakov proposed that the filtration efficiency of intermediate nanoparticles drops

due to the desorption. In this model, the residence time of particles in the bond state is considered, where the efficiency reduction takes place based on desorption for long times of filter operation [57], although experimental results [58] show a reduction of efficiency even for short times of operation.

This chapter introduces a model for the deposition of intermediate nanoparticles on a clean fiber surface. Adhesion probability is introduced along with the collision based on transport. The adhesion probability is equal to unity for larger particles. However, it is crucial for intermediate nanoparticles and gas molecules to consider imperfect adhesion. Adhesion probability in this model is determined from partition function based on particle-surface interfacial interaction.

4.3 Model Development

As the size of particles becomes intermediate, the imperfect adhesion assumption seems reasonable because of the size similarities between intermediate nanoparticle and gas molecules. With this assumption, only a fraction of intermediate particles that collide on the surface adhere. Thus, the product of collision efficiency η_c and adhesion probability η_{ad} gives the efficiency of a single fiber, η_0,:

$$\eta_0 = \eta_{ad}\eta_c \tag{4-1}$$

Before explaining the hypothesis for the adhesion of intermediate nanoparticles, a definition for their contact with the surface is determined. Although, there is no clear definition for a contact of two surfaces at the molecular level, the definition based on earlier research of Mo *et al*., and Cheng *et al.,* [174, 175] seems reasonable; intermediate nanoparticles are in contact with the surface when the atoms are closer than the separation at the minimum potential energy (r_e). At this separation distance, the intermediate nanoparticle will be at equilibrium, where van der Waals due to the interaction force exerted on the particle is zero ($F_{int} = 0$) [174, 175], although all particles on the surface or in the air stream are under thermal motion and they might depart from the surface when their energy can

overcome this potential energy. Among various adhesion models, which consider particles and surface at contacts such as Hamaker, Hertz, Johnson-Kendall-Roberts (JKR), Derjaguin-Muller-Toporov (DMT), and Maugis-Dugdale (MD) [91, 93, 176-178], the Hamaker model is used to model the particle-surface and particle-particle interactions

Figure 4-1 shows the contact area around the fiber. The discreetness of intermediate nanoparticles, non-additivity, and retardation are ignored in this model [51, 179]. Assuming intermediate particles behave like gas molecules, their adhesion probability can be determined. Similar to the molecules, as an intermediate nanoparticle approaches the surface, the adhesive van der Waals force from the surface exerted on it. The intermediate particles are stabilized at the tiny separation distance, z_0 where the particle is balanced by adhesive and repulsive forces. Intermediate particles are in contact with the surface when it is at a separation distance shorter than z_0, however, larger particles adhere to the surface, while they have physical contact with the surface. One of the main differences between molecules and particles in the term of interfacial interaction is the repulsive force. The pair potential stabilizes molecules on the surface while stabilizing repulsive force for particles comes from their elastic/plastic deformation [51]. Intermediate particles can oscillate in separation distances smaller than z_0 due to the energy exchanges. If the intermediate particle gains enough energy to overcome the energy barrier (equal to maximum adhesive energy), it will dissociate from the surface. For larger particles the adhesive interaction energy is enough for a perfect adhesion, while the smaller sizes the lower adhesive energy is [51], thus detachment of intermediate nanoparticles is more probable than nanoparticles.

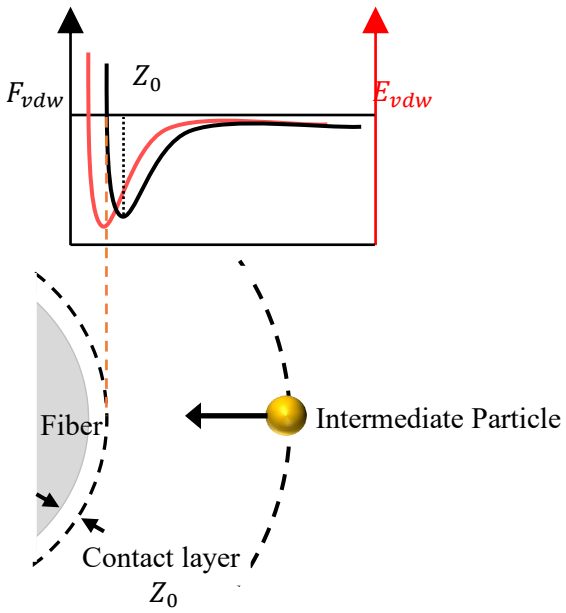

Figure 4-1 the adhesion of entities (intermediate nanoparticles and smaller) to the fiber's surface

Similar to the molecules, the energy of intermediate nanoparticles results from frequent thermal or Brownian motion of surrounding gas molecules, whether these nanoparticles are in the air or on the surface [42]. When they are in the air, this thermal motion leads to diffusion [157], and while they are on the surface the thermal motion may cause them to detach... The adhesion probability is determined base on the adhesive energy to keep the particle on the surface.

The adhesion probability of entities is given as:

$$\eta_{ad} = S_0 f(y) \tag{4-2}$$

where S_0 is the initial adhesion probability and $f(y)$ is the surface coverage function. y is the dimensionless surface coverage. The initial adhesion probability and the surface coverage function can be determined from all possible kinetic processes of adhesion, detaching, and proceeding to the next site. When a molecule striking an empty site, P_a, P_b, and P_c are the probability of adhesion, detaching,

and proceeding to the next site, respectively (Figure 4-2). If the entity strikes on a site that is already contaminated, then P'_a, P'_b and P'_c are used to describe the probabilities of adhesion, detaching, and proceeding to the next site [56]. Thus, the probability of adhesion, bouncing, and moving to the next site on the first site are:

$$P_{a1} = (1 - y)P_a \tag{4-3}$$

$$P_{b1} = (1 - y)P_b + y\,P'_b \tag{4-4}$$

$$P_{c1} = 1 - P_{a1} - P_{b1} \tag{4-5}$$

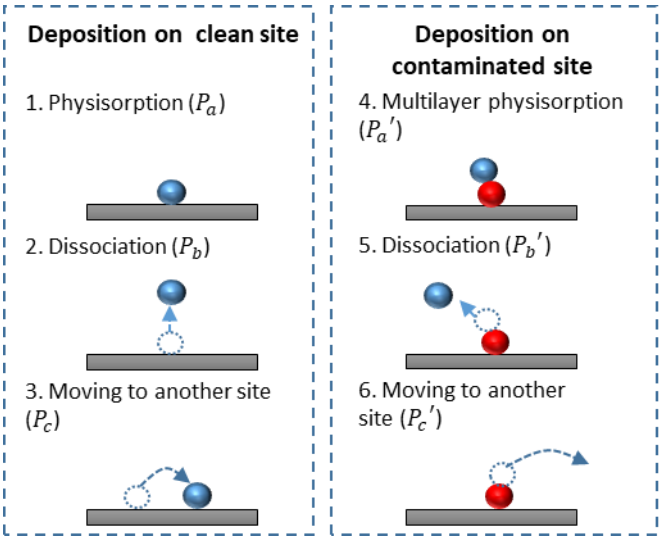

Figure 4-2 Probabilities of adhesion, bounce, and moving to another site for a clean (left) and contaminated site (right). The colliding entities are shown in blue, and already deposited entities are shown in red sphere

With the assumption that the probabilities for the first site are independent with other sites, the probabilities on the second site are:

$$P_{a2} = P_{c1}\big((1-y)P_a\big) \tag{4-6}$$

$$P_{b2} = P_{c1}\big((1-y)P_b + yP'_b\big) \tag{4-7}$$

$$P_{c2} = P_{c1}(1 - P_{a1} - P_{b1}) \tag{4-8}$$

Similarly, the adhesion probability to site *i*, P_i can be calculated as:

$$P_{ai} = (P_{c1})^{i-1}\big((1-y)P_a\big) \tag{4-9}$$

$$P_{bi} = (P_{c1})^{i-1}\big((1-y)P_b + yP'_b\big) \tag{4-10}$$

$$P_{ci} = (P_{c1})^{i-1}(1 - P_{a1} - P_{b1}) \tag{4-11}$$

The total adhesion efficiency is determined by the summation of probabilities of adhesion over all available sites:

$$\begin{aligned}\eta_{ad} &= P_{a1} + P_{a2} + P_{a3} + \cdots \\ &= (1-y)P_a \sum_{i=1}^{n} {P_{c1}}^{(i-1)}\end{aligned} \tag{4-12}$$

The geometric sequence in Equation (4-13) can be replaced by:

$$\big(1 + P_{c1} + {P_{c1}}^2 + \cdots\big) = \frac{1[1 - (P_{c1})^n]}{1 - P_{c1}} \tag{4-13}$$

where $(P_{c1})^n$ can be neglected because n is normally a large number and P_{c1} is a small one. Therefore Equation (4-12) is transformed to:

$$\eta_{ad} = (1-y)P_a \frac{1}{1 - P_{c1}} \tag{4-14}$$

P_{c1} is replaced with Equations (4-3), (4-4), and (4-5) and Equation (4-14) becomes:

$$\eta_{ad} = \frac{(1-y)P_a}{P_a + P_b - y(P_a + P_b - P'_b)} \tag{4-15}$$

When $y = 0$ the initial adhesion probability in Equation (4-2) is given as:

$$S_0 = \frac{P_a}{P_a + P_b} \tag{4-16}$$

With Equation (4-14), the surface coverage function for monolayer deposition is determined as:

$$f(y) = \left(1 + \frac{y}{1-y}\,\frac{S_0 P'_b}{P_a}\right)^{-1} \tag{4-17}$$

The adhesion probability of particles from Equation (4-2) is derived by considering monolayer surface coverage, Equation (4-17); however, real deposition may occur on multiple layers. The surface coverage function based on multilayer assumption is derived in this study. For multilayer deposition, the Kisliuk model can be used with revisions. For multilayer assumption, non-zero P'_a has been considered because entities can be deposited on contaminated sites. Then the probability of adhesion on the first site is defined as:

$$P_{a1} = (1-y)P_a + y\,P'_a \tag{4-18}$$

With the assumption that the probabilities for the first site are independent of the other sites, the probability of adhesion on the second site is:

$$P_{a2} = P_{c1}[(1-y)P_a + y\,P'_a] \tag{4-19}$$

Similar to the derivation of monolayer adhesion probabilities to site *i*, probabilities can be calculated as:

$$P_{ai} = (P_{c1})^{i-1}\left((1-y)P_a + y\,P'_a\right) \tag{4-20}$$

$$P_{bi} = (P_{c1})^{i-1}\left((1-y)P_b + y\,P'_b\right) \tag{4-21}$$

$$P_{ci} = (P_{c1})^{i-1}(1 - P_{a1} - P_{b1}) \tag{4-22}$$

The sum of adhesion probabilities over all available sites gives a new function for the adhesion probability.

$$\eta_{ad} = P_{a1} + P_{a2} + P_{a3} + \cdots = \left((1-y)P_a + y\,P'_a\right)\sum_{i=1}^{n} {P_{c1}}^{(i-1)}$$
$$= \frac{(1-y)P_a + y\,P'_a}{1-P_{c1}} = \frac{P_a + y\,(P'_a - P_a)}{P_a + P_b + \theta\,(P'_a - P_a + P'_b - P_b)} \tag{4-23}$$

Rearranging Equation (4-23) gives:

$$\eta_{ad} = \frac{P_a}{P_a + P_b}\,\frac{1+ny}{1+my} \tag{4-24}$$

where m and n are $n = \frac{P\prime_a}{P_a} - 1$, and $m = \frac{P\prime_a + P\prime_b}{P_a + P_b} - 1$. For zero surface coverage ($y=0$), the adhesion efficiency is reduced to the initial adhesion probability. The probabilities of different states are estimated based on the partition function.

Although a surface coverage function based on multilayer assumption is derived in the preceding analysis, a simple surface coverage function for monolayer is used for further analysis because of the difficulty of estimation on the energies in each state.

The bonding to the surface is due to the interfacial interaction of van der Waals (physisorption). Since physisorbed entities are at thermal equilibrium with respect to the surface [56], the adhesion probability can be determined by considering partition function, which means that after colliding on the surface, they become thermodynamically stable and form a canonical ensemble regardless of adhesion or detachment.

An ensemble is a hypothetical collection of non-interacting systems [180]. Each entity represents a system, and entities in the same state have equal energy and probability. There are six possible kinetic states after collision: adhesion, detaching to the clean site and proceeding from the clean site to the next

site, and adhesion, detaching to an already contaminated site and proceeding from the contaminated site to the next site [56]. The ensemble with its all systems moves towards the state of maximum entropy, and the probabilities of each system in the ensemble can be calculated based on the maximum entropy. The probability of state i out of Ω states is then obtained by the method of the Lagrange multipliers as [180]:

$$P_i = \frac{\exp\left(-E_i/k_b\,T\right)}{\sum_1^{\Omega}\exp\left(-E_j/k_b\,T\right)} \tag{4-25}$$

where i is the state of particle defined in Figure 4-2, and E_i is the energy of a system in state i. By determining the probabilities of six possible kinetic states, the initial adhesion probability and surface coverage function could be determined based on all six states. Entities with equal energy have the same probability. E_i could be E_a, E_b, and E_c, meaning the energy from adhesion, detachment and proceeding to the next clean site respectively. E'_a, E'_b and E'_c, stand for the energy from adhesion, detachment and proceeding to the next contaminated site, respectively. By applying these probabilities, the initial adhesion probability becomes:

$$\begin{aligned} S_0 &= \frac{\dfrac{\exp\left(-E_a/k_b\,T\right)}{\sum_1^{\Omega}\exp\left(-E_j/k_b\,T\right)}}{\dfrac{\exp\left(-E_a/k_b\,T\right)}{\sum_1^{\Omega}\exp\left(-E_j/k_b\,T\right)} + \dfrac{\exp\left(-E_b/k_b\,T\right)}{\sum_1^{\Omega}\exp\left(-E_j/k_b\,T\right)}} \\ &= \frac{1}{\exp\left[-(E_b - E_a)/k_b\,T\right]} \end{aligned} \tag{4-26}$$

and the surface coverage function for monolayer deposition is reduced to:

$$f(y) = \left(1 + \frac{y}{1-y}\,\frac{S_0\,\dfrac{1}{\exp\left[-(E'_b - E_a)/k_b\,T\right]}}{1}\right)^{-1} \tag{4-27}$$

The amount of energy that intermediate nanoparticles needed to overcome barriers and detach from the surface is equal to interaction potential. The interaction potential between bodies due to the van der Waals force is the energy of adsorption, or the difference between energies of the entities in the adsorbed, and the gas state [181]. Therefore, the difference between E_a and E_b is particle-surface interfacial interaction and the difference between ${E'}_b$ and ${E'}_a$ is particle-particle interfacial interaction due to van der Waals force. Since the energy barrier for detachment of intermediate nanoparticle in multilayer deposition (E_{pp}) is lower than that in monolayer (E_{sp}), the adhesion probability in the contaminated site is lower than a clean site. By assuming that the energy of deposited particle is the same in monolayer and multilayer deposition, ${E'}_a = E_a$, the Equations (4-26) and (4-27) are determined bases on E_{pp} and E_{sp}.

The energies E_{pp} and E_{sp} are estimated with the assumption of the purely attractive interaction potential between two atoms or molecules in the air at a separation z_0, $E_{int}(r) = -C/r^n$. As discussed in Section 3.3.2, the particle is assumed as a spherical body and the fiber is assumed spherical in both plains (x and y axes in Figure 3-1). The interaction potential between two macroscopic bodies will be the sum of the interaction energy between all molecules in the first body and all molecules in the second body:

$$E_{int} = -\frac{A}{6}\left\{\frac{2R_1R_2}{(2R_1+2R_2+z_0)z_0} + \frac{2R_1R_2}{(2R_1+z_0)(2R_2+z_0)} + \ln\frac{(2R_1+2R_2+z_0)z_0}{(2R_1+z_0)(2R_2+z_0)}\right\} \quad (4\text{-}28)$$

where R_1 and R_2 are the radii of the bodies of concern, z_0 is their minimum separation distance, and A is effective Hamaker constant for the bodies 1 and 2 ($A = \sqrt{A_1A_2}$).

4.4 Results and Discussion

4.4.1 Adhesion probability of intermediate nanoparticles

Figure 4-3 compares the model with the experimental data for two cases in literature [166] (Figure 4-3 a, and 4-5 b), where NaCl nanoparticles are deposited on a glass fibrous filters. The properties of these two cases are listed in Table 3-1. The experimental data are shown in scattered markers. As explained in Chapter 3, the dominant mechanism of transport for theses cases is convective diffusion. Therefore $C_d N'_f$ is a dominant term in Equation (3-16). The solid lines show the model considering two correction factors in Equation (3-16). The solid red line for $C_d = 1/(1 + N'_f)$ from [153], and solid blue line for $C_d = 0.2$ determined by the results from the previous chapter.

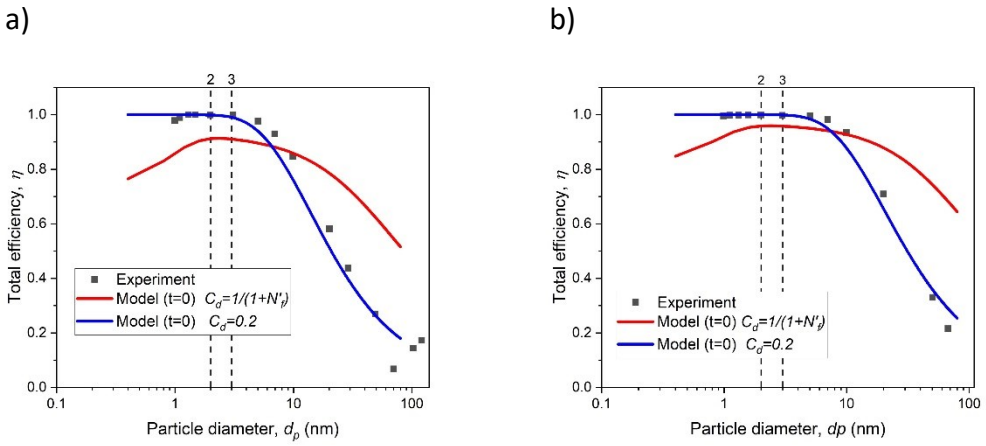

Figure 4-3 Comparison between model and experiment [166] a) Case 7, and b) Case 8

Figure 4-3 a, and 4-5 b, shows that, the model with $C_d = 0.2$ (blue line) is consistent with the experimental data for particles larger than 3nm. However, no efficiency drop is shown with the blue line. By considering $C_d = 0.2$, however, the collision efficiency for sub-3 nm is higher than unity, and the total efficiency is considered as 100 %.

The vertical dashed line at 3 nm shows the onset of efficiency drop due to the lower adhesion probability. The model shows that single-fiber efficiency increases with decreasing particle size due to the diffusion mechanism; however, the single-fiber efficiency begins to drop when the particle size is 3 nm or smaller. Since initial adhesion probability is lower than unity for sub-3 nanoparticle, the adhesion of NaCl particles on the glass fibrous fibers is no longer 100%. Depending on the properties of the filter, the total filtration efficiency may also decrease for sub-3 nm particles.

The model with $C_d = 1/(1 + N'_f)$ shows efficiency drops for sub-2 nm nanoparticles, which is consistent with the experiment. For sub 3 nm nanoparticles, the model and the experimental data follow the same trend, although the experimental data has a 10 % vertical shift in Figure 4-3 a and 6% in Figure 4-3 b. It can be concluded that for intermediate particles, a correction factor of $C_d = 1/(1 + N'_f)$ should be considered, otherwise the correction factor is 0.2.

Figure 4-4 and Figure 4-5 show eight sets of experimental data reported in literature [155] and two more cases from [160], all of which are compared to the model. The properties of the cases are listed in Table 3-1. Silver nanoparticles are deposited on the glass fibrous filters (Figure 4-4), and the stainless steel wire screen (Figure 4-5). Measured total efficiency is shown with scattered markers. As explained in Chapter 3, the dominant mechanism of transport for theses cases is convective diffusion. Thus, $C_d N'_f$ is dominant term in Equation (3-16). The solid lines show the model results with different correction factors. The results are depicted in solid red line for $C_d = 1/(1 + N'_f)$ [153], and solid blue line for $C_d = 0.2$ determined by the results from Chapter 3.

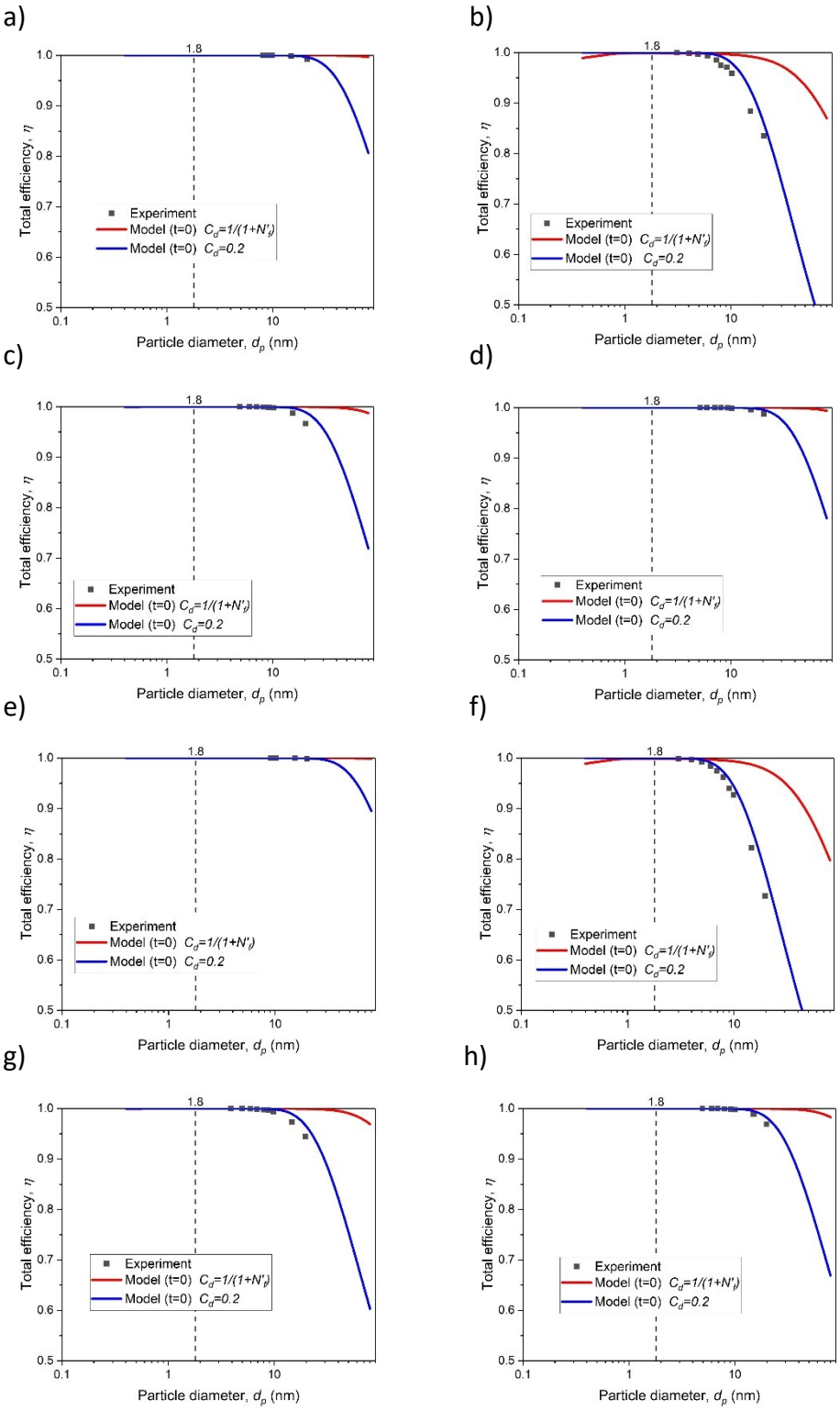

Figure 4-4 Model results compared to experiments [155] a) to h) Cases 9 to 16

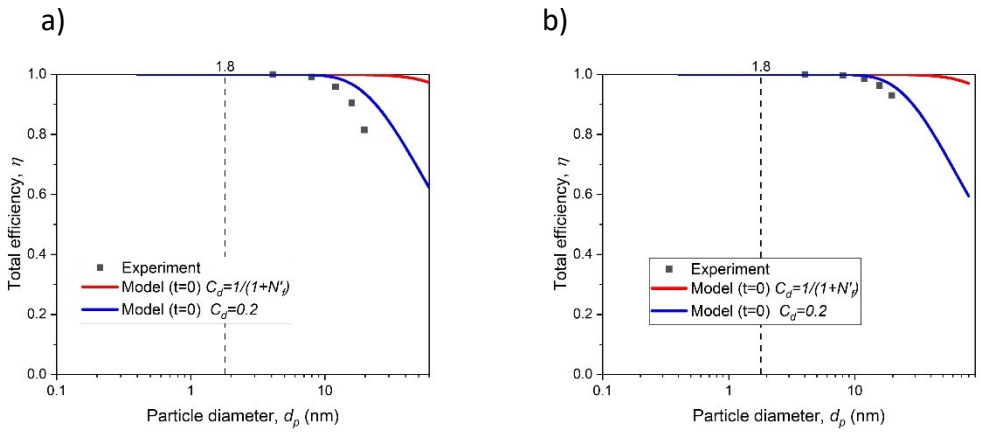

Figure 4-5 Model results compared to experiments [160] a) Case 17, and b) Case 18

As indicated by the vertical dashed lines, the initial adhesion probability is lower than unity for sub-1.8 nanoparticles. Although the single-fiber efficiency is expected to drop for this range, the model shows no efficiency drop with respect to the filter properties. For particles larger than 1.8 nm, the model using $C_d = 0.2$ (blue line) agrees well with the experimental data in Figure 4-4 and Figure 4-5. For sub-1.8 nm particles, the model using $C_d = 1/(1 + N'_f)$ shows no efficiency drops, which is consistent with the experiment.

Figure 4-6 compares the model to 3 experiments in terms of total efficiency [159]. As explained in Chapter 3, the dominant mechanism of transport for these cases is diffusion due to the van der Waals force, thus $C'_d N'_{vdw}$ is a dominant term. Tungsten oxide nanoparticles are deposited on stainless steel wire screens (Figure 4-6a, and b) and nickel (Figure 4-6c). Measured total efficiency is shown with scattered markers. The solid lines show the model results considering different correction factors in Equation (3-16). The results are depicted using solid red lines for $C'_d = 1/(1 + N'_{vdw})$ [153], and solid blue line for $C'_d = 10^{-5}$ determined by the results from Chapter 3.

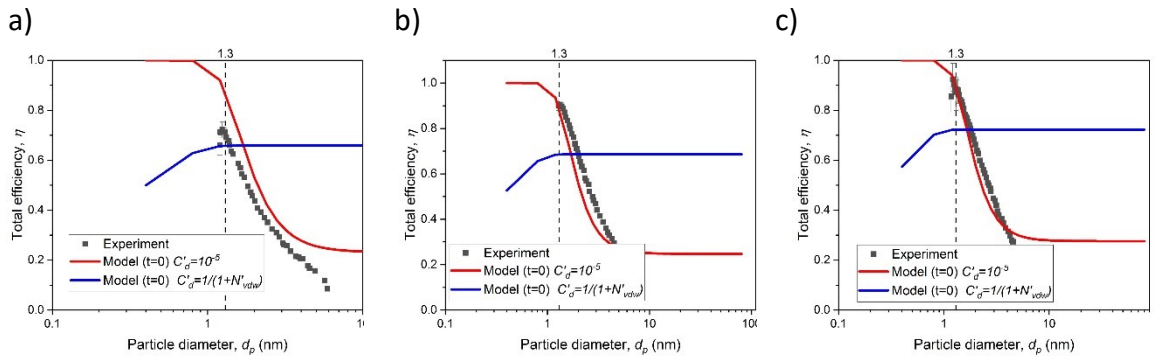

Figure 4-6 Model compared to experiment [159] a) Case 1, b) Case 2, and c) Case 3

The experimental data show a slight efficiency drop starting from 1.3 nm. The model with $C_d = 0.2$ (blue line) agreed with the experimental data when the particles are larger than 1.8 nm in diameter. For sub-1.8 nm particles, the model with $C_d = 1/(1 + N'_f)$ shows no efficiency drop, which is consistent with the experiment. The initial adhesion probability from the model is lower than unity for sub-1.3 nm nanoparticle interacting with stainless steel and sub-1.4 nm nanoparticle interacting with nickel, however, with respect to the filter properties, the model (blue line) shows the efficiency drop starting from 1.3 nm nanoparticle in all cases.

4.4.2 Effects of particle size on initial adhesion probability

Figure 4-7a shows single-fiber efficiency and its components, collision efficiency, and initial adhesion probability. The single-fiber efficiency is the product of the collision efficiency and the adhesion probability. The particles are WOx nanoparticles (0.4-100 nm) and the fibers are PVA nanofibrous fiber ($d_f = 187\ nm$). The collision efficiency due to the diffusion of particles is decreased with particle size, but it increases due to interception mechanism. A combination of both mechanisms shows collision efficiency. For intermediate nanoparticles, collision efficiency reaches 100 %. As shown in Figure 4-7a,

the drop in initial adhesion probability is observed for sub-1 nm nanoparticles for given operating conditions. Thus, the single-fiber efficiency also decreases in this size range.

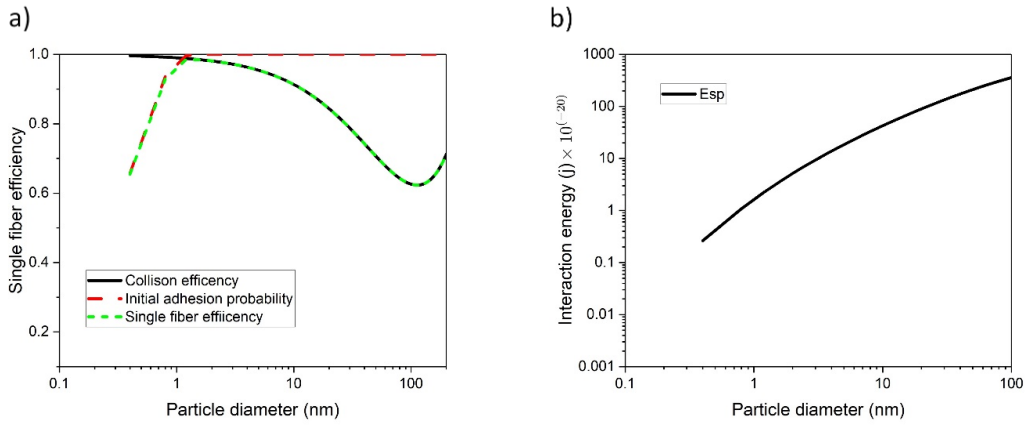

Figure 4-7 a) Components of single-fiber efficiency, b) adhesive interaction energy due to van der Waals force between nanoparticles and fiber (d_f = 187 nm)

According to the present model, the adhesion of intermediate particles is not 100%. With clean fibers (zero time), the adhesion probability (=initial adhesion probability) drops as the particle size decreases. At time zero, when the fibers are almost clean, the particle-surface interaction energy determines adhesion probability, which is size dependant. The intermediate nanoparticle have continues drop in the adhesive interaction energy binding particles to the fiber surface (Figure 4-7b), while the average energy of particles is constant, which is about $k_b\,T$. Thus, the probability of their detachment from the surface is higher for intermediate nanoparticles compared to the nanoparticles. The drop in adhesion probability leads to lower values of efficiency for the intermediate size range. For larger nanoparticle sizes, adhesion probability approaches 1. Therefore, only diffusion in the boundary layer contributes to the filtration. The model reduces to the conventional filtration model, where single-fiber efficiency is due to the diffusion and interception.

4.4.3 Effects of material properties on initial adhesion probability

Figure 4-8 shows the effects of Hamaker constant on initial adhesion probability of 1, 2, and 3 nm particles. The effective Hamaker constant is calculated using the Hamaker constants of the fiber and the particles. As seen in Figure 4-8, the adhesion probability is less than unity for low values of Hamaker constants. Higher values of Hamaker constant lead to higher particle-surface interaction energy and stronger bonding to the surface. Thus, the reduction of efficiency in the intermediate size range is expected for some materials. The Hamaker constants of some materials are listed in Table 4-1. For example, metal nanoparticles or fibers have higher Hamaker constants than the other materials, thus adhesion of those materials is expected to have greater probabilities.

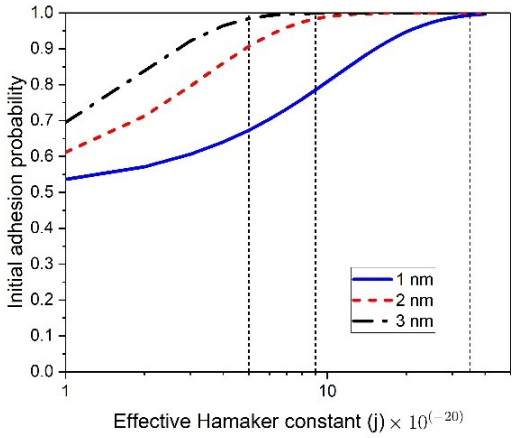

Figure 4-8 Initial adhesion probability versus effective Hamaker constant for 1, 2, and 3 nm particles on fiber surface

The critical effective Hamaker constant also varies with size. The adhesion probability of 3 nm particles with an effective Hamaker constant of less than 5×10^{-20} J is less than unity, while adhesion probability of 1 nm particles with an effective Hamaker constant less than 35×10^{-20} J is lower than unity. For this reason, larger particles are more probable to adhere to the surface.

Table 4-1 Values of the Hamaker constant for various materials

Material	Hamaker constant in air (10^{-20} J)
Metals (Au, Ag, Cu)	20-50 [51]
Silicon (Si)	19-21[51]
Polymers	0.3-37 [182]
Fiberglass	8.5 [51]
NaCl	7
Silica (SiO2)	6.5 [51]
Carbon	5-25 [182]

4.5 Conclusions

A model is introduced in the chapter for the deposition of intermediate nanoparticles on nanofibers. As the size of nanoparticles decreases to intermediate size, the adhesion probability drops below unity. In this model, the interfacial interaction plays a major role in the adhesion and detachment of intermediate nanoparticles. These particles could overcome the energy barrier because of the interfacial interaction of intermediate nanoparticles and surface. The adhesion probability of intermediate nanoparticles is determined based on the partition function. The adhesion probability magnifies as the size of particles decreases to the molecular scale. The adhesion probability in this model could be less than unity for a range of intermediate sizes, depending on the properties. Thus, materials should also be considered to improve the filtration efficiency of intermediate particles.

Chapter 5
The kinetic behavior of entities in the deposition process

5.1 Summary

In this chapter, the model from the previous chapter is expanded with consideration of surface coverage.

This chapter introduces a kinetic model for the deposition of entities from molecular to nano sizes. The adhesion probability from the previous chapter is improved by considering surface coverage, which is a key factor for the deposition of molecules and intermediate nanoparticles, but it does not affect the deposition of larger nanoparticles. Concentration and time can have an interchangeable role on surface coverage and the deposition of entities. With high particle concentrations, the filter surface is covered with more particles. In addition to concentration, time is another factor that causes more coverage. Therefore, the effects of both initial concentration and time on the interfacial interaction are considered in surface coverage.

In addition, this model is validated using experimental data for gas adsorption and filtration of intermediate particles. To determine the reliability of experimental data, the role of an instrument on the uncertainty of measurement for the filtration of sub-2nm nanoparticles is also investigated prior to using the data for model validation. The error of filtration efficiency associated with the limit of detection (LOD) of the system due to the noise level is characterized and compared for different dilution ratios.

5.2 Introduction

In addition to the size dependency of interfacial interaction, which is explained in Chapter 4, time and initial concentration may also be influential to the deposition of intermediate particles on nanofibers. In kinetic adsorption, both time and initial concentration are key parameters on the deposition on the adsorbate. The percentage adsorption (efficiency) is decreased at higher initial concentrations of

molecule in the kinetics process of adsorption, although the uptake capacity of adsorption is increased [104, 105, 107, 183]. The effects of time and concentration are demonstrated by breakthrough curves in adsorption kinetic models. The breakthrough curves show the ratio of downstream to upstream concentration versus time for different concentrations. At higher concentrations, the breakthrough behavior takes place faster and the ratio of downstream concentration to the upstream concentration (or penetration) is higher during the time of operation [122]. The breakthrough behavior is predicted by kinetic adsorption models.

In kinetic adsorption models, mass transfer includes 3 steps: Step 1, external diffusion, Step 2, pore diffusion [IPD], and Step 3, surface reaction. The last step is the attachment of adsorbate to the adsorbent. However, the second step does not exist for the adsorption on the surface of activated carbon fibers, since the surface of activated carbon fibers is clear and smooth [135]. Reactions do not take place in physisorption without chemical bond. Therefore, assuming a diffusion control rate is a reasonable assumption for intermediate nanoparticles.

In adsorption kinetics, the deposition efficiency drops as the fiber surface is gradually covered with entities. Concentration and time can have an interchangeable role on surface coverage. At higher concentrations, the filter surface is covered with more particles than low number concentrations. In addition to concentration, time is another factor that affects surface coverage. With more surface coverage, the adhesion probability and efficiency are reduced. Surface coverage can be a dimensionless parameter for breakthrough behavior, and a single breakthrough curve that describes all data should be established.

In air filtration studies, the concentration dependency of efficiency has been reported [36, 58, 59]. However, their findings are contrary to conventional filtration theories, which claim that concentration and operation time do not affect the filtration efficiency of nanoparticles. Therefore, the roles of both

initial concentration and time (i.e., kinetic behavior) on the interfacial interaction should be considered and an analytical model is needed to predict this behavior.

This chapter presents a model for intermediate nanoparticles and smaller sizes with consideration of surface coverage. Surface coverage is introduced as a dimensionless parameter expressing the effects of time and initial concentration on the deposition of entities on fibers. A kinetic model is developed for the deposition of a wide range of entities from molecular to nano sizes, where for nanoparticles the surface coverage function is reduced to unity. This model is validated using experimental data of adsorption and filtration of intermediate particles. Furthermore, the reliability of experiments in the intermediate size range is discussed.

5.2.1 Measurement of filtration efficiencies for sub-3 nm particles

Measuring aerosol size distributions down to 2 nm is a major challenge in many studies related to the nucleation and particle growth, aerosol filtration and environmental protection [184-188]. Since 1970, differential mobility analyzers (DMAs) have been used for sizing particles larger than 5 nm [189]. Sizing down to clusters (~1 nm) is possible with the recent improvement of DMAs [190, 191]. Despite developments and improvement of instruments, the measurement by current electrical mobility spectrometers contains large uncertainties for sub-2 nm particles. The uncertainties could be due to the particle losses, diffusional broadening effect, low particle counting statistics, chemical composition dependency, and unknown charging probabilities [192].

Recent advances tried to overcome these uncertainties by core sampling optimizing sheath flow rate [193-197]. The performance of instruments was evaluated and improved based on overall detection efficiency and size resolution. However, Cai *et al*. believed that aerosol flow rate and measurement time should be considered. In their study, a parameter π was proposed. π parameter and size resolution are used to evaluate the performance of instruments [198].

The experimental data from [58] are used to validate the present model. The scanning mobility particle sizer coupled with a Faraday cup electrometer (SMPS+E, GRIMM Model 5.706) was used to measure nanoparticle size distributions before and after filtration. Regarding uncertainties that instruments might have in measuring the concentration of sub-2nm particles, whether the data is still reliable for the application of aerosol filtration has not been discussed before. If the uncertainties are amplified for low particle concentrations, the concentrations of upstream and downstream filter should vary and the accuracy of filtration measurement might be undermined. Therefore, the error of filtration efficiency associated with the LOD of the SMPS+E due to noise is characterized.

5.3 Method

5.3.1 Model for kinetic adhesion of entities to a single fiber

According to Equation (4-2), in addition to the interfacial interaction, surface coverage also affects the surface coverage function and adhesion probability. The surface coverage is estimated from the kinetic deposition process.

Adsorption kinetics can be modeled as a diffusion control process based on the linear film diffusion model (LDM) [106]. LDM is a lumped kinetic model to describe the kinetic process of adsorption based on mass balance:

$$\frac{dq}{dt} = k\,(q_e - q) \tag{5-1}$$

where q and q_e are the mass concentration and maximum-possible mass concentration at the surface, respectively. k is the overall effective mass transfer coefficient. There is no rigorous calculation available for this coefficient. The LDF mass transfer coefficient has been calculated from experimental breakthrough fronts [199]. The correlation between mass transfer coefficient to the effective diffusion coefficient depends on the geometry of adsorbent [199, 200]. Thus in this research, the constant rate is

the rate of particles deposited at the surface, which is represented by the single-fiber efficiency by deposition on a clean site ($\eta_{0(t=0)}$) times the residence time of deposition ($\tau = \frac{d_f}{u}$). Since the adsorption kinetic models are used for the entire filter, k is also scaled with the ratio of dimensionless bet specific surface area of the filter ($\frac{A_{bet}}{A_f}$), where A_{bet} is the specific surface area and A_f is the surface of filter perpendicular to the flow. Therefore, k is calculated as:

$$k = b\frac{A_f}{A_{bet}} \cdot \frac{\eta_{0(t=0)} u}{d_f} \tag{5-2}$$

Integrating Equation (5-1) for boundary conditions $t = 0$ to t and $q = 0$ to q gives:

$$q = q_e\left(1 - e^{-kt}\right) \tag{5-3}$$

The surface coverage, y is obtained by the correlation between the mass concentration and surface coverage. As shown in Figure 5-1a, at $t = 0$, the number of particles with the size d_p, that is deposited on the single fiber is $(n_0)^{2/3}\eta_{0(t=0)}$. Thus, the mass concentration at the surface is determined at $t = 0$ by multiplying number concentration and mass of particles with the size d_p:

$$q_{(t=0,d_p)} = \frac{\pi\left(d_p\right)^3}{6}\rho_p\,(n_0)^{\frac{2}{3}}\eta_{0(t=0)} \tag{5-4}$$

As shown in Figure 5-1b, $(n_0)^{\frac{2}{3}}\eta_{0(t)}$ (in the unit of #/cm^2) particles will be added to the fiber over time, t, and total mass concentration on the fiber at time t is:

$$q_{(d_p)} = \int_0^t \frac{\pi\left(d_p\right)^3}{6}\rho_p\,(n_0)^{\frac{2}{3}}\eta_{0(t)}\,dt \tag{5-5}$$

$$= \frac{\pi\left(d_p\right)^3}{6}\rho_p\,(n_0)^{\frac{2}{3}}\int_0^t \eta_{0(t)}\,dt$$

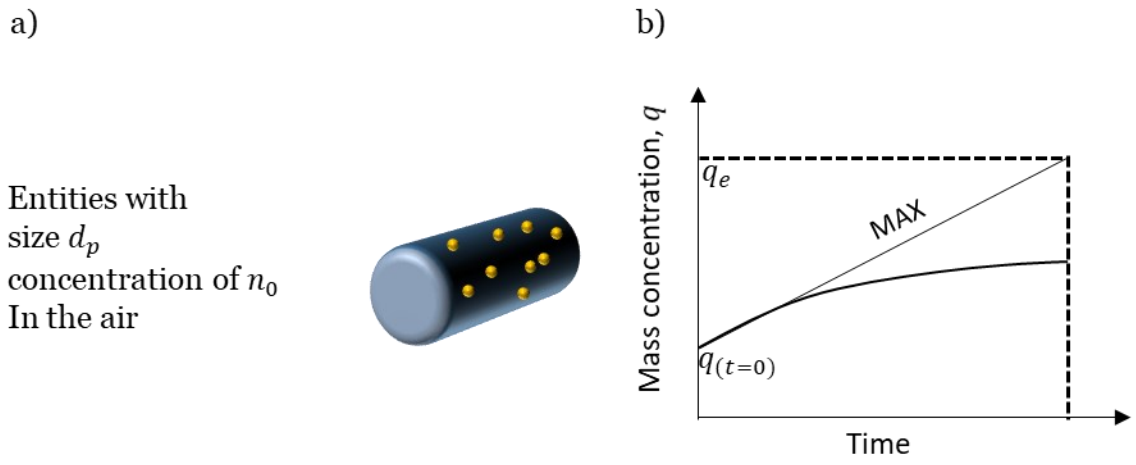

Figure 5-1 a) Mass concentration (or surface coverage) of particles deposited on a single fiber at time zero, b) mass concentration of particles on the surface over time

As the deposition during the time is reduced due to the lower efficiency, $\eta_{0(t)}$, the maximum deposition takes place at time $t = 0$. Therefore, maximum mass concentration is assumed to be proportional to the deposition at $t = 0$ (Figure 5-1b):

$$q_{e\,(d_p)} = b\frac{\pi(d_p)^3}{6}\rho_p\,(n_0)^{\frac{2}{3}}\eta_{0(t=0)} \tag{5-6}$$

where b is constant. By assuming monolayer deposition, all particles with the size d_p are deposited on the surface of fiber. Similarly, calculation, the surface coverage is estimated as:

$$y_{d_p} = \int_0^t \frac{\pi(d_p)^2}{4}\,(n_0)^{\frac{2}{3}}\eta_{0(t)}\,dt \tag{5-7}$$

$$= \frac{\pi(d_p)^2}{4}\,(n_0)^{\frac{2}{3}}\int_0^t \eta_{0(t)}\,dt$$

Substituting Equations (5-5), (5-6) and (5-7) into Equation (5-3) gives:

$$y_{d_p} = b\, n_0^{\frac{2}{3}} \eta_{0(t=0)} \pi \left(d_p\right)^2 \left(1 - e^{-kt}\right) \tag{5-8}$$

Regarding the size dependency of $\eta_{0(t=0)}$ as well as concentration distribution in the poly-disperse case, the total surfaces coverage, y, is obtained by integrating Equation (5-8) over the size range 0 to $+\infty$:

$$y = \int_0^{+\infty} y_{t,d_p}\, d\left(d_p\right) = b \left(\int_0^{+\infty} {n_0}^{2/3} \eta_{0(t=0)} \pi \left(d_p\right)^2 \, \mathrm{d}d_p \right) \left(1 - e^{-kt}\right) \tag{5-9}$$

5.3.2 Evaluation of experimental data for the filtration of intermediate nanoparticles

The systematic error related to the experimental data from literature is determined from the LOD of measuring devices for sub-4nm particles. The concentration of particles from [58] is measured by SMPS+E. In comparison with CPCs, FCEs have higher counting efficiency due to the high diffusional loss for very intermediate nanoparticles. Furthermore, FCEs are not sensitive to operating conditions, particle composition, or charge state [18, 201-203]. However, FCEs have a high background noise level. The noise level is described by the root mean square (RMS) of signal. The limit of detection of FCE is different from CPC; it can be estimated based on the root mean square (RMS) value of the noise level based on the average over the measurement time:

$$LOD = \frac{3 \cdot \ln 10 \cdot RMS_1}{\pi_{FCE}} \tag{5-10}$$

Coefficient 3 is due to possible background count interference of one or two raw counts. The RMS based on the average over the measurement time is determined by the RMS based on 1 s average.

$$RMS_t = \frac{RMS_1}{\sqrt{t/1s}} \tag{5-11}$$

The parameter π_{FCE} in (5-10) is defined as a product of overall detection efficiency, the root of measurement time, the aerosol to sheath flow ratio, and the effective aerosol flow rate [198]:

$$\pi_{FCE} = eP\sqrt{t/1s}\, Q\, \beta \left(-\frac{d \log d_p}{d \log Z_p}\right) \tag{5-12}$$

where e is the unit of charge, $Z_p$is the particle electrical mobility, β is the aerosol to sheath flow ratio and Q is the effective aerosol flow rate. The overall detection efficiency is usually determined by the product of efficiencies through the instrument given as:

$$P = \eta_{samp}\eta_{char}\eta_{DMA}f_c\eta_e \tag{5-13}$$

where f_c is the charge fraction of particles, which is determined based on the Fuchs theory[204]. Based on this charge distribution, particles smaller than 13 nm accept a single charge. η_{samp}, η_{char}, η_{DMA} , and η_e are penetration efficiencies through the sampling line, charger, DMA, and electrometer. The product of theses three efficiencies is called penetration efficiency:

$$\eta_{pen} = \eta_{samp}\eta_{char}\eta_{DMA} \tag{5-14}$$

The particle loss through different parts of the instrument is estimated based on the effective length approach [191]. The penetration efficiency is given by:

$$\eta_{pen} = 0.819\exp(-3.66\mu) + 0.0975\exp(-22.3\mu) + 0.0325\exp(-57.0\mu) + 0.0154\exp(-107.6\mu) \quad for\ \mu > 0.02 \tag{5-15}$$

$$\eta_{pen} = 1 - 2.56\,\mu^{\frac{2}{3}} + 1.2\,\mu + 0.1767\mu^{\frac{4}{3}} \quad for\ \mu \leq 0.02$$

where D is the diffusion coefficient of particles, Q is the flow rate through the cylindrical DMA, L_{eff} is the effective length, and μ is the dimensionless deposition parameter:

$$\mu = \frac{\pi\, D\, L_{eff}}{Q} \tag{5-16}$$

5.4 Results and Discussion

5.4.1 Validation of the model for surface coverage

The adhesion probability drops below unity when the size of nanoparticles decreases to intermediate size. The adhesion probability depends on size, time, and concentration. The surface coverage function describes the related kinetic behavior of deposition. Since the measured efficiency depends only on surface coverage (*i.e.*, time and concentration), the surface coverage function, Equation (4-17), is compared with the transformed surface coverage:

$$f_{exp}(y) = \frac{\eta_{exp}}{\eta_c S_0 \frac{4\alpha L}{\pi d_f (1-\alpha)}} \tag{5-17}$$

Figure 5-2 compares the model [Equation (4-17)] with the surface coverage function transformed from experimental data [104, 205] using Equation (5-17). The properties and operating conditions of experimental results from the literature are listed in Table 5-1. These experimental data are from physisorption of gas (toluene) molecules on nanofibers. The surface coverage of the experimental data, x-axis, is calculated using the time and concentration and other parameters reported in the references for a single size entity. See Equation (5-8), where $a = 1$, $b = 0.25$, and the size of toluene is assumed 6.7 $\dot{A}$. The nanofiber properties were used to correlate the data for a single fiber. In adsorption, specific surface area (A_{bet}) is one of the key adsorbent properties for kinetic behavior [104], while in air filtration α, L, and d_f are commonly reported filter properties. Thus, $\frac{4\alpha L}{\pi d_f(1-\alpha)} = \frac{A_{bet} m}{\pi A_f (1-\alpha)}$ is used in the correlation between single fiber and total efficiency, where m is the mass of filter, and A_f is the filter surface perpendicular to the flow. Since the new coefficient is a large number, normalized $f_{exp}(y)$ is shown in Figure 5-2. The solid line shows the model result for $f(y) = \left(1 + \frac{y}{1-y}\, PR\right)^{-1}$.

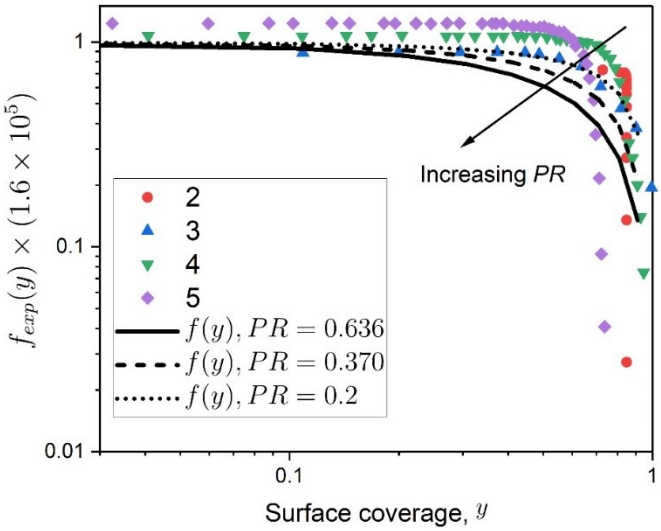

Figure 5-2 Surface coverage function for the experimental data and model

Table 5-1 Properties and parameters of molecule experimental data

		Entity properties			Filter properties							Operating parameter	
No	**Ref**	**Entity material**	**Hamaker constant (J)**	**Concentration (ppm)**	**Fiber material**	**Hamaker constant (J)**	**Fiber diameter, d_f**	**Solidity, α**	**Specific surface area, A_{bet} (m^2/g)**	**Weight, m (g)**	**Filter surface area, A_f (m^2)**	**Flow rate (LPM)**	**Temperature, T**
1	[104]	VOC (toluene)	5.4E-20	2000	Carbon	2.17E-19	4.6E-07	0.2 assumed	1000	5	π×0.028×0.1	0.5	323
2	[104]	VOC (toluene)	5.4E-20	2000	Carbon	2.17E-19	4.6E-07	0.2 assumed	1500	5	π ×0.028×0.1	0.0010	323
3	[205]	VOC (toluene)	5.4E-20	50000	Carbon	2.17E-19	10–20 μm	0.32	700–2500	6.2	π×0.02×0.3	0.5	318
4	[205]	VOC (toluene)	5.4E-20	8750	Carbon	2.17E-19	10–20 μm	0.32	700–2500	6.2	π×0.02×0.3	0.5	318
5	[205]	VOC (toluene)	5.4E-20	4000	Carbon	2.17E-19	10–20 μm	0.32	700–2500	6.2	π×0.02×0.3	0.5	318

Since the new coefficient is a very large number, the normalized $f_{exp}(y)$ is shown in Figure 5-2. The solid line shows the model result for $f(y) = \left(1 + \frac{y}{1-y}\, PR\right)^{-1}$, where $PR = \frac{S_0\, P\prime_b}{P_a}$ is the probability ratio. PR is not experimentally available, but by comparing the experiment and model, PR is estimated as 0.636 for monolayer deposition. The dashed line shows the model, with lower values of $PR = 0.370$. Admittedly, neither of them is accurate, and it deserves further investigation in future studies. Nonetheless, both model and experimental data show that the surface coverage function, $f(y)$, which is proportional to the adhesion probability, drops with decreasing surface coverage. The surface coverage gradient of the experimental data is low ($y = 0\ to\ 0.5$) for low surface coverages. At a high surface coverage, however, the gradient drops sharply ($y = 0.5\ to\ 1$).

Several factors may contribute to the discrepancy between $f_{exp}(y)$ and $f(y)$. First, the model assumes monolayer deposition, but actual deposition may occur on multiple layers. Although a surface coverage function based on multilayer assumption is derived in this study, a simple surface coverage function for monolayer is employed for simple estimation on the energies in each state. Further research on the surface coverage function is needed for a more robust adhesion probability. Second, the energy difference between adhesion and detached states are estimated by interfacial interaction, rather than the exact energy of each state. Additionally, for simplicity, Hamaker model is used for interfacial energies to calculate the probability of different states; a better estimation of interfacial interaction should improve the present model accuracy. Third, the discrepancy may also be attributed to the properties of filter media which in some cases, a range was reported instead of a single value for the filter properties. More experimental data with more filter properties are needed for the validation of the model.

5.4.2 Validation of the model for intermediate nanoparticle

Figure 5-3 compares the measured efficiencies [58] with the calculations for intermediate nanoparticles in the size range of 0.8-3.3 nm (*i.e.*, $\mathrm{Pe} = 0.003 - 0.05$). The dashed line is for time zero and the solid line, at 10 min. The operation time is not reported in the literature. Constants $a = 9 \times 10^{-8}$ and $b =$

1.6×10^8 are used for all six cases. The scattered markers are for the experimental data. The calculated error bars for experimental data are due to the systematic error associate with the LOD of the system due to the noise level. As error bars show, the result for those particles that have a higher concentration (in the middle of size distribution diagram) are more reliable; the error bars due to the LOD are smaller for 1-1.4 nm particles. All show that lower concentrations result in higher filtration efficiencies.

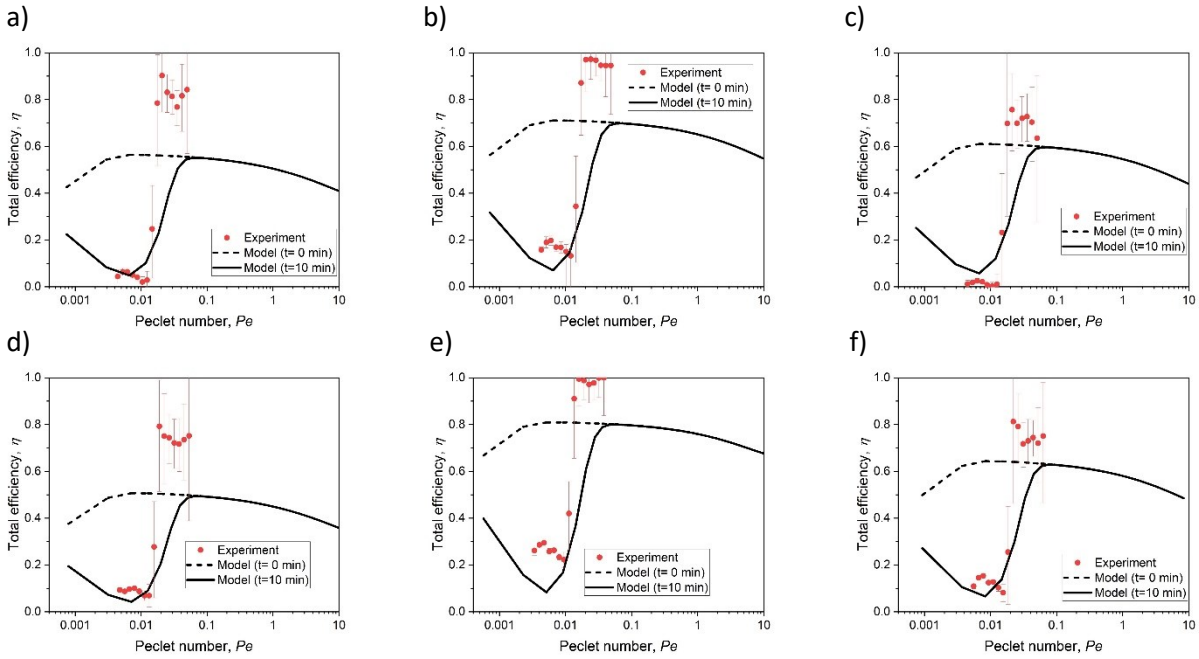

Figure 5-3 Model and experimental filtration efficiencies for WOx nanoparticles using PVA nanofibrous filters (a-f) 1-6 cases

The model results at time zero show that the filtration efficiency is reduced for intermediate sizes range, which is due to lower initial adhesion probability; however, a greater reduction is observed in experimental data. The experimental data shows that the total efficiencies of intermediate nanoparticles drop for Pe numbers smaller than 0.02 (*i.e.*, sub-2 nm particles). The present model enlightens this behavior, considering the effects of surface coverage.

Over time, more particles are covering the fiber surface, which worsens the total efficiency. Although the time of operation is not reported by the authors of this paper, by assuming that the data acquisition was performed in a short period (~10 min), the model results at $t=10$ min are consistent with the experiments in all six cases. Thus, at a relatively higher surface coverage (after 10 min), the efficiency drop is initially steeper following by a minor increase at low Pe number. This minor increase at a very low Pe number is likely because of the lower surface coverage of smaller particle sizes. Finally, the length of the filters used in experiment is measured using a digital micrometer by pressing the filter mat, thus the numbers are considered with a 30% error. By considering error more even than 30 %, much better fitting can be provided.

Regardless of the discrepancy between model and experiment, it can be concluded that the effects of concentration on the deposition of intermediate nanoparticles become more and more obvious over time. This behavior might not be observed for concentrations than these 6 cases since surface coverage is less important for a low concentration and a short time.

In comparison with the deposition of molecules, the surface of the fiber is covered by intermediate nanoparticles much faster due to the larger size of intermediate nanoparticles than molecules. Thus, the surface-converge dependency of deposition takes place faster than the deposition of molecules. A better estimation of energies in different states can increase the accuracy of the model.

Table 5-2 Properties and parameters of intermediate nanoparticles experimental data

		Particle properties			Filter properties						Operating parameter	
	Ref	**Particle material**	**Hamaker constant (J)**	**Particle size, d_p**	**Fiber material**	**Fiber diameter, d_f (m)**	**Filter thickness, L (m)**	**Solidity, α**	**Hamaker constant (J)**	**Filter diameter (m)**	**Face velocity, u (m/s)**	**Temperature, T (K)**
1	[58]	WOx	2.12E-19	0.8-3.3	PVA	1.87E-07	8.4E-06	0.0157	3.7E-19	0.025	0.137978	293
2	[58]	WOx	2.12E-19	0.8-3.3	PVA	1.82E-07	11.2E-06	0.0171	3.7E-19	0.025	0.138175	293
3	[58]	WOx	2.12E-19	0.8-3.3	PVA	1.91E-07	1.54E-05	0.009	3.7E-19	0.025	0.137184	293
4	[58]	WOx	2.12E-19	0.8-3.3	PVA	2.01E-07	8.4E-06	0.0144	3.7E-19	0.025	0.137796	293
5	[58]	WOx	2.12E-19	0.8-3.3	PVA	1.43E-07	7E-06	0.0283	3.7E-19	0.025	0.138344	293
6	[58]	WOx	2.12E-19	0.8-3.3	PVA	2.36E-07	1.54E-05	0.0107	3.7E-19	0.025	0.137323	293

5.5 Conclusions

In this chapter, the model from the previous chapter is expanded with consideration of surface coverage. The dimensionless parameter of surface coverage to consider the effect of both initial concentration and time provides a better understanding of the kinetics of adhesion in breakthrough behavior of adsorption area as well as the deposition efficiency of intermediate nanoparticles. According to the model, the effect of the concentration of the deposition of intermediate nanoparticles becomes important over time. This behavior might not be observed for low concentrations since surface coverage is not considered in lower concentrations after a short time.

The model is validated by the experimental data of molecules and intermediate nanoparticles. In comparison with the deposition of molecules, the surface of the fiber is covered by intermediate nanoparticles much faster due to the larger size of intermediate nanoparticles. Thus, the surface-converge dependency of deposition takes place faster than the deposition of molecules. Better estimation of the energies in different states results in better fitting to the experiments.

Chapter 6
Comprehensive theory for deposition of entities from molecular to nano-sizes on nanofibers

6.1 Summary

In this chapter, all the models in Chapter 3 through 5 are integrated into one piece as a comprehensive model for a wide size range of entities from molecular to intermediate nanoparticles, and regular nanoparticles. The deposition behavior of all entities is explained with respect to their transport, adhesion, interfacial interaction, and surface coverage dependency. In this model, the entities are transported by diffusion to filter surface. Adhesion probability is determined based on the particle-surface interfacial interaction, time, and initial concentration of entities.

6.2 Comprehensive deposition model

Figure **6-1** illustrates the comprehensive model framework. The total filtration efficiency is determined by correlating of single fiber with filter media (upper left). This correlation is based on mass balance so that it can be used for entities of various sizes. The principle of this model is based on steady transport of entities to the single fiber surface (top-right) followed by a kinetic process of adhesion (bottom). Both convective diffusion and interfacial interactive diffusion owing to van der Waals force are obtained using boundary layer analysis around a single fiber. After particles collide on the fiber surface, they may adhere to it and the adhesion probability is determined based on the particle-surface interfacial interaction, time, and initial concentration of entities.

The following assumptions are made in developing the comprehensive model. Isothermal condition is considered for this model and temperature is assumed to be uniform throughout the filter. The fiber surface is homogenous with equal surface energy in different sites. Interaction between entities is

neglected. The model for the steady transport of entities to the fiber and kinetic process of their adhesion are explained as follows.

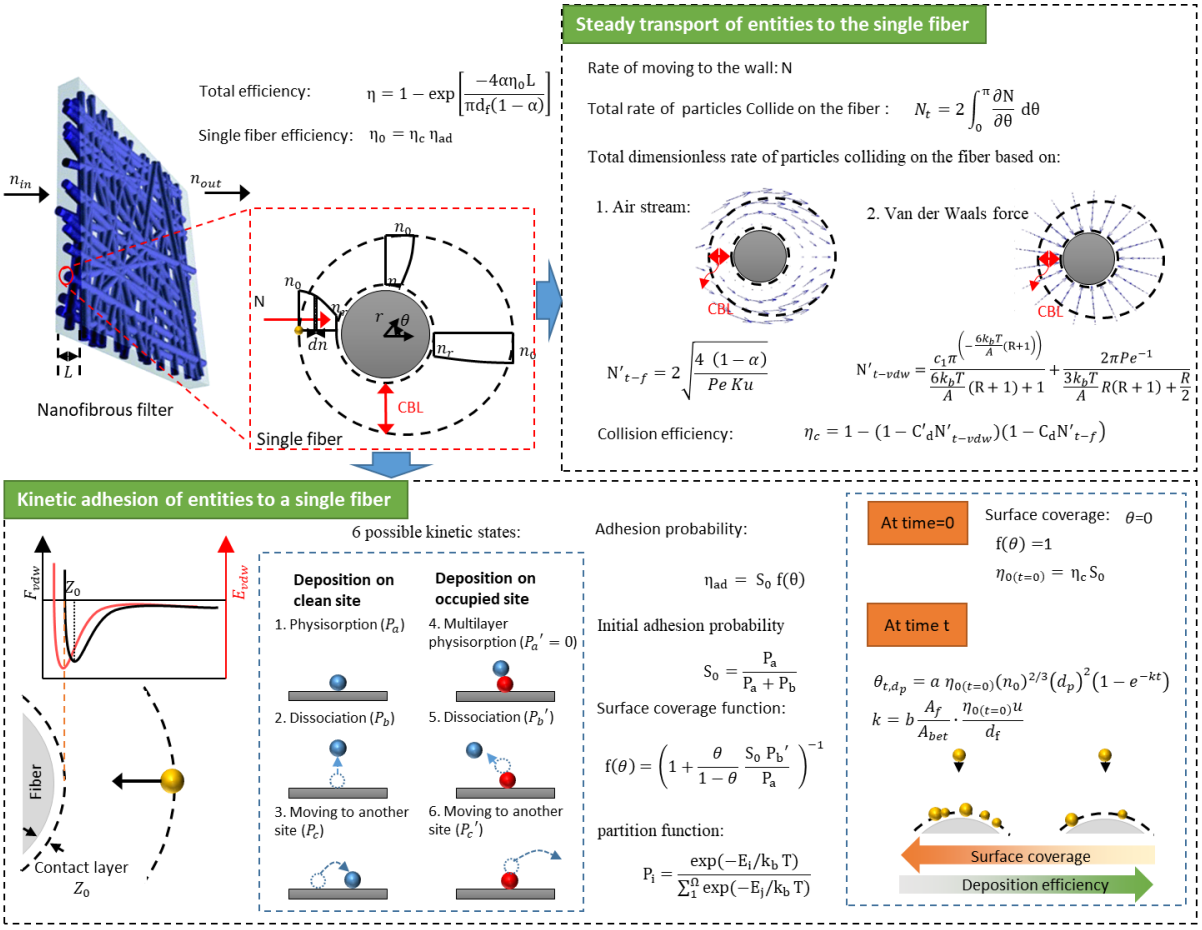

Figure 6-1 Model development based on steady transport of entities and kinetic adhesion

Figure 6-2 elaborates on the comprehensive model for the deposition of entities on a nanofiber and their comparison with the filtration and adsorption experimental data. Figure 6-2b presents total efficiency as a function of entity size and time for two concentration distributions; high initial concentration is shown with a solid black line and low initial concentration is shown with a dash red line. Low concentration stands for a case where the total number concentration is $\sim 10^7\,(\mathrm{cm}^{-3})$ and the value for high concentration is approximately 10 times higher than the low concentration. These results

are obtained for WOx entities with the size range varying from 0.4 to 110 nm and PVA nanofiber filter at 25°c and 13.6 cm/s face velocity. The filters have a mean fiber diameter of 191 μm, thickness of 50 μm, and the solidity of 0.01. The model is reduced to adsorption (Figure 6-2a) when the size of entities approaches molecular size; on the other hand, it is consistent with the conventional filtration models for larger nanoparticles (Figure 6-2c) where the filtration of nanoparticles does not vary with the time (Figure 6-2b). The model results are explained in the following from different perspectives.

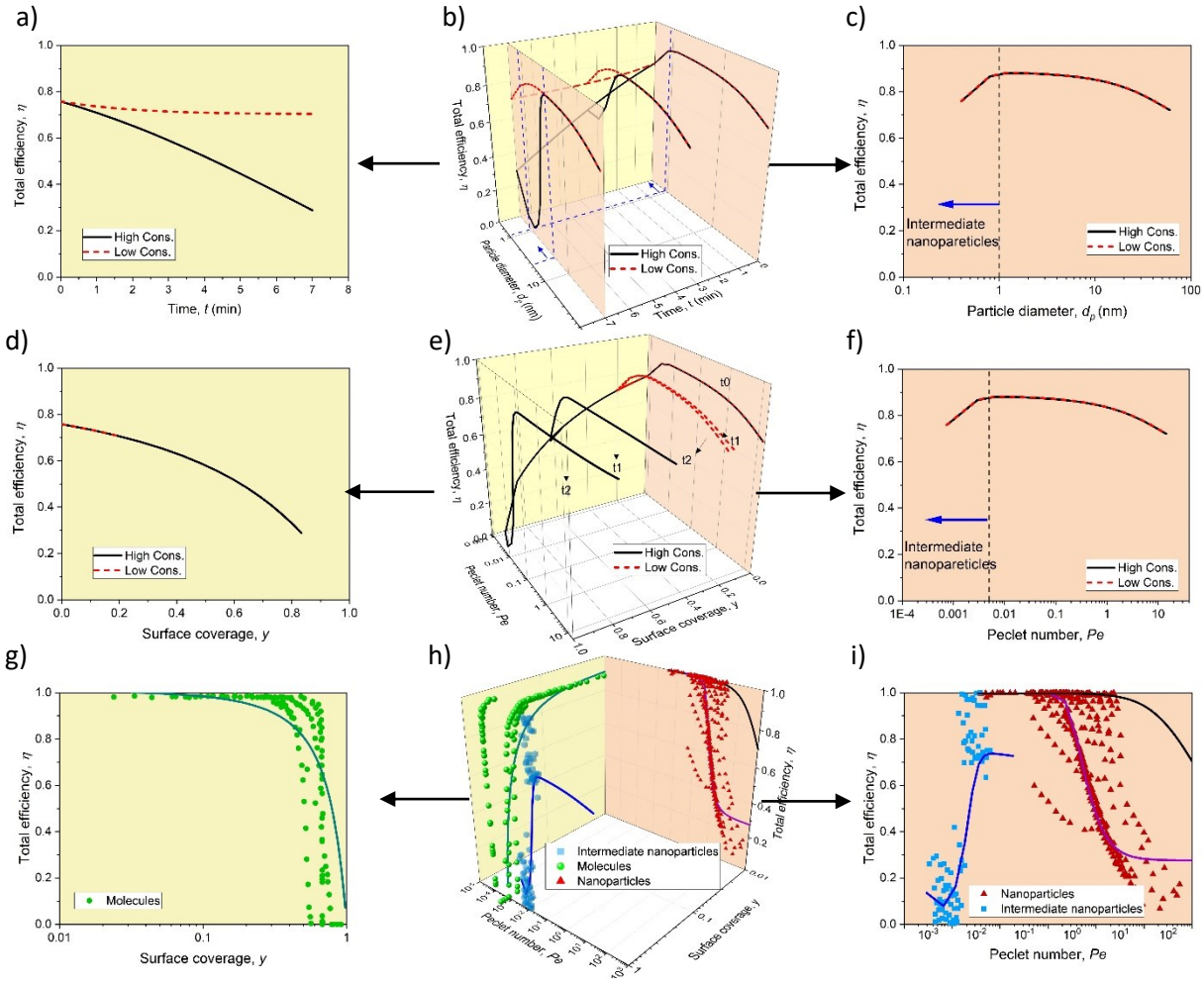

Figure 6-2 The comprehensive model and its validation with experimental data, the total efficiency of the model (a-c) as a function of particle size and time, (d-f) as a function of Peclet number and surface coverage, and the total efficiency of experimental data (g-i) as a function of Peclet number and surface coverage

6.2.1 On the molecular perspective

For molecules, the model shows that the total efficiency is time and concentration dependent. It can predict the breakthrough behavior in adsorption kinetics. Figure 6-2.a shows the efficiency of $d_p = 0.4\,nm$ at the high initial concentration (solid black line) and the low initial concentration (dash red line). Molecules in this size are deposited on the surface based on physisorption. The efficiency drops over time since more entities covered the fiber surface. Since the adhesion probability of deposition on a contaminated site is lower than the clean site on a fiber, efficiency drops at a high surface coverage.

Besides the effects of time, the initial concentration also affects surface coverage and efficiency. The efficiencies are lower for a higher initial concentration because of relatively higher surface coverage. These results are consistent with the breakthrough curves in adsorption kinetics. The breakthrough takes place faster at a higher concentration and the ratio of downstream concentration to the upstream concentration (or penetration) is lower than the values for low concentrations during the time of operation [122].

Figure 6-2d shows the total efficiency as a function of surface coverage by considering both time and concentration. The effects of surface coverage are negligible for the low concentration. The total efficiency of all five cases of adsorption data from literature is shown in Figure 6-2g as a function of surface coverage. Figure 6-2g shows the measured total adsorption efficiency as a function of their calculated surface coverage, which is discussed in Chapter 5. All these prove that the comprehensive model is applicable to adsorption.

6.2.2 On the nano-sized perspective

Figure 6-2c shows that the comprehensive model concurs the conventional filtration theories, where diffusion is the dominant mechanism of nanoparticle filtration. In the present model, the diffusion of particles to the fiber's surface could be determined based on the airflow or van der Waals interaction.

For a clean surface, a reduction in efficiency is observed while the particle size approaches molecular size. The drop in efficiency is observed for entities with sub-1 nm entities, for the given operating parameters. The main reason for this behavior is the particle-surface interfacial interaction. As the size of nanoparticles drops to the intermediate size range, the adhesive interaction energy binding particles to the fiber surface continuously drops, while the average energy of particles remains constant, about k_b T. Thus, the intermediate nanoparticles can overcome the energy barrier and detach from the surface more easily than larger particles. The adhesion probability of intermediate nanoparticles to the surface is lower compared to the nanoparticles and the drop in adhesion probability leads to lower efficiency for the intermediate size range. For larger particle sizes, adhesion probability approaches to unity, and diffusion determines the filtration, which does not vary with time or concentration. The efficiency of nanoparticles shown in Figure 6-2c is stable, whereas Figure 6-2b reveals the efficiency drop over time for intermediate nanoparticles.

The efficiency drop in the intermediate size range depends on the properties of particles and nanofibers. However, the efficiency of intermediate nanoparticles might not drop when particles and fibers have great Hamaker constants, which increase adhesion probability for particles. In this model, The Hamaker model is used for adhesive interaction energy between bodies, which has simplified. Discreetness of intermediate nanoparticles, non-additivity, and retardation are ignored in this model [51, 179]. A more accurate definition for the interaction of intermediate nanoparticles with a surface should be developed in the future to improve this model.

Figure 6-2d demonstrates the total efficiency as a function of the Peclet number. The collision efficiency of nanoparticles based on either airflow (black line) or van der Waals interaction (purple line) is a function of Pe number. Figure 6-2i shows experimental results for total filtration efficiency

as a function of the Pe number. According to the model, data are discussed and categorized based on the dominant transport mechanism in Chapter 3.

6.2.3 On the intermediate-size perspective

The present model shows that the deposition of intermediate nanoparticles not only depends on size but also time and concentration. Figure 6-2c shows that, at time zero, the total efficiency of intermediate nanoparticles drops since the adhesion probability is lower than unity in this size range. When the fibers are almost clean, the particle-surface interaction energy determines adhesion probability, which depends only on particle size. At time zero, number concentration does not affect the filtration performance; however, over time, the role of concentration on the deposition process of intermediate nanoparticles becomes important.

Figure 6-2b depicts the total efficiency of intermediate nanoparticles as a function of particle size, time, and concentration. At time zero, both efficiencies for low concentration (dashed red line) and high concentration (solid black line) are entangled. As time goes on, the effect of concentration on the deposition becomes important. With more surface coverage provided by high concentration, adhesion probability and subsequent total efficiency drops further than in low concentration.

Similar to the adhesion of molecules, the adhesion probability of intermediate nanoparticles is lower when they collide on a contaminated site than that on a clean surface. Thus, the more surface coverage, the lower adhesion probability for the transient nanoparticles. This phenomenon is adopted in the comprehensive model: adhesion probability is determined by interfacial interaction energy, which is the barrier for detachment. Since the particle-particle interaction energy due to the van der is lower than particle surface interaction energy, the adhesion probability of deposition on a contaminated site is lower than the deposition on a clean site. Moreover, if a particle collides on a contaminated site, the separation between the collided particle and surface increases, therefore the adhesive interaction energy

decreases with the power of 6 ($E_{int} = -C/r^6$) and the surface is unable to keep the particle. All in all, it can be concluded that, regardless of monolayer or multilayer deposition, the adhesion probability and total efficiency of deposition decrease with increased surface coverage. Nevertheless, this thesis reports the work based on monolayer deposition for simplicity.

Figure 6-2e shows the total efficiency calculated for the deposition of entities on nanofiber in terms of Pe and surface coverage. The deposition of intermediate nanoparticles depends on both Pe and surface coverage. With zero surface coverage, the efficiency decreases with size. At a relatively higher surface coverage, however, the efficiency first drops steeply then slightly increases at a very low Pe. The reason for this minor increase at low Pe number is the reduced surface coverage for smaller particles. Finally, Figure 6-2h summarizes all the measured total efficiencies for nanoparticles, intermediate nanoparticles, and molecules as a function of Pe and surface coverage. Overall, they agree with the model. Note that these experimental data are also analyzed in Chapter 5.

6.3 Conclusions

In this chapter, the models in previous chapters are integrated into a comprehensive model for the deposition of entities from molecular to nano sizes on the nanofibers. The comprehensive model is reduced to the adsorption where the size of entities approaches the molecular size and for larger nanoparticles, it reduced to the conventional filtration, since the filtration of nanoparticles does not vary with the time. The deposition behavior of entities from nano, molecular, and intermediate size perspectives are studied and well understood.

Chapter 7
Conclusions and future work

7.1 Conclusions and contributions

A new theoretical interpretation of deposition of entities has been established in this thesis work. A comprehensive model is developed for the deposition of entities from a few Angstroms to tens of nanometers on a fiber. The principle of this model is the quasi-steady deposition of entities and kinetic adhesion. The transport of entities is determined based on convective diffusion and interfacial interactive diffusion. As the size of entities decreases to intermediate range, which is between gas molecules and nanoparticles, adhesion probability on the surface is less than unity. Adhesion probability is determined based on the interfacial interactions and kinetic process of adhesion. Smaller particles need a lower amount of energy to overcome the energy barrier based on the interfacial interaction of intermediate nanoparticles and surface, results in their detachment from the surface. Moreover, the contaminated surface may interfere with the adhesion process. The developed dimensionless parameter of surface coverage provides a better understanding of adhesion kinetic by considering the effects of initial concentration and time. The model is validated by experimental data in the literature.

7.2 Recommendations for future research

This section discusses potential areas of research that would extend the work initiated in this thesis.

7.2.1 Extending model considering reaction (Chemisorption)

The present model in this thesis can be extended by considering surface chemical reactions. It could provide a better understanding of the reaction-control adsorption since the physical meanings of the current kinetic models have not been well established [206]. Such a model could be used to predict the performance of media in the separation of gases as well as intermediate particles. This extended model

considering chemisorption is deemed important to the kinetic adsorption. Moreover, the filtration efficiency of intermediate nanoparticles could be enhanced by chemical reaction.

Multiple factors should be taken into consideration in developing the model based on chemical reactions. First, the difference of energies in adhesion and detachment states is equal to the activation energy of desorption. The activation energy could be calculated using the Arrhenius equation [207]. Then, the adhesion probability can be calculated. Second, the rate of reaction should be considered in the variation of surface coverage over time. Third, since chemisorption is an exothermic process, the isotherm assumption is no longer valid and the temperature of surface changes during deposition. In this case, the effects of thermophoresis should be considered. Accordingly, the molecular collision from the hot side of particles pushes them to the cold side because of a temperature gradient [158]. This phenomenon affects the transport of entities due to the modified stream around the fiber. The thermophoretic force strongly depends on the Knudsen number in the free molecular regime[158].

7.2.2 Extended model considering size-dependant material properties

Nanoparticles exhibit unique properties both physically and chemically because of their distinctive surface structure. Their mechanical, electronic, optical, electrical, and even thermal behavior is very much different from that of bulk materials [37, 61, 65, 66]. Dielectric permittivity, as a function of frequency, is used to calculate the Hamaker constant of material from Lifshitz theory. Deriving Hamaker constant for macroscopic bodies from Lifshitz theory agreed well with experiments [51]. However, it deviates for intermediate nanoparticles. For metal nanoparticles, Hamaker constant varies with size due to the scattering of free conducting electrons and size dependency of the dielectric permittivity [131-134]. Improved model considering size dependant properties of particles may give more accurate results than the one using bulk properties.

7.2.3 Enhancing the removal efficiency of intermediate nanoparticles with modified fiber structure

The present model offers some suggestions to enhance the deposition efficiency of intermediate nanoparticles. Interfacial interaction plays a key role in the transport and adhesion process, enhancing the interaction and efficiency. Adhesive interfacial interaction is increased in several ways. First, the selection of filter material with a greater Hamaker constant is one solution. This effect has been observed in experimental studies in the literature. For example, polar polymer nanofibers such as polyacrylonitrile (PAN) provides a higher filtration efficiency of $PM_{2.5}$ than nonpolar polypropylene fibers [208]. The polarity affects dielectric polarization and Hamaker constant, which is a separation of electric charge that causes electric dipole moment. Second, fiber roughness may alter adhesion, depending on asperities size and surface properties [209]. Thus, fiber surface modification by coating particles or fabrication processes may enhance the adhesive interaction of particles and a surface.

Moreover, the available surface area on the filter is also influential in the deposition of intermediate nanoparticles and molecules. Nano-scaled rough structures on the surface increase the effective surface area [210].

7.2.4 Model improvement for surface coverage function

Several improvements are suggested for the surface coverage function in the present model. First, the assumption of a multilayer may provide a more realistic estimation of deposition, although monolayer deposition is used for simplicity in the current model. The surface coverage function based on multilayer assumption is derived in this study but not used because of the difficulty of estimation of the energies in each state. Further research on the surface coverage function is needed to provide a more robust surface function. Second, a better estimation of the energies in each state may provide a better assumption for surface coverage function. In the present study, the energy difference between adhesion

and detached states are estimated by interfacial interaction, rather than exact values for the energy of each state. Moreover, the Hamaker model is used for interfacial energies to calculate the probability of different states for simplicity, while better estimation on the interfacial interaction can improve the present model.

Bibliography

1. Fiore, A.M., et al., *Global air quality and climate.* Chemical Society Reviews, 2012. **41**(19): p. 6663-6683.
2. Huang, R.-J., et al., *High secondary aerosol contribution to particulate pollution during haze events in China.* Nature, 2014. **514**(7521): p. 218.
3. Lelieveld, J., et al., *The contribution of outdoor air pollution sources to premature mortality on a global scale.* Nature, 2015. **525**(7569): p. 367.
4. Maynard, A.D., et al., *Safe handling of nanotechnology.* Nature, 2006. **444**(7117): p. 267.
5. Prüss-Ustün, A., et al., *Environmental risks and non-communicable diseases.* Bmj, 2019. **364**.
6. Maher, B.A., et al., *Magnetite pollution nanoparticles in the human brain.* Proceedings of the National Academy of Sciences, 2016. **113**(39): p. 10797-10801.
7. Peeples, L., *News Feature: How air pollution threatens brain health.* Proceedings of the National Academy of Sciences, 2020: p. 202008940.
8. Calderon-Garciduenas, L., et al., *DNA damage in nasal and brain tissues of canines exposed to air pollutants is associated with evidence of chronic brain inflammation and neurodegeneration.* Toxicologic pathology, 2003. **31**(5): p. 524-538.
9. Chen, H., et al., *Living near major roads and the incidence of dementia, Parkinson's disease, and multiple sclerosis: a population-based cohort study.* The Lancet, 2017. **389**(10070): p. 718-726.
10. Sunyer, J., et al., *Association between traffic-related air pollution in schools and cognitive development in primary school children: a prospective cohort study.* PLoS Med, 2015. **12**(3): p. e1001792.
11. Harrel, S.K. and J. Molinari, *Aerosols and splatter in dentistry: a brief review of the literature and infection control implications.* The Journal of the American Dental Association, 2004. **135**(4): p. 429-437.
12. Kadaifciler, D.G., S. Ökten, and B. Sen, *Mycological contamination in dental unit waterlines in Istanbul, Turkey.* Brazilian Journal of Microbiology, 2013. **44**(3): p. 977-981.
13. Tellier, R., et al., *Recognition of aerosol transmission of infectious agents: a commentary.* BMC infectious diseases, 2019. **19**(1): p. 101.
14. Peng, X., et al., *Transmission routes of 2019-nCoV and controls in dental practice.* International Journal of Oral Science, 2020. **12**(1): p. 1-6.
15. Morawska, L. and D.K. Milton, *It is time to address airborne transmission of COVID-19.* Clinical Infectious Diseases, 2020. **7**.
16. Taira, M., et al., *Characterization of aerosols and fine particles produced in dentistry and their health risk assessments.* Nano Biomedicine, 2009. **1**(1): p. 9-15.
17. Pope Iii, C.A., et al., *Lung cancer, cardiopulmonary mortality, and long-term exposure to fine particulate air pollution.* Jama, 2002. **287**(9): p. 1132-1141.
18. Kulmala, M., et al., *Direct observations of atmospheric aerosol nucleation.* Science, 2013. **339**(6122): p. 943-946.
19. Rönkkö, T., et al., *Traffic is a major source of atmospheric nanocluster aerosol.* Proceedings of the National Academy of Sciences, 2017. **114**(29): p. 7549-7554.

20. Hietikko, R., et al., *Diurnal variation of nanocluster aerosol concentrations and emission factors in a street canyon.* Atmospheric environment, 2018. **189**: p. 98-106.
21. Sgro, L.A., et al., *Measurements of nanoparticles of organic carbon and soot in flames and vehicle exhausts.* Environmental science & technology, 2008. **42**(3): p. 859-863.
22. Liati, A., et al., *Metal nanoparticles in diesel exhaust derived by in-cylinder melting of detached engine fragments.* Atmospheric environment, 2015. **101**: p. 34-40.
23. Nosko, O., J. Vanhanen, and U. Olofsson, *Emission of 1.3–10 nm airborne particles from brake materials.* Aerosol Science and Technology, 2017. **51**(1): p. 91-96.
24. Anenberg, S., et al., *A global snapshot of the air pollution‐related health impacts of transportation sector emissions in 2010 and 2015.* International Council on Clean Transportation: Washington, DC, USA, 2019.
25. Scovronick, N., et al., *The impact of human health co-benefits on evaluations of global climate policy.* Nature communications, 2019. **10**(1): p. 1-12.
26. Sirelkhatim, A., et al., *Review on zinc oxide nanoparticles: antibacterial activity and toxicity mechanism.* Nano-Micro Letters, 2015. **7**(3): p. 219-242.
27. Shyjumon, I., et al., *Structural deformation, melting point and lattice parameter studies of size selected silver clusters.* The European Physical Journal D-Atomic, Molecular, Optical and Plasma Physics, 2006. **37**(3): p. 409-415.
28. Rogers, L. and J. Reed, *The adhesion of particles undergoing an elastic-plastic impact with a surface.* Journal of Physics D: Applied Physics, 1984. **17**(4): p. 677.
29. Xu, J., et al., *Atomic scale deformation in the solid surface induced by nanoparticle impacts.* Nanotechnology, 2005. **16**(6): p. 859.
30. Guo, D., G. Xie, and J. Luo, *Mechanical properties of nanoparticles: basics and applications.* Journal of Physics D: Applied Physics, 2013. **47**(1): p. 013001.
31. Stace, A.J., *Molecular dynamic simulations of the elastic and inelastic surface scattering of nanoparticles.* Physical Chemistry Chemical Physics, 2014. **16**(7): p. 3077-3086.
32. Hickey, A.J., et al., *Physical characterization of component particles included in dry powder inhalers. I. Strategy review and static characteristics.* Journal of pharmaceutical sciences, 2007. **96**(5): p. 1282-1301.
33. Mohanraj, V. and Y. Chen, *Nanoparticles-a review.* Tropical Journal of Pharmaceutical Research, 2006. **5**(1): p. 561-573.
34. Nel, A.E., et al., *Understanding biophysicochemical interactions at the nano–bio interface.* Nature materials, 2009. **8**(7): p. 543.
35. Spielman, L.A. and S.L. Goren, *Capture of small particles by London forces from low-speed liquid flows.* Environmental Science & Technology, 1970. **4**(2): p. 135-140.
36. Sinha-Ray, S., et al., *Application of solution-blown 20–50 nm nanofibers in filtration of nanoparticles: The efficient van der Waals collectors.* Journal of membrane science, 2015. **485**: p. 132-150.
37. Biswas, P. and C.-Y. Wu, *Nanoparticles and the environment.* Journal of the Air & Waste Management Association, 2005. **55**(6): p. 708-746.
38. Wang, C.-s. and Y. Otani, *Removal of nanoparticles from gas streams by fibrous filters: a review.* Industrial & Engineering Chemistry Research, 2012. **52**(1): p. 5-17.
39. Abdolghader, P., et al., *Airborne Nanoparticle Filtration Performance of Fibrous Media: A review.* Science and Technology for the Built Environment, 2018(just-accepted).
40. Preining, O., *The physical nature of very, very small particles and its impact on their behaviour.* Journal of Aerosol Science, 1998. **29**(5-6): p. 481-495.

41. Preining, O., *The physical nature of very, very small particles and its impact on their behavior*, in *Developments in Surface Contamination and Cleaning: Fundamentals and Applied Aspects*. 2008, Elsevier. p. 3-24.
42. Dahneke, B., *Kinetic theory of the escape of particles from surfaces.* Journal of Colloid and Interface Science, 1975. **50**(1): p. 89-107.
43. Hiller, R. and F. Löffler, *Influence of particle impact and adhesion on the collection efficiency of fibre filters.* German Chemical Engineering, 1980. **3**: p. 327-332.
44. Wang, H.-C., *Theoretical adhesion efficiency for particles impacting a cylinder at high Reynolds number.* Journal of Aerosol Science, 1986. **17**(5): p. 827-837.
45. Wang, H.-C. and G. Kasper, *Filtration efficiency of nanometer-size aerosol particles.* Journal of Aerosol Science, 1991. **22**(1): p. 31-41.
46. Mouret, G., et al., *Discussion about the thermal rebound of nanoparticles.* Separation and Purification Technology, 2011. **78**(2): p. 125-131.
47. DelRio, F.W., et al., *The role of van der Waals forces in adhesion of micromachined surfaces.* Nature materials, 2005. **4**(8): p. 629.
48. Wang, S., et al., *A new technique for nanoparticle transport and its application in a novel nano-sieve.* Scientific reports, 2018. **8**(1): p. 9682.
49. Björk, J., et al., *Adsorption of aromatic and anti-aromatic systems on graphene through π− π stacking.* The Journal of Physical Chemistry Letters, 2010. **1**(23): p. 3407-3412.
50. Kawai, S., et al., *Van der Waals interactions and the limits of isolated atom models at interfaces.* Nature communications, 2016. **7**: p. 11559.
51. Israelachvili, J.N., *Intermolecular and surface forces*. 2011: Academic press.
52. Weiss, W. and W. Ranke, *Surface chemistry and catalysis on well-defined epitaxial iron-oxide layers.* Progress in Surface Science, 2002. **70**(1-3): p. 1-151.
53. Bolis, V., *Fundamentals in adsorption at the solid-gas interface. Concepts and thermodynamics*, in *Calorimetry and thermal methods in catalysis*. 2013, Springer. p. 3-50.
54. Do, D.D., *Adsorption analysis: equilibria and kinetics*. Vol. 2. 1998: Imperial college press London.
55. Yang, R.T., *Gas separation by adsorption processes*. 2013: Butterworth-Heinemann.
56. Kisliuk, P., *The sticking probabilities of gases chemisorbed on the surfaces of solids.* Journal of Physics and Chemistry of Solids, 1957. **3**(1-2): p. 95-101.
57. Chernyakov, A., *Filtration of nanoaerosols through porous materials with allowance for desorption processes.* Colloid Journal, 2016. **78**(5): p. 717-721.
58. Givehchi, R., Q. Li, and Z. Tan, *Filtration of Sub-3.3 nm Tungsten Oxide Particles Using Nanofibrous Filters.* Materials, 2018. **11**(8): p. 1277.
59. Ardkapan, S.R., et al., *Filtration efficiency of an electrostatic fibrous filter: Studying filtration dependency on ultrafine particle exposure and composition.* Journal of Aerosol Science, 2014. **72**: p. 14-20.
60. Dowling, A., et al., *Possible Adverse Health Environmental and Safety Impacts.* Nanoscience and Nanotechnologies: Opportunities and Uncertainties, The Royal Society & The Royal Academy of Engineering, 2004: p. 35-51.
61. Yang, W., J.I. Peters, and R.O. Williams, *Inhaled nanoparticles—a current review.* International Journal of Pharmaceutics, 2008. **356**(1): p. 239-247.
62. Curtius, J. *Nucleation of atmospheric particles*. in *EPJ Web of Conferences*. 2009. EDP Sciences.

63. Buseck, P.R. and K. Adachi, *Nanoparticles in the atmosphere.* Elements, 2008. **4**(6): p. 389-394.
64. Jiang, J., G. Oberdörster, and P. Biswas, *Characterization of size, surface charge, and agglomeration state of nanoparticle dispersions for toxicological studies.* Journal of Nanoparticle Research, 2009. **11**(1): p. 77-89.
65. Sun, Q., et al., *Appearance of bulk properties in small tungsten oxide clusters.* The Journal of chemical physics, 2004. **121**(19): p. 9417-9422.
66. Uppenbrink, J., *Unconventional Clusters.* Science, 2001. **292**(5526): p. 2401-2401.
67. Auffan, M., et al., *Towards a definition of inorganic nanoparticles from an environmental, health and safety perspective.* Nature nanotechnology, 2009. **4**(10): p. 634-641.
68. Bian, K., et al., *The strongest particle: size-dependent elastic strength and Debye temperature of PbS nanocrystals.* The journal of physical chemistry letters, 2014. **5**(21): p. 3688-3693.
69. Jung, S.-c., D. Suh, and W.-s. Yoon, *Molecular dynamics simulation on the energy exchanges and adhesion probability of a nano-sized particle colliding with a weakly attractive static surface.* Journal of Aerosol Science, 2010. **41**(8): p. 745-759.
70. Kuninaka, H. and H. Hayakawa, *Origin of rebounds with a restitution coefficient larger than unity in nanocluster collisions.* Physical Review E, 2012. **86**(5): p. 051302.
71. Qi, W., et al., *Molecular dynamic simulation of the size-and shape-dependent lattice parameter of small Platinum nanoparticles.* Journal of Nanoparticle Research, 2009. **11**(3): p. 575-580.
72. Boskovic, L., et al., *Influence of particle shape on filtration processes.* Aerosol Science and Technology, 2005. **39**(12): p. 1184-1190.
73. Sabbagh-Kupelwieser, N., A. Maisser, and W.W. Szymanski, *From micro-to nanosized particles: Selected characterization methods and measurable parameters.* Particuology, 2011. **9**(3): p. 193-203.
74. Maynard, A.D. and E.D. Kuempel, *Airborne nanostructured particles and occupational health.* Journal of nanoparticle research, 2005. **7**(6): p. 587-614.
75. Protection, I.C.o.R., *Human respiratory tract model for radiological protection*. 1994: Published for the International Commission on Radiological Protection [By ….
76. Vincent, J., et al., *Aerosol inhalability at higher windspeeds.* Journal of Aerosol Science, 1990. **21**(4): p. 577-586.
77. Lin, L.Y., et al., *The effects of indoor particles on blood pressure and heart rate among young adults in Taipei, Taiwan.* Indoor air, 2009. **19**(6): p. 482-488.
78. Powell, M.C. and M.S. Kanarek, *Nanomaterial health effects-part 1: background and current knowledge.* WMJ-MADISON-, 2006. **105**(2): p. 16.
79. Chuanfang, Y., *Aerosol Filtration Application Using Fibrous Media—An Industrial Perspective.* Chinese journal of chemical Engineering, 2012. **20**(1): p. 1-9.
80. Wang, H., et al. *Study on the air filtration performance of nanofibrous membranes compared with conventional fibrous filters*. in *Nano/Micro Engineered and Molecular Systems (NEMS), 2010 5th IEEE International Conference on*. 2010. IEEE.
81. Zhu, M., et al., *Electrospun Nanofibers Membranes for Effective Air Filtration.* Macromolecular Materials and Engineering, 2016.
82. Givehchi, R. and Z. Tan, *An overview of airborne nanoparticle filtration and thermal rebound theory.* Aerosol Air Qual Res, 2014. **14**: p. 45-63.

83. Podgórski, A., A. Bałazy, and L. Gradoń, *Application of nanofibers to improve the filtration efficiency of the most penetrating aerosol particles in fibrous filters.* Chemical Engineering Science, 2006. **61**(20): p. 6804-6815.
84. Spurný, K. and J. Pich, *Analytical methods for determination of aerosols with help of membrane ultrafilters. VI. On the mechanism of membrane ultrafilter action.* Collection of Czechoslovak Chemical Communications, 1963. **28**(11): p. 2886-2894.
85. Ramarao, B.V., C. Tien, and S. Mohan, *Calculation of single fiber efficiencies for interception and impaction with superposed Brownian motion.* Journal of Aerosol Science, 1994. **25**(2): p. 295-313.
86. Colbeck, I., *Aerosol Science: Technology and Applications*. 2014: John Wiley & Sons.
87. Podgórski, A. and A. Bałazy, *Novel formulae for deposition efficiency of electrically neutral, submicron aerosol particles in bipolarly charged fibrous filters derived using Brownian dynamics approach.* Aerosol Science and Technology, 2008. **42**(2): p. 123-133.
88. Wang, J. and D.Y. Pui, *Filtration of aerosol particles by elliptical fibers: a numerical study.* Journal of Nanoparticle Research, 2009. **11**(1): p. 185-196.
89. Tabor, D., *Surface forces and surface interactions.* Journal of colloid and interface science, 1977. **58**(1): p. 2-13.
90. Greenwood, J. *Adhesion of elastic spheres*. in *Proceedings of the Royal Society of London A: Mathematical, Physical and Engineering Sciences*. 1997. The Royal Society.
91. Prokopovich, P. and V. Starov, *Adhesion models: From single to multiple asperity contacts.* Advances in colloid and interface science, 2011. **168**(1): p. 210-222.
92. Hertz, H., *On the contact of elastic solids.* J. Reine Angew Math., 1881. **92**: p. 156-171.
93. Johnson, K., K. Kendall, and A. Roberts. *Surface energy and the contact of elastic solids*. in *Proceedings of the Royal Society of London A: Mathematical, Physical and Engineering Sciences*. 1971. The Royal Society.
94. Derjaguin, B., *Theory of the stability of strongly charged lyophobic sols and the adhesion of strongly charged particles in solutions of electrolytes.* Acta Physicochim. USSR, 1941. **14**: p. 633-662.
95. Maugis, D. and H. Pollock, *Surface forces, deformation and adherence at metal microcontacts.* Acta Metallurgica, 1984. **32**(9): p. 1323-1334.
96. Sun, W., *Interaction forces between a spherical nanoparticle and a flat surface.* Physical Chemistry Chemical Physics, 2014. **16**(12): p. 5846-5854.
97. Sun, W., et al., *Calculation of normal contact forces between silica nanospheres.* Langmuir, 2013. **29**(25): p. 7825-7837.
98. Ortiz, F.G., P. Aguilera, and P. Ollero, *Biogas desulfurization by adsorption on thermally treated sewage-sludge.* Separation and Purification Technology, 2014. **123**: p. 200-213.
99. García, G., et al., *Use of different residues for high temperature desulphurisation of gasification gas.* Chemical Engineering Journal, 2011. **174**(2-3): p. 644-651.
100. Saleh, T.A., *Nanocomposite of carbon nanotubes/silica nanoparticles and their use for adsorption of Pb (II): from surface properties to sorption mechanism.* Desalination and Water Treatment, 2016. **57**(23): p. 10730-10744.
101. Malik, D.S., C.K. Jain, and A.K. Yadav, *Heavy Metal Removal by Fixed‐Bed Column–A Review.* ChemBioEng Reviews, 2018. **5**(3): p. 173-179.
102. Crhribi, A. and M. Chlendi, *Modeling of fixed bed adsorption: application to the adsorption of an organic dye.* Asian J. Textile, 2011. **1**: p. 161-171.

103. Cheng, T., et al., *Prediction of breakthrough curves for adsorption on activated carbon fibers in a fixed bed.* Carbon, 2004. **42**(15): p. 3081-3085.
104. Das, D., V. Gaur, and N. Verma, *Removal of volatile organic compound by activated carbon fiber.* Carbon, 2004. **42**(14): p. 2949-2962.
105. Zhang, X., S. Chen, and H.T. Bi, *Application of wave propagation theory to adsorption breakthrough studies of toluene on activated carbon fiber beds.* Carbon, 2010. **48**(8): p. 2317-2326.
106. Ortiz, F.G., P. Aguilera, and P. Ollero, *Modeling and simulation of the adsorption of biogas hydrogen sulfide on treated sewage–sludge.* Chemical Engineering Journal, 2014. **253**: p. 305-315.
107. Sui, H., et al., *Removal and recovery of o-xylene by silica gel using vacuum swing adsorption.* Chemical Engineering Journal, 2017. **316**: p. 232-242.
108. Qiu, H., et al., *Critical review in adsorption kinetic models.* Journal of Zhejiang University-Science A, 2009. **10**(5): p. 716-724.
109. Zhang, T., et al., *Investigation of nanoparticle adsorption during transport in porous media.* SPE Journal, 2014.
110. Khalfaoui, M., et al., *New theoretical expressions for the five adsorption type isotherms classified by BET based on statistical physics treatment.* Journal of colloid and interface science, 2003. **263**(2): p. 350-356.
111. Brunauer, S., et al., *On a theory of the van der Waals adsorption of gases.* Journal of the American Chemical society, 1940. **62**(7): p. 1723-1732.
112. Foo, K. and B. Hameed, *Insights into the modeling of adsorption isotherm systems.* Chemical Engineering Journal, 2010. **156**(1): p. 2-10.
113. Simonin, J.-P., *On the comparison of pseudo-first order and pseudo-second order rate laws in the modeling of adsorption kinetics.* Chemical Engineering Journal, 2016. **300**: p. 254-263.
114. Tan, K. and B. Hameed, *Insight into the adsorption kinetics models for the removal of contaminants from aqueous solutions.* Journal of the Taiwan Institute of Chemical Engineers, 2017. **74**: p. 25-48.
115. Bhattacharyya, K.G. and A. Sharma, *Azadirachta indica leaf powder as an effective biosorbent for dyes: a case study with aqueous Congo Red solutions.* Journal of Environmental Management, 2004. **71**(3): p. 217-229.
116. Ho, Y.-S. and G. McKay, *Pseudo-second order model for sorption processes.* Process biochemistry, 1999. **34**(5): p. 451-465.
117. Ho, Y.-S., et al., *Sorption of lead ions from aqueous solution using tree fern as a sorbent.* Hydrometallurgy, 2004. **73**(1-2): p. 55-61.
118. Chinoune, K., et al., *Adsorption of reactive dyes from aqueous solution by dirty bentonite.* Applied Clay Science, 2016. **123**: p. 64-75.
119. Naushad, M., Z. ALOthman, and H. Javadian, *Removal of Pb (II) from aqueous solution using ethylene diamine tetra acetic acid-Zr (IV) iodate composite cation exchanger: kinetics, isotherms and thermodynamic studies.* Journal of Industrial and Engineering Chemistry, 2015. **25**: p. 35-41.
120. Zarezadeh-Mehrizi, M. and A. Badiei, *Highly efficient removal of basic blue 41 with nanoporous silica.* Water Resources and Industry, 2014. **5**: p. 49-57.
121. Vincent, T., et al., *Thallium (I) sorption using Prussian blue immobilized in alginate capsules.* Carbohydrate polymers, 2014. **99**: p. 517-526.

122. Azizian, S., *Kinetic models of sorption: a theoretical analysis.* Journal of colloid and Interface Science, 2004. **276**(1): p. 47-52.
123. Crank, J., *The mathematics of diffusion, 347 pp*. 1956, Clarendon Press, Oxford.
124. Vermeulen, T., *Theory for irreversible and constant-pattern solid diffusion.* Industrial & Engineering Chemistry, 1953. **45**(8): p. 1664-1670.
125. Wang, H.-L., J.-L. Chen, and Z.-C. Zhai, *Study on thermodynamics and kinetics of adsorption of p-toluidine from aqueous solution by hypercrosslinked polymeric adsorbents.* ENVIRONMENTAL CHEMISTRY-BEIJING-, 2004. **23**(2): p. 192-196.
126. Weber, W.J. and J.C. Morris, *Kinetics of adsorption on carbon from solution.* Journal of the sanitary engineering division, 1963. **89**(2): p. 31-60.
127. Ho, Y.-S. and G. McKay, *Sorption of dye from aqueous solution by peat.* Chemical engineering journal, 1998. **70**(2): p. 115-124.
128. Haerifar, M. and S. Azizian, *Mixed surface reaction and diffusion-controlled kinetic model for adsorption at the solid/solution interface.* The Journal of Physical Chemistry C, 2013. **117**(16): p. 8310-8317.
129. Wilczak, A. and T.M. Keinath, *Kinetics of sorption and desorption of copper (II) and lead (II) on activated carbon.* Water Environment Research, 1993. **65**(3): p. 238-244.
130. Zhang, Y., *Dynamics of Nanoparticles in Stagnation Flames*. 2017: Springer.
131. Batista, C.A.S., R.G. Larson, and N.A. Kotov, *Nonadditivity of nanoparticle interactions.* Science, 2015. **350**(6257): p. 1242477.
132. Pinchuk, P. and K. Jiang. *Size-dependent Hamaker constants for silver and gold nanoparticles*. in *Physical Chemistry of Interfaces and Nanomaterials XIV*. 2015. International Society for Optics and Photonics.
133. Pinchuk, P. and A. Pinchuk. *Size-and temperature-dependent Hamaker constants for heterogeneous systems of interacting nanoparticles*. in *Physical Chemistry of Interfaces and Nanomaterials XV*. 2016. International Society for Optics and Photonics.
134. Jiang, K. and P. Pinchuk, *Temperature and size-dependent Hamaker constants for metal nanoparticles.* Nanotechnology, 2016. **27**(34): p. 345710.
135. Marcuzzo, J., et al., *Microporous activated carbono fiber felt produced from brasilian textile pan fiber.* X Encontro Brasileiro sobre Adsorção. Guarujá, SP, Brasil, 2014.
136. Stechkina, I. and N. Fuchs, *Studies on fibrous aerosol filters—I. Calculation of diffusional deposition of aerosols in fibrous filters.* Annals of occupational Hygiene, 1966. **9**(2): p. 59-64.
137. Payet, S., *Filtration stationnaire et dynamique des aérosols liquides submicroniques*. 1991, Université Paris-Est Créteil Val de Marne (UPEC).
138. Yeh, H.-C. and B.Y. Liu, *Aerosol filtration by fibrous filters—I. Theoretical.* Journal of aerosol science, 1974. **5**(2): p. 191-204.
139. Friedlander, S., *Mass and heat transfer to single spheres and cylinders at low Reynolds numbers.* AIChE journal, 1957. **3**(1): p. 43-48.
140. Natanson, G., *Diffusional precipitation of aerosols on a streamlined cylinder with a small capture coefficient.* Proc. Acad. Sci. USSR, Phys. Chem. Sec, 1957. **112**: p. 21-25.
141. Tomotika, S. and T. Aoi, *An expansion formula for the drag on a circular cylinder moving through a viscous fluid at small Reynolds numbers.* The Quarterly Journal of Mechanics and Applied Mathematics, 1951. **4**(4): p. 401-406.
142. Lamb, H., *Hydrodynamics*. 1993: Cambridge university press.

143. Kuwabara, S., *The forces experienced by randomly distributed parallel circular cylinders or spheres in a viscous flow at small Reynolds numbers.* Journal of the physical society of Japan, 1959. **14**(4): p. 527-532.
144. Happel, J., *Viscous flow relative to arrays of cylinders.* AIChE Journal, 1959. **5**(2): p. 174-177.
145. Pich, J., *The filtration theory of highly dispersed aerosols.* Staub Reinhalt. Luft, 1965. **5**(1965): p. 16-23.
146. Spielman, L. and S.L. Goren, *Model for predicting pressure drop and filtration efficiency in fibrous media.* Environmental Science & Technology, 1968. **2**(4): p. 279-287.
147. Brinkman, H., *C. 1947a A calculation of the viscous force exerted by a flowing fluid on a dense swarm of particles.* Appl. Sci. Res: p. 27-34.
148. Lee, K. and B. Liu, *Theoretical study of aerosol filtration by fibrous filters.* Aerosol Science and Technology, 1982. **1**(2): p. 147-161.
149. Hunt, B., T. Thajudeen, and C.J. Hogan Jr, *The single-fiber collision rate and filtration efficiency for nanoparticles I: The first-passage time calculation approach.* Aerosol Science and Technology, 2014. **48**(8): p. 875-885.
150. Kirsh, A. and I. Stechkina, *The Theory of Aerosol Filtration with Fibrous Filter: Fundamentals of Aerosol Science.* NY: Wiley, 1978: p. 165.
151. Kirsch, A. and N. Fuchs, *Studies on fibrous aerosol filters—III Diffusional deposition of aerosols in fibrous filters.* Annals of Occupational Hygiene, 1968. **11**(4): p. 299-304.
152. Liu, B.Y. and K.L. Rubow. *Efficiency, pressure drop and figure of merit of high efficiency fibrous and membrane filter media*. in *Proceedings of the Fifth world filtration congress, Nice*. 1990.
153. Payet, S., et al., *Penetration and pressure drop of a HEPA filter during loading with submicron liquid particles.* Journal of Aerosol Science, 1992. **23**(7): p. 723-735.
154. Hinds, W.C., *Aerosol Technology: Properties.* Behavior, and Measurement of airborne Particles (2nd, 1999.
155. Wang, J., D. Chen, and D. Pui, *Modeling of filtration efficiency of nanoparticles in standard filter media.* Journal of Nanoparticle Research, 2007. **9**(1): p. 109-115.
156. Kirsh, V., *The effect of van der Waals' forces on aerosol filtration with fibrous filters.* Colloid Journal, 2000. **62**(6): p. 714-720.
157. Peskir, G., *On the diffusion coefficient: The Einstein relation and beyond.* 2003.
158. Li, S., et al., *Adhesive particulate flow: The discrete-element method and its application in energy and environmental engineering.* Progress in Energy and Combustion Science, 2011. **37**(6): p. 633-668.
159. Heim, M., M. Attoui, and G. Kasper, *The efficiency of diffusional particle collection onto wire grids in the mobility equivalent size range of 1.2–8nm.* Journal of Aerosol Science, 2010. **41**(2): p. 207-222.
160. Shin, W., et al., *Experimental study of filtration efficiency of nanoparticles below 20nm at elevated temperatures.* Journal of Aerosol Science, 2008. **39**(6): p. 488-499.
161. Van Gulijk, C., E. Bal, and A. Schmidt-Ott, *Experimental evidence of reduced sticking of nanoparticles on a metal grid.* Journal of Aerosol Science, 2009. **40**(4): p. 362-369.
162. Kim, S.C., M.S. Harrington, and D.Y. Pui, *Experimental study of nanoparticles penetration through commercial filter media.* Journal of Nanoparticle Research, 2007. **9**(1): p. 117-125.

163. Rengasamy, S., et al., *Filtration performance of NIOSH-approved N95 and P100 filtering facepiece respirators against 4 to 30 nanometer-size nanoparticles.* Journal of occupational and environmental hygiene, 2008. **5**(9): p. 556-564.
164. Steffens, J. and J. Coury, *Collection efficiency of fiber filters operating on the removal of nano-sized aerosol particles: I—Homogeneous fibers.* Separation and purification technology, 2007. **58**(1): p. 99-105.
165. Givehchi, R., Q. Li, and Z. Tan, *Quality factors of PVA nanofibrous filters for airborne particles in the size range of 10–125 nm.* Fuel, 2016. **181**: p. 1273-1280.
166. Kim, C.S., et al., *Filtration efficiency of a fibrous filter for nanoparticles.* Journal of nanoparticle research, 2006. **8**(2): p. 215-221.
167. Otani, Y., et al., *Generation of nanometer size particles and their removal from air.* Advanced Powder Technology, 1995. **6**(4): p. 271-281.
168. Bałazy, A., A. Podgórski, and L. Gradoń, *Filtration of nanosized aerosol particles in fibrous filters. I–experimental results.* Journal of Aerosol Science, 2004. **35**: p. 967-980.
169. Dahneke, B., *The influence of flattening on the adhesion of particles.* Journal of Colloid and Interface Science, 1972. **40**(1): p. 1-13.
170. Weir, G. and P. McGavin. *The coefficient of restitution for the idealized impact of a spherical, nano-scale particle on a rigid plane.* in *Proceedings of the Royal Society of London A: Mathematical, Physical and Engineering Sciences*. 2008. The Royal Society.
171. Tsai, C.-J., D.Y. Pui, and B.Y. Liu, *Capture and rebound of small particles upon impact with solid surfaces.* Aerosol Science and Technology, 1990. **12**(3): p. 497-507.
172. Rennecke, S. and A. Weber, *On the pressure dependence of thermal rebound.* Journal of Aerosol Science, 2013. **58**: p. 129-134.
173. Gensch, M. and A. Weber, *Rebound behavior of nanoparticle-agglomerates.* Advanced Powder Technology, 2017.
174. Mo, Y., K.T. Turner, and I. Szlufarska, *Friction laws at the nanoscale.* Nature, 2009. **457**(7233): p. 1116.
175. Cheng, S., B. Luan, and M.O. Robbins, *Contact and friction of nanoasperities: Effects of adsorbed monolayers.* Physical review E, 2010. **81**(1): p. 016102.
176. Derjaguin, B.V., V.M. Muller, and Y.P. Toporov, *Effect of contact deformations on the adhesion of particles.* Journal of Colloid and interface science, 1975. **53**(2): p. 314-326.
177. Maugis, D., *Adhesion of spheres: the JKR-DMT transition using a Dugdale model.* Journal of colloid and interface science, 1992. **150**(1): p. 243-269.
178. Hamaker, H.C., *The London—van der Waals attraction between spherical particles.* physica, 1937. **4**(10): p. 1058-1072.
179. Kim, H.-Y., et al., *Van der Waals dispersion forces between dielectric nanoclusters.* Langmuir, 2007. **23**(4): p. 1735-1740.
180. Roque-Malherbe, R.M., *Adsorption and diffusion in nanoporous materials*. 2018: CRC press.
181. Nardin, M. and E. Papirer, *Powders and fibers: interfacial science and applications*. 2006: CRC Press.
182. Lyklema, J., *Principles of the stability of lyophobic colloidal dispersions in non-aqueous media.* Advances in Colloid and Interface Science, 1968. **2**(2): p. 67-114.
183. Aguilera, P. and F.G. Ortiz, *Prediction of fixed-bed breakthrough curves for H2S adsorption from biogas: Importance of axial dispersion for design.* Chemical Engineering Journal, 2016. **289**: p. 93-98.

184. Kulmala, M., et al., *Measurement of the nucleation of atmospheric aerosol particles.* Nature protocols, 2012. **7**(9): p. 1651-1667.
185. Jiang, J., D.-R. Chen, and P. Biswas, *Synthesis of nanoparticles in a flame aerosol reactor with independent and strict control of their size, crystal phase and morphology.* Nanotechnology, 2007. **18**(28): p. 285603.
186. Arenz, M., et al., *The effect of the particle size on the kinetics of CO electrooxidation on high surface area Pt catalysts.* Journal of the American Chemical Society, 2005. **127**(18): p. 6819-6829.
187. Alanen, J., et al., *The formation and physical properties of the particle emissions from a natural gas engine.* Fuel, 2015. **162**: p. 155-161.
188. Almeida, J., et al., *Molecular understanding of sulphuric acid–amine particle nucleation in the atmosphere.* Nature, 2013. **502**(7471): p. 359.
189. Knutson, E. and K. Whitby, *Aerosol classification by electric mobility: apparatus, theory, and applications.* Journal of Aerosol Science, 1975. **6**(6): p. 443-451.
190. de la Mora, J.F. and J. Kozlowski, *Hand-held differential mobility analyzers of high resolution for 1–30 nm particles: Design and fabrication considerations.* Journal of Aerosol Science, 2013. **57**: p. 45-53.
191. Jiang, J., et al., *Transfer functions and penetrations of five differential mobility analyzers for sub-2 nm particle classification.* Aerosol science and technology, 2011. **45**(4): p. 480-492.
192. Kangasluoma, J. and J. Kontkanen, *On the sources of uncertainty in the sub-3 nm particle concentration measurement.* Journal of Aerosol Science, 2017. **112**: p. 34-51.
193. Kangasluoma, J., et al., *Operation of the Airmodus A11 nano Condensation Nucleus Counter at various inlet pressures and various operation temperatures, and design of a new inlet system.* Atmos. Meas. Tech., 2016. **9**(7): p. 2977-2988.
194. Cai, R., et al., *A miniature cylindrical differential mobility analyzer for sub-3 nm particle sizing.* Journal of Aerosol Science, 2017. **106**: p. 111-119.
195. Cai, R., et al., *Characterization of a high-resolution supercritical differential mobility analyzer at reduced flow rates.* Aerosol Science and Technology, 2018: p. 1-12.
196. Stolzenburg, D., G. Steiner, and P.M. Winkler, *A DMA-train for precision measurement of sub-10 nm aerosol dynamics.* Atmospheric Measurement Techniques, 2017. **10**(4): p. 1639-1651.
197. Stolzenburg, M.R., et al., *Characterization of the TSI model 3086 differential mobility analyzer for classifying aerosols down to 1 nm.* Aerosol Science and Technology, 2018. **52**(7): p. 748-756.
198. Cai, R., et al., *Parameters governing the performance of electrical mobility spectrometers for measuring sub-3 nm particles.* Journal of Aerosol Science, 2018.
199. Chauveau, R., et al., *Values of the mass transfer coefficient of the linear driving force model for VOC adsorption on activated carbons.* Chemical engineering research and design, 2013. **91**(5): p. 955-962.
200. Patton, A., B. Crittenden, and S. Perera, *Use of the linear driving force approximation to guide the design of monolithic adsorbents.* Chemical Engineering Research and Design, 2004. **82**(8): p. 999-1009.
201. Kangasluoma, J., et al., *Remarks on ion generation for CPC detection efficiency studies in sub-3-nm size range.* Aerosol Science and Technology, 2013. **47**(5): p. 556-563.
202. Wimmer, D., et al., *Performance of diethylene glycol-based particle counters in the sub-3 nm size range.* Atmospheric Measurement Techniques, 2013. **6**(7): p. 1793.

203. Sem, G.J., *Design and performance characteristics of three continuous-flow condensation particle counters: a summary.* Atmospheric research, 2002. **62**(3-4): p. 267-294.
204. Wiedensohler, A., *An approximation of the bipolar charge distribution for particles in the submicron range.* J. Aerosol Sci., 1988. **19**(3): p. 387-389.
205. Dwivedi, P., et al., *Comparative study of removal of volatile organic compounds by cryogenic condensation and adsorption by activated carbon fiber.* Separation and Purification Technology, 2004. **39**(1-2): p. 23-37.
206. Wang, J. and X. Guo, *Adsorption kinetic models: Physical meanings, applications, and solving methods.* Journal of Hazardous Materials, 2020. **390**: p. 122156.
207. Baral, S.S., S.N. Das, and P. Rath, *Hexavalent chromium removal from aqueous solution by adsorption on treated sawdust.* Biochemical Engineering Journal, 2006. **31**(3): p. 216-222.
208. Liu, C., et al., *Transparent air filter for high-efficiency PM 2.5 capture.* Nature communications, 2015. **6**: p. 6205.
209. Hoek, E.M. and G.K. Agarwal, *Extended DLVO interactions between spherical particles and rough surfaces.* Journal of Colloid and Interface science, 2006. **298**(1): p. 50-58.
210. Wang, N., et al., *Superamphiphobic nanofibrous membranes for effective filtration of fine particles.* Journal of colloid and interface science, 2014. **428**: p. 41-48.
211. Gamio, L., *The workers who face the greatest coronavirus risk.* New York Times, 2020.
212. Rothe, C., et al., *Transmission of 2019-nCoV infection from an asymptomatic contact in Germany.* New England Journal of Medicine, 2020. **382**(10): p. 970-971.
213. Organization, W.H., *Modes of transmission of virus causing COVID-19: implications for IPC precaution recommendations: scientific brief, 27 March 2020*. 2020, World Health Organization.
214. AFFAIRS, A.C.O.S. and A.C.O.D. PRACTICE, *Infection control recommendations for the dental office and the dental laboratory.* The Journal of the American Dental Association, 1996. **127**(5): p. 672-680.
215. Safety, O. and H. Administration, *Occupational exposure to bloodborne pathogens: final rule.* Federal Register, 1991. **56**(235): p. 64004-64182.
216. Simu, M., et al., *COMPLEX CHARACTERIZATION OF DENTAL OFFICE AEROSOLS REVEALS IMPORTANT LOADS OF RISK ELEMENTS FOR THE HUMAN HEALTH.* DIGEST JOURNAL OF NANOMATERIALS AND BIOSTRUCTURES, 2014. **9**(4): p. 1429-1438.
217. Izzetti, R., et al., *COVID-19 transmission in dental practice: brief review of preventive measures in Italy.* Journal of Dental Research, 2020: p. 0022034520920580.
218. Mahmud, P.K., S.M. Ali, and D.K. Sabir, *Impacts of novel pandemic coronavirus (COVID-19) outbreak on dental practice: A review of the.*
219. (RCDSO), R.C.o.D.S.o.O., *COVID-19: Managing Infection Risks During In-Person Dental Care*. May 26, 2020.
220. Pippin, D.J., R.A. Verderame, and K.K. Weber, *Efficacy of face masks in preventing inhalation of airborne contaminants.* Journal of oral and maxillofacial surgery, 1987. **45**(4): p. 319-323.
221. Rupf, S., et al., *Exposure of patient and dental staff to fine and ultrafine particles from scanning spray.* Clinical oral investigations, 2015. **19**(4): p. 823-830.
222. Zhao, B., N. An, and C. Chen, *Using air purifier as a supplementary protective measure in dental clinics during the COVID-19 pandemic.* Infection Control & Hospital Epidemiology, 2020: p. 1-4.

223. Polednik, B., *Aerosol and bioaerosol particles in a dental office.* Environmental research, 2014. **134**: p. 405-409.
224. Sotiriou, M., et al., *Measurement of particle concentrations in a dental office.* Environmental monitoring and assessment, 2008. **137**(1-3): p. 351.
225. Raynor, P.C., et al., *Assessing potential nanoparticle release during nanocomposite shredding using direct-reading instruments.* Journal of occupational and environmental hygiene, 2012. **9**(1): p. 1-13.
226. Van Landuyt, K.L., et al., *Nanoparticle release from dental composites.* Acta biomaterialia, 2014. **10**(1): p. 365-374.
227. Lang, A., et al., *Nanoparticle concentrations and composition in a dental office and dental laboratory: A pilot study on the influence of working procedures.* Journal of occupational and environmental hygiene, 2018. **15**(5): p. 441-447.
228. Mädler, L. and S.K. Friedlander, *Transport of nanoparticles in gases: overview and recent advances.* Aerosol and Air Quality Research, 2007. **7**(3): p. 304-342.
229. Tan, Z., *Air pollution and greenhouse gases: from basic concepts to engineering applications for air emission control*. 2014: Springer.
230. Zemouri, C., et al., *Dental aerosols: microbial composition and spatial distribution.* Journal of Oral Microbiology, 2020. **12**(1): p. 1762040.
231. He, X., et al., *How does breathing frequency affect the performance of an N95 filtering facepiece respirator and a surgical mask against surrogates of viral particles?* Journal of occupational and environmental hygiene, 2014. **11**(3): p. 178-185.
232. Paxton, N.C., et al., *N95 Respiratory Masks for COVID-19: A Review of the Literature to Inform Local Responses to Global Shortages.* 2020.
233. Control, C.f.D. and Prevention, *Strategies for Optimizing the Supply of N95 Respirators [Internet]. 2020 [cited 2020 Mar 21]*.
234. Canada, G.o., *Infection prevention and control for COVID-19: Second interim guidance for acute healthcare settings*. 2020.
235. Patel, A., et al., *Personal protective equipment supply chain: lessons learned from recent public health emergency responses.* Health security, 2017. **15**(3): p. 244-252.
236. Viscusi, D.J., et al., *Evaluation of five decontamination methods for filtering facepiece respirators.* Annals of occupational hygiene, 2009. **53**(8): p. 815-827.
237. O'Hearn, K., et al., *Decontaminating N95 masks with Ultraviolet Germicidal Irradiation (UVGI) does not impair mask efficacy and safety: A Systematic Review.* 2020.
238. Lin, T.H., et al., *Relative survival of Bacillus subtilis spores loaded on filtering facepiece respirators after five decontamination methods.* Indoor air, 2018. **28**(5): p. 754-762.
239. Heimbuch, B.K., et al., *A pandemic influenza preparedness study: use of energetic methods to decontaminate filtering facepiece respirators contaminated with H1N1 aerosols and droplets.* American journal of infection control, 2011. **39**(1): p. e1-e9.
240. Lin, T.-H., et al., *Filter quality of electret masks in filtering 14.6–594 nm aerosol particles: Effects of five decontamination methods.* PloS one, 2017. **12**(10): p. e0186217.
241. O'Hearn, K., et al., *Efficacy and Safety of Disinfectants for Decontamination of N95 and SN95 Filtering Facepiece Respirators: A Systematic Review.* 2020.
242. Salter, W., et al., *Analysis of residual chemicals on filtering facepiece respirators after decontamination.* Journal of occupational and environmental hygiene, 2010. **7**(8): p. 437-445.
243. Kim, H.P., et al., *Re-use of health masks after autoclaving.* NanoImpact, 2020: p. 100231.

244. Gertsman, S., et al., *Microwave-and Heat-Based Decontamination of N95 Filtering Facepiece Respirators (FFR): A Systematic Review.* 2020.
245. Osha, O., *Information Booklet on Industrial Hygiene. Revised Edition. US Department of Labor OSHA*. 2006, OICA Publications, Occupational Safety and Health Administration, Washington ….
246. Grinshpun, S.A., et al., *Performance of an N95 filtering facepiece particulate respirator and a surgical mask during human breathing: two pathways for particle penetration.* Journal of occupational and environmental hygiene, 2009. **6**(10): p. 593-603.
247. Rengasamy, S. and B.C. Eimer, *Nanoparticle penetration through filter media and leakage through face seal interface of N95 filtering facepiece respirators.* Annals of occupational hygiene, 2012. **56**(5): p. 568-580.
248. Mukhametzanov, I.T., et al., *Assessing the protection provided by facepiece filtering respirator: New model involving spherical porous layer with annular peripheral opening.* Aerosol and Air Quality Research, 2016. **16**(10): p. 2428-2437.
249. Zhu, J., et al., *Performance Comparison of N95 and P100 Filtering Facepiece Respirators with Presence of Artificial Leakage.* Annals of Work Exposures and Health, 2020. **64**(2): p. 202-216.
250. Eshbaugh, J.P., et al., *N95 and P100 respirator filter efficiency under high constant and cyclic flow.* Journal of occupational and environmental hygiene, 2008. **6**(1): p. 52-61.
251. Rengasamy, S., et al., *A comparison of total inward leakage measured using sodium chloride (NaCl) and corn oil aerosol methods for air-purifying respirators.* Journal of occupational and environmental hygiene, 2018. **15**(8): p. 616-627.
252. Rengasamy, S., B.C. Eimer, and J. Szalajda, *A quantitative assessment of the total inward leakage of NaCl aerosol representing submicron-size bioaerosol through N95 filtering facepiece respirators and surgical masks.* Journal of occupational and environmental hygiene, 2014. **11**(6): p. 388-396.
253. Hui, D.S., et al., *Exhaled air dispersion during coughing with and without wearing a surgical or N95 mask.* Plos one, 2012. **7**(12): p. e50845.
254. Lindsley, W.G., et al., *Dispersion and exposure to a cough-generated aerosol in a simulated medical examination room.* Journal of occupational and environmental hygiene, 2012. **9**(12): p. 681-690.
255. McMahon, E., K. Wada, and A. Dufresne, *Implementing fit testing for N95 filtering facepiece respirators: practical information from a large cohort of hospital workers.* American journal of infection control, 2008. **36**(4): p. 298-300.
256. Lee, K., A. Slavcev, and M. Nicas, *Respiratory protection against Mycobacterium tuberculosis: quantitative fit test outcomes for five type N95 filtering-facepiece respirators.* Journal of occupational and environmental hygiene, 2004. **1**(1): p. 22-28.
257. Winter, S., et al., *Particulate face masks for protection against airborne pathogens-one size does not fit all: an observational study.* Critical Care and Resuscitation, 2010. **12**(1): p. 24.
258. Ramirez, J. and P. O'Shaughnessy, *Filter penetration and breathing resistance evaluation of respirators and dust masks.* Journal of occupational and environmental hygiene, 2017. **14**(2): p. 148-157.
259. Liu, B.Y., et al., *Respirator leak detection by ultrafine aerosols: a predictive model and experimental study.* Aerosol science and technology, 1993. **19**(1): p. 15-26.
260. Johnson, A.T., C.R. Dooly, and C.O. Dotson, *Respirator mask effects on exercise metabolic measures.* American Industrial Hygiene Association Journal, 1995. **56**(5): p. 467-473.

261. Johnson, A., W. Scott, and D. Caretti, *Review of recent research on respiration while wearing a respirator.* JOURNAL-INTERNATIONAL SOCIETY FOR RESPIRATORY PROTECTION, 2000. **18**(1): p. 22-30.
262. Johnson, A., et al., *Comparison of treadmill exercise performance times for several types of respirators.* JOURNAL-INTERNATIONAL SOCIETY FOR RESPIRATORY PROTECTION, 1999. **17**: p. 19-23.
263. Johnson, A.T., *Respirator masks protect health but impact performance: a review.* Journal of biological engineering, 2016. **10**(1): p. 1-12.
264. Lei, Z., et al., *Simulation and evaluation of respirator faceseal leaks using computational fluid dynamics and infrared imaging.* Annals of occupational hygiene, 2013. **57**(4): p. 493-506.
265. Saggese, N.P., et al., *An Interim Solution to the Decreased Availability of Respirators against COVID-19.* Anesthesia and Analgesia, 2020.
266. NIOSH, *Total inward leakage test for half-mask air-purifying particulate respirators*. 2009.
267. Allen, J. and L. Marr, *Re-thinking the Potential for Airborne Transmission of SARS-CoV-2.* 2020.
268. Bałazy, A., et al., *Manikin-based performance evaluation of N95 filtering-facepiece respirators challenged with nanoparticles.* Annals of Occupational Hygiene, 2006. **50**(3): p. 259-269.

Appendices

Appendix A: Spatial distribution of airborne particles in dental offices

A.1 Summary

Aerosols generated during dental procedures are one of the most significant routs for infection transmission. The purpose of this work is to assess the mechanisms of dental aerosol dispersion in dental offices. This study aimed to provide recommendations based on a quantitative study to minimize infection transmission in dental offices. The spread and removal of aerosol particles generated from a specific dental operation in a dental office are quantified for a single dental activity in the area near to the generation and corner of the office. The Effects of the air purifier, door condition, and particle sizes on the spread and removal of particles were investigated. The results help to develop technologies for the proper control of aerosols and splatters generated during the dental procedures. The results show that in the worst-case scenario it takes 95 min for 0.5 μm particles to settle and that it takes a shorter time for the larger particles. The air purifier expedited the removal time at least 6.3 times faster than the case with no air purifier in the generation zone. The particles may be transported from the source to the rest of the room, even when the particle concentrations in the generation zone dropped back to the background.

A.2 Introduction

Dental professionals, staff, and patients in dental offices are exposed to aerosol droplets, particles, and pathogenic microorganisms in the saliva and blood of the infected patients. The infectious microorganisms transmitted from saliva and nasopharyngeal secretions include pneumonic plague, Legionella pneumophila, tuberculosis, influenza viruses, herpes viruses, SARS virus (a form of coronavirus), pathogenic streptococci and staphylococci, blood-borne HIV, hepatitis viruses [11, 16]. Recently, COVID-19 joins this list because studies show that dentists are at high risk of exposure to

this virus, even more than nurses [211]. These infectious diseases could be transmitted from asymptomatic patients or patients in the recovery phase [212].

Infectious microorganisms spread in dental offices via various routes [14]. These routes include direct contact with body fluid of infected person, contact with surfaces and instruments that are touched, contact with the exhaled air by the infected person, and infection transmission through aerosols generated during the dental procedures [11-15]. The most considerable one is associated with aerosol smaller than 5 μm in diameter, recognized by the World Health Organization (WHO) in healthcare settings [213]. Splatters are another potential source of infection. Splatters are a mixture of air, water, and solid substances [16]. As the water evaporates, the smaller splatters linger longer in the air. In addition, exposure to non-biological aerosol particles in the dental offices and laboratories adversely affects human health [11, 17]. Many researchers have reported similar detrimental effects of the dental aerosol [1-4]. There is a direct correlation between the respiratory system infections of dental personnel and the concentration of generated aerosols due to the dental procedures. Nanoparticles may deposit in the alveolar region of the respiratory system. They can further enter the bloodstream, causing lung cancer, pulmonary and cardiovascular diseases, heart diseases, asthma, increased mortality, and so on [77, 78]. Furthermore, extremely small nanoparticles are mostly deposited in the head airways cause brain diseases such as Alzheimer [6].

According to the American Dental Association (ADA), the Centers for Disease Control and Prevention (CDC), and the Occupational Safety and Health Administration (OSHA), all the contaminated aerosol and splatters should be eliminated as much as possible from the air in the dental offices and related laboratories [214, 215]. It is necessary not only to the protection of the people in the dental offices but also to the prevention and control of disease transmission. Aerosol particles smaller than 50 μm in diameter and remain suspended in the air for up to 30 minutes after their formation [216]

and can be inhaled and enter the respiratory tract. However, smaller particles may remain airborne even longer, and the settlement might be affected by various conditions in the room.

Strict and effective infection control protocols are highly required to fight COVID-19 in dentaries [14]. General preventive measures and dental practice recommendations have been developed during the COVID-19 pandemic [217, 218]. The Ontario Dental Association guidelines, for example, require three hours between two patients during the COVID-19 pandemic [219]. This requirement poses a great challenge to the dental business due to reduced patient visits. Systematic research is needed for the development of alternative approaches for the decision makers.

Protection methods are constantly emphasized in the guidelines. Multiple approaches may help reduce the transmission of infectious diseases. The use of personal protection such as facemasks, gloves, and goggles are recommended to reduce the exposure of dental staff to aerosol; however, facemasks are not 100% effective [220, 221]. Measurements show a very high concentration of particles $9.7 \times 10^5\ \#/cm^3$ even behind surgical masks [221]. Rubber dams and suction tubes can protect patients, while their uses are limited to certain dental operations [11, 221]. A high-efficiency particulate air (HEPA) filter and the use of ultraviolet (UV), chambers in the ventilation system are another protecting methods that are effective after threats have become airborne and spread to the room. Extraoral high volume evacuators (EHVE) can also be used to remove the aerosol particles near to the area of particle generation [16]; however, its performance depends on the volumetric rate of evacuation and particle generation rate. In addition, using extra devices around the dental unit causes a restricted environment and inconvenience to the dentists. Recent COVID-19 outbreak has resulted in increased use of portable air purifiers in dental offices, despite little research has been published on their performances in dental offices [222]. The portable air purifiers can be located at the corners in the dental offices, and they cause much less inconvenience during dental operations than extra-oral high

evacuators do. In addition, these portable air purifiers do not require modification to existing ventilation systems.

Despite the research on number concentrations for micron [223, 224] and nano-size particles [225-227] related to the dental processes, to the best of knowledge, no research has been done on the dispersion and transport of airborne particles lingering in different parts of the office. The nature of the extensive surface area in dental offices may enhance the losses of particles onto various surfaces. Furthermore, research on the effects of air purifiers is needed to develop guidelines and protocols to reduce waiting time between patients and ensure the safe operation of dental offices.

The objective of this study is to understand the spread and removal of airborne dental particles in dental offices associated with a single dental activity. The remainder of this paper is presented as follows. Section A.3 presents the material and study design of concentration measurements in the dental office. In Section 0, the number concentration distribution of particles under the effects of operating conditions during the generation is investigated. After the generation, the spread and removal of particles with different sizes under the effects of operating conditions are investigated in Section A.4.2 at the generation zone and Section A.4.3 at the corner of the office. The effective removal mechanisms that depend on particle size are determined. Finally, the study is summarised in Section A.5. Results in this paper are deemed useful to the best practices for particle removal from dental offices.

A.3 Materials and Methods

A.3.1 Measurement site and instruments

The concentrations of micron and submicron particles were measured on May 15, 2020, in a dental operation room on the second floor of the dental clinic in Toronto, Ontario, Canada. Figure A- 1 shows the schematic of the operatory and layout of the instruments. This typical dental operatory room is 3 m

wide, 3 m long, and 4 m high; it has one dental unit. The mechanical ventilation system was off and the window was closed throughout the test. The temperature and relative humidity of the room air were 13.4^{0}C and 88%, respectively.

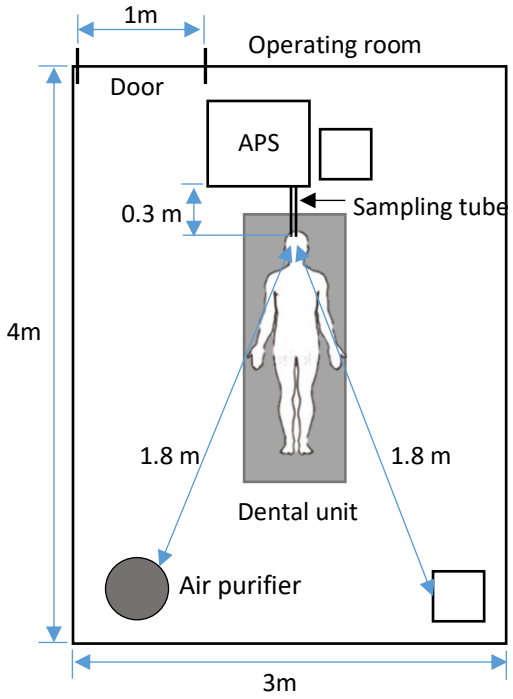

Figure A- 1 Schematic of the experimental setup

The number concentrations of particles were measured using an aerodynamic particle sizer spectrometer (APS, TSI 3321) and two optical particle counters (OPC, Handheld 3016, Lighthouse Worldwide Solutions Inc.). The APS took data every 5 min with 5 scans; each scan lasted 20 s; it can detect the particles in the range of 0.5-20 µm in diameter and those smaller than 0.5 µm. The APS was located on the left-hand side of the doctor, to prevent any inconvenience for the doctor during dental operations. A stainless-steel sampling tube, which is 1/4-inch of inner diameter and 0.3 m long, was connected to the inlet of the APS for sampling air 10 cm away from the operation area (*i.e.*, the patient's

mouth). Both OPCs were running continuously. One OPC was located beside the APS, and another OPC was 1.8 m away from the source. Both OPCs report particles with diameters of 0.3, 0.5, 1, 2, 5, 10 μm. The first OPC is calibrated against the APS.

A.3.2 Study design of dental operation on pig jaw

Before the operation, the room was uncontaminated for 15 hours before the background concentrations were measured at the source without air purification. As seen in Figure A- **2**, all particles in the background air were less than 10 #/cm^3 and those larger than 1 μm in diameter were less than 1 #/cm^3.

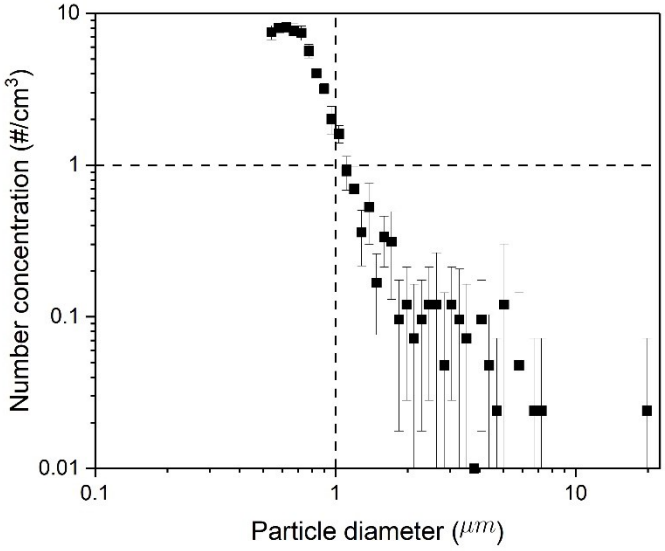

Figure A- 2 Background number concentration for 0.5- 20 μm aerosols

To begin with, particles were generated over 5 min of continuous drilling operation (high-speed handpiece) using a pig jaw. The particle number concentrations were measured during 5 min of continuous dental operation and afterward until the number concentrations reached the background.

Then we measured the airborne particle concentrations under six scenarios. Table A- **1** shows the conditions of these cases. All particles were generated by drilling the pig jaw with a high-speed hand piece. Other factors considered include the door condition (open and close) and air purifier (on and off, air flow rate, starting time). The air purifier (surgically clean air, model: JADE, SCA5000C) was 1.8 m away from the generation zone.

Table A- 1 Test cases and conditions

Case No.	Dental operation duration	Door (Open/Close)	Air purifier		
			On/Off	Fan speed	Air cleaning starting time
1	5 min	Open	Off	-	-
2	5 min	Open	On	High (312 CFM)	At the beginning of the operation
3	5 min	Close	Off	-	-
4	5 min	Close	On	Low (153 CFM)	After 5 min of operation
5	5 min	Close	On	High (312 CFM)	After 5 min of operation
6	5 min	Close	On	High (312 CFM)	At the beginning of the operation

A.4 Results and discussion

A.4.1 Particle generation during operation for five minutes

Figure A- **3** shows the incremental concentrations, which are defined as the differences between real concentrations and the background, during the five min of continuous dental operation and five min afterward. Figures illustrate the concentration for the particle size range of 0.5 to 4 μm, while the larger size concentration was negligible. The color scale defines number concentrations from 0 (blue) to 200 #/cm^3 (red). The values between these limits are mapped by blue, green, yellow, and orange. The purple shows values greater than 200 #/cm^3. As expected, the number concentration distribution varies with the operating conditions. For all cases, the smaller the particle size, the higher concentration is.

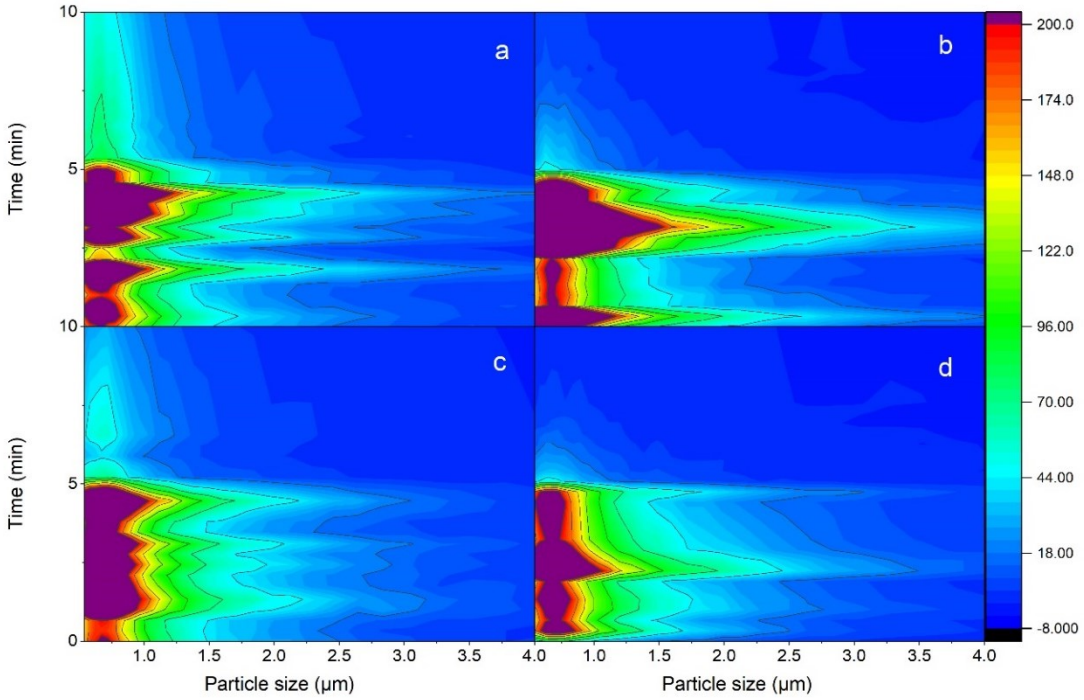

Figure A- 3 Concentrations of particles from 0.5 to 4 μm in the first 10 min measurement with closed door a) air purifier off, b) high-speed air purifier turned on from the beginning of particle generation with open door, and c) air purifier off, d) high-speed air purifier burned on from the beginning of particle generation.

In close-door cases, by comparing the case that no air purifier is running (Figure A- 3a) with the case that the air purifier is running at the beginning of operation (Figure A- 3b), it can be observed that particles have a wider distribution in Figure A- 3b, which means particles are growing to the larger sizes. For instance, the concentration of higher than 200 #/cm^3 is observed for 0.5-1.3 μm particles in Figure A- 3a, while, this range of concentration is observed for 0.5-1.5 μm particles in Figure A- 3b. Moreover, the concentration of 200-70 #/cm^3 is detected for 1.3-2.8 μm particles in Figure A- 3a;

however, 1.5–3.5 μm particles have this concentration range in Figure A- 3b. The real generated values for the Figure A- 3b is even more than this reported number because the removal process is started ad the beginning.

From this observation, it can be inferred that running the air purifier from the beginning causes air circulation. The air circulation can enhance the interaction between airborne particles leading to agglomeration in the area that particles are generated [228]. Thus, the particles may grow to the larger ones when the air purifier was on at the beginning of the operation. Growing to larger sizes is preferable in terms of particle removal. Removal by HEPA filter is size dependant; the larger sizes, the more probable filtration is. The filtration of micron particles is due to interception and impaction [229].

Similar behavior was observed when the door was open. Comparing Figure A- 3.c with 3.d shows that growing particles to larger sizes during the first 5 min while the air purifier was running from the beginning of the operation. The concentration of higher than 200 #/cm^3 is observed for 0.5-1 μm particles in Figure A- 3.a (air purifier off), while, this range of concentration is observed for 0.5-1.4 μm particles in Figure A- 3d. Moreover, the concentration of 200-70 #/cm^3 is detected for 1-2.2 μm particles in Figure A- 3c, however 1.4–2.5 μm particles have this concentration range in Figure A- 3d.

The particles generated in the 5-min long operation gradually spread in the room, and their concentrations were decreased by different mechanisms. They are introduced in the next sections.

A.4.2 Spread and removal of particles in the generated zone

A.4.2.1 Effects of air purifier and the door condition on the spread and removal of 0.5 particles

Figure A- 4 shows real-time number concentrations of 0.5 μm particles during the dental operation and afterward until they reached the background level. Figure A- 4a is for the close-door and Figure A- 4b

is for the open-door cases. The solid horizontal line marks the background concentration of 0.5 μm particles. The particle concentrations dropped gradually, likely by settlement on the surface[230], filtration by the air purifier, or dispersion in and out of the room. Table A- 2 summarizes the times it takes for the number concentrations to reach their background levels (removal times) for all six cases. In the worst-case scenario, when the door is closed and no air purifier is running in the room, it takes 95 min for 0.5 μm particles to settle.

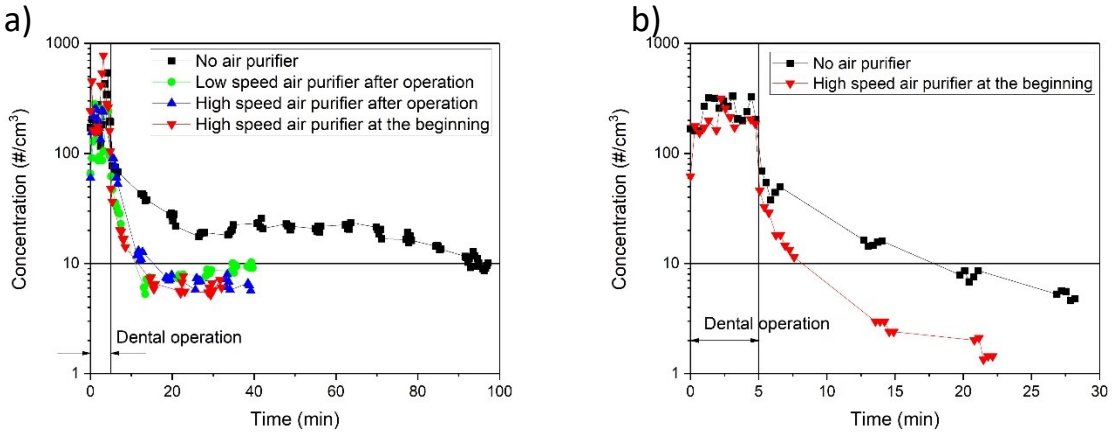

Figure A- 4 Spread and removal of 0.5-μm particle in (a) close door and (b) open door cases

Two conclusions can be drawn from the results in Figure A- 4. First, both Figure A- 4a and 4b show that the air purifier expedited particle removal from the air. For instance, Figure A- 4a shows that running high-speed air purifier enhanced the removal time of 0.5-μm particles at least 6.3 times faster than the case with no air purifier. Figure A- 4a shows the lowest particle concentrations in the room when the high-speed air purifier is running from the beginning of the operation. However, the removal time is almost the same for all these 3 cases: low-speed air purification after the dental operation, high-speed air purification after the dental operation, and high-speed air purification from the beginning of

the operation. It can be inferred that particles were captured with the HEPA filter and Activated Carbon Filter installed in the air purifier. In addition to filtration, enhancing air circulation in the room by the air purifier leads to faster particle settlement on the surface areas. These results suggest that air purifier has a crucial role in removing airborne contamination of dental offices in the generation zone.

Second, comparing the removal times of open-door cases (Figure A- 4b) with closed-door cases (Figure A- 4a) shows that the open door expedited the removal of 0.5 μm particles in the generation zone. The open door enables the dispersion of airborne particles by natural ventilation and air circulation. Dispersed particles may settle on the indoor surfaces and exit the room. It implies that the number concentration in the hallway was lower than inside the test room at the time of these measurements. On the other hand, external particles may enter the room and worsen the inside air quality if there are more particles outside of the door. This was the case on another day of measurement (*see* supplementary information). Therefore, the opening window, similar to the open-door cases, is recommended as a short term solution for the dental offices without air filtration systems.

The particle removal time varies with particle size although the air purifier and open door help reduce the concentration of all-size particles in the generation zone. The next section elaborates on the size dependency of particle spread and removal because smaller particles probably carry more infectious microorganisms because the concentration of smaller particles is higher than the larger ones.

A.4.2.2 Effects of particles size on particle removal

Figure A- 5 demonstrates the number concentrations of particles with sizes of sub-0.5, 0.5, 1, and 2.5 μm for all six cases. The background concentration is shown with the red horizontal line for <0.5 and 0.5 μm particles, green dash line for 1 μm particles and blue dotted line for 2.5 μm particles. The removal time for different particle sizes is marked with asterisks and their corresponding values are listed in Figure A- 5.

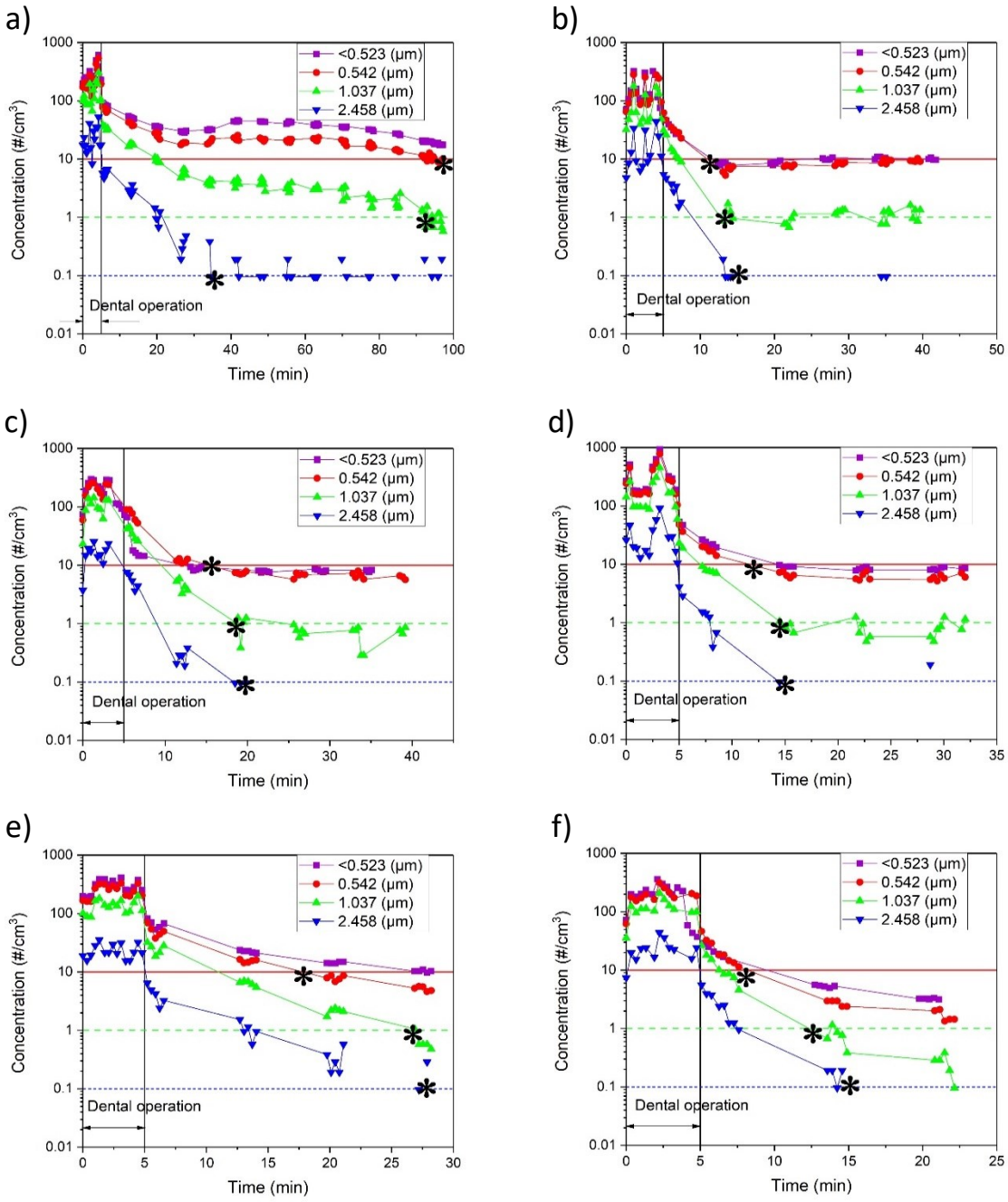

Figure A- 5 Number concentrations of sub-0.5, 0.5, 1, 2.5 μm particles measured in the generation zone for (a-d)closed-door cases: (a) air purifier off, (b) low-speed air purifier turned on after particle generation, (c) high-speed air purifier turned on after particle generation, (d) high-speed air purifier running from the beginning of particle generation and (e-f) open-door cases: (e) air purifier off, (f) high-speed air purifier running from the beginning of particle generation

Table A- 2 Removal times of the cases at the generation zone

No.	Door	Air purifier			Removal time at generation zone (min)		
		On/Off	Fan mode (Flow rate)	Air cleaning starting time	0.5 μm	1 μm	2.5 μm
1	Close	Off	-	-	95	92	35
2	Close	On	Low (153 CFM)	After dental operation	11	13	15
3	Close	On	High (312 CFM)	After dental operation	15	18.5	20
4	Close	On	High (312 CFM)	At the beginning of the dental operation	12	14.5	15
5	Open	Off	-	-	18	26.5	28
6	Open	On	High (312 CFM)	At the beginning of the dental operation	8	12.5	15

There are several mechanisms of particle removal from the air including settling, air circulation, and air filtration. First, all particles in a closed-door room without air circulation or filtration settle down because of gravity. It is well-known that the larger particles have higher gravitational settling velocity and that their removal times are shorter than the smaller particles. Figure A- 5 further confirms this mechanism. For example, 2.5-μm particles disappeared faster than those smaller. Second, air circulation leads to the dispersion of particles and their subsequent removal by settling on the surface areas or exiting the room or both. The drag force on a particle is also size-dependent. It usually takes a longer time for a larger particle to disperse than the smaller ones do. Figure A- 5 e indicates that air circulation through the open door expedited the particle removal, although the air purifier was off. In addition, Figure A- 5 e shows expedited removal of smaller particles and confirms that air circulation is the dominant mechanism in this case. Third, the filtration efficiency is also size dependant and it increased with the particle size for micron particles [229].

Figure A- 5 f for the high-speed air purifier running from the beginning of operation in the open door room shows the combined effects of all the three mechanisms. Air circulation may be the dominant mechanism of removal, although filtration also plays a significant role in the removal because it took a longer time to reduce the concentrations of 2.5-μm particles than the smaller ones.

Moreover, Figure A- 5 b, 5.c, and 5.d show that the removal times do not vary with particle size. Therefore, a combination of settling, air circulation, and air filtration all play roles in particle removal for these cases. Comparing these cases with that in Figure A- 5 f demonstrates the strong effects of air circulation due to the open door.

In summary, an air purifier running at high fan speed may ensure the removal of 0.5 to 3 μm particles, while air circulation is more effective for smaller particles. Since the door of dental offices might be open frequently, an air purifier with a strong fan may help prevent cross-contamination from one room to the other through the door. Nonetheless, our study herein does not undermine the effectiveness of external high volume evacuation (EHVE) and suction, which are often used near to the generation zone.

However, it does not mean that the room is completely cleaned even when the particle concentrations in the generation zone dropped back to the background. The particles may be transported from the source to the rest of the room. Dental staff walks around in the same room, and they often remove their masks for a short break at the corner, where there is little air circulation. It is necessary to investigate the spread of particles by analyzing the concentration at the corner of the room, and the results are presented in the next section.

A.4.3 Spread and removal of particles in the corner of the dental office

A.4.3.1 Effects of air purifier and the door condition on the spread and removal of 0.5 particles

Figure A- 6 compares the number concentrations of 0.5-μm particles in the corner with those at the generation zone for all 6 cases. This comparison helps quantify the number of particles in the corner when the number concentration in the generation zone dropped to the background level. The particles moved from the generation zone to the corner for some cases. Table A- 3 summarizes the times of travel indicated by the peaks and the ratio of concentrations in the corner to those in the generation zone. For example, the concentration peaks are observed for all sizes in 6 minutes when the door was close and the air purifier was running. In this case, the number concentration of peak in the corner is lower than the value in the generation zone. On the contrary, Figure A- 6d and 6f show that no peak is observed in the corner for 0.5 μm particles when the air purifier running from the beginning of operation with either open or closed door. These results indicate the effectiveness of high-speed high-efficiency air purification. Generally, it can be inferred that the peak is observed in the corner when the rate of particle settlement and removal from the air is lower than particle transport to the corner.

Table A- 3 indicates that it took 6 min for the concentration peak to reach the corner when the door was open and air purifier off. In comparison, Figure A- 6a shows that the travel time is shorter when the door was closed with the air purifier off (37 min). The air circulation result from the open door affected the contamination level in the corner. Therefore, an open door during operation may expedite the travel of particles from the source to the corner.

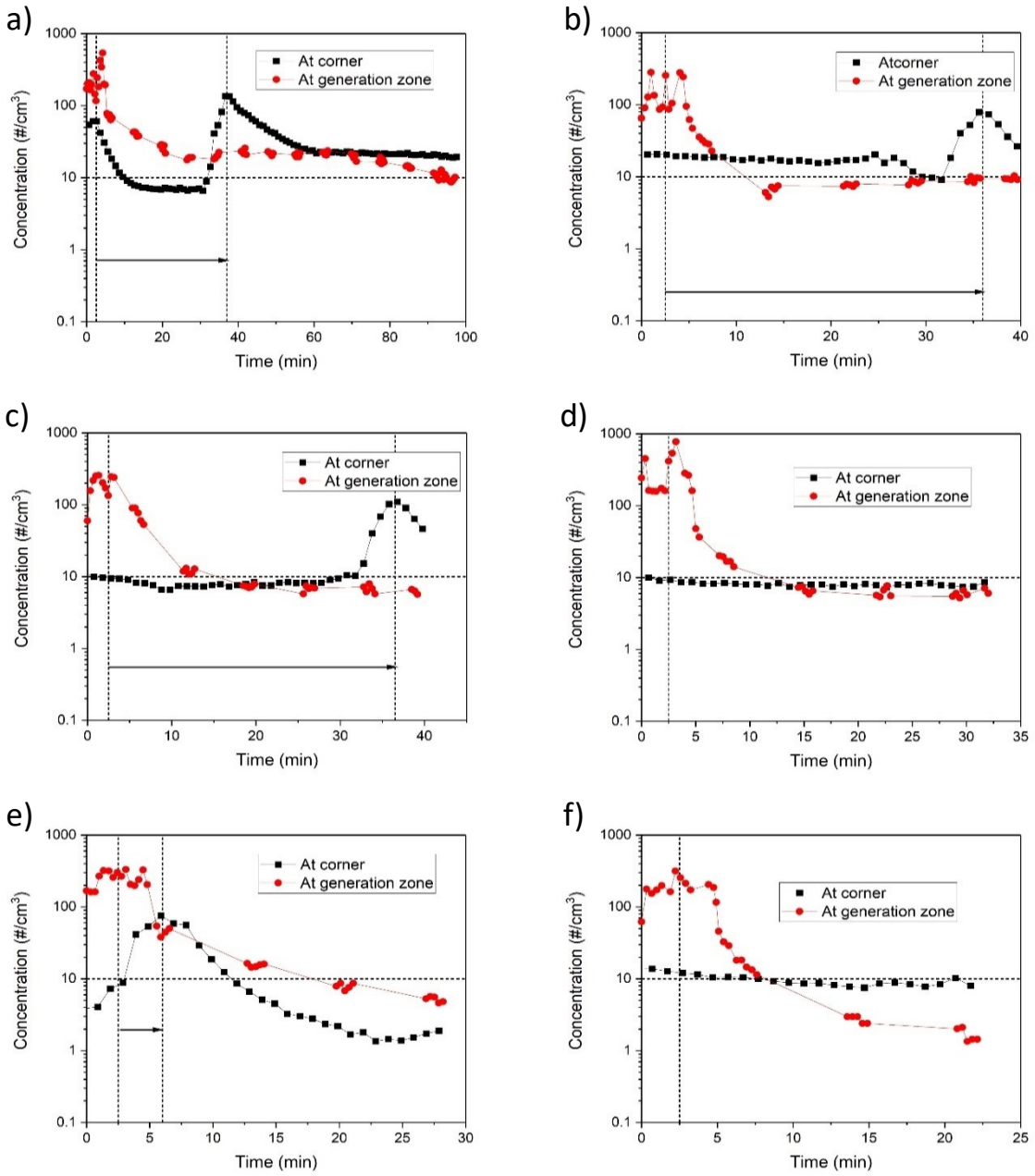

Figure A- 6 Comparison of the number concentrations of 0.5-μm particles in the corner with those at the generation zone for (a-d)closed-door cases: (a) air purifier off, (b) low-speed air purifier turned on after particle generation, (c) high-speed air purifier turned on after particle generation, (d) high-speed air purifier running from the beginning of particle generation and (e-f) open-door cases: (e) air purifier off, (f) high-speed air purifier running from the beginning of particle generation.

Table A- 3 The travel time and concentration ratios of 6 cases at the corner of the dental office

No.	Door	Air purifier			Travel time (min)			Concentration ratio		
		On/Off	Fan mode (Flow rate)	Air cleaning starting time	0.5 μm	1 μm	2.5 μm	0.5 μm	1 μm	2.5 μm
1	Close	Off	-	-	37	37	37	0.5	0.16	0.66
2	Close	On	Low (153 CFM)	After dental operation	36	36	36	0.33	0.1	0.4
3	Close	On	High (312 CFM)	After dental operation	36.5	36.5	36.5	0.33	0.11	0.5
4	Close	On	High (312 CFM)	At the beginning of the dental operation	-	-	-	-	-	-
5	Open	Off	-	-	6	6	6	0.26	0.11	0.5
6	Open	On	High (312 CFM)	At the beginning of the dental operation	-	21	21	-	0.016	0.06

The travel time of the concentration peak and peak concentration ratios are close to each other for the three close-door cases including air purifier off (Figure A- 6a), low-speed air purifier running after the operation (Figure A- 6b), and high-speed air purifier running after the operation (Figure A- 6c). Thus, the same fraction of particles reaches the corner at the same time for these cases. This is surprising because these results imply that the air circulation result from the air purifier has little impact on the air movement to the corner of the room.

A.4.3.2 Effects of particles size on particle removal

Figure A- 7 shows the number concentrations of 0.3-, 0.5-, 1-, 2.5-μm particles in the corner of the office for all six cases. All particles reached the corner with the same travel time as indicated by the concentration peaks observed in the corner except one case. Figure A- 7f shows the concentration peaks for 1- and 2.5-μm particles, but not for the 0.3- and 0.5-μm particles. This observation is expected based on two conclusions that were made earlier for this case. First, the removal rate of larger particles is lower than the smaller ones while the air circulation due to the open door and filtration are removal mechanisms. Second, the peak is observed in the corner when the rate of particle settlement and removal from the air is lower than particle transport to the corner. Thus, a fraction of 1, 2.5 μm particles, which is not removed from the air, traveled to the corner.

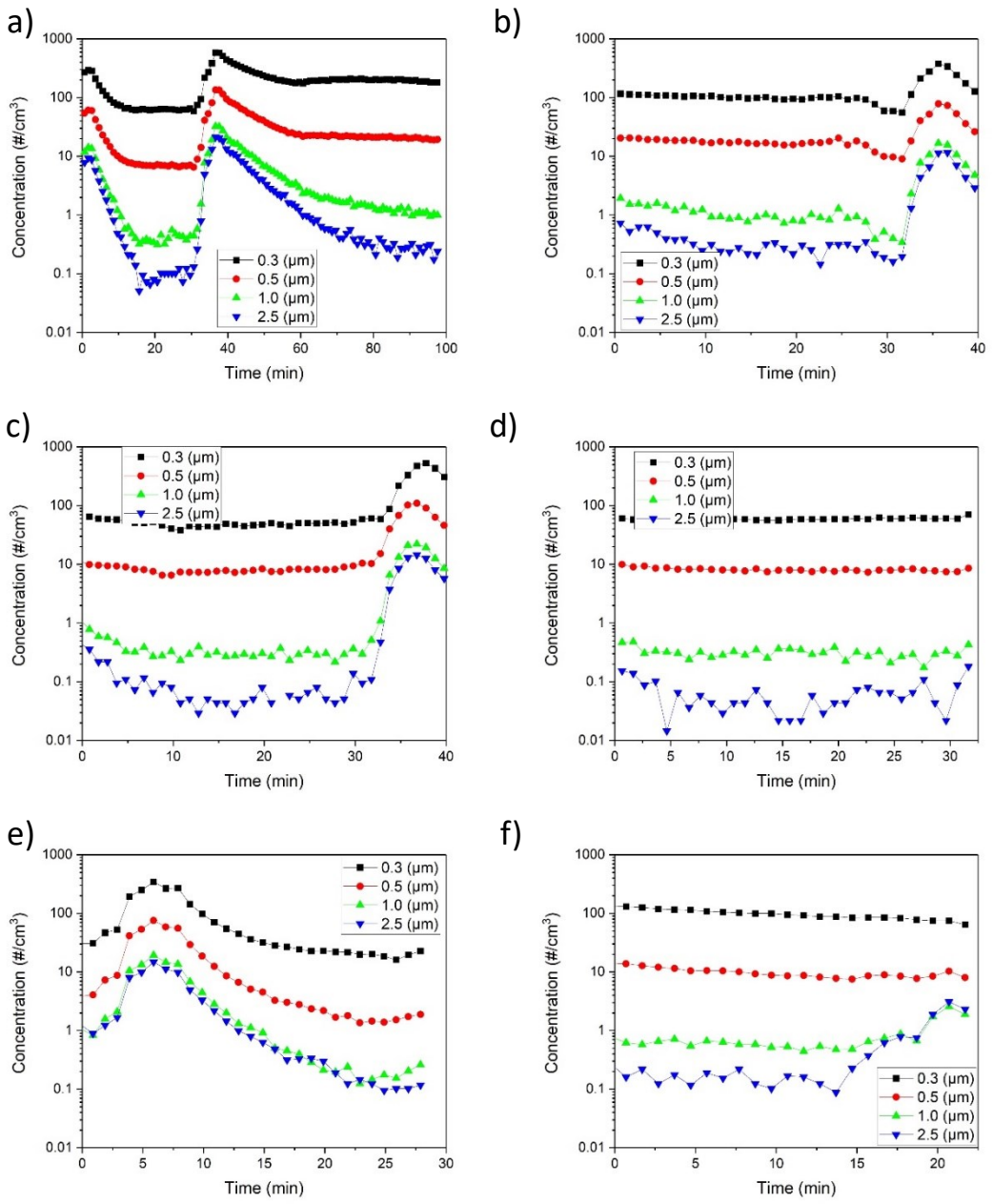

Figure A- 7 Number concentrations of sub-0.5, 0.5, 1, and 2.5 μm particles measured in the corner of the office for (a-d) closed-door cases: (a) air purifier off, (b) low-speed air purifier turned on after particle generation, (c) high-speed air purifier turned on after particle generation, (d) high-speed air purifier running from the beginning of particle generation and (e-f) open-door cases: (e) air purifier off, (f) high-speed air purifier running from the beginning of particle generation.

A.5 Conclusions

The following conclusions can be drawn from the results of this study:

- In the worst-case scenario with no protection system in the closed-door office and continuous high-speed drilling, it takes 95 min for 0.5 μm particles to settle and that it takes a shorter time for particles larger than 0.5 μm to be removed from the air. In the real operations with the patient, which usually is less than five minutes, air may be cleaner because of other measures like suction from the source (*i.e.*, the mouth).

- There are three size-dependent mechanisms for particle removal: gravity settling, air circulation, and air filtration. Technologies that combine all of them are the most effective in air cleaning. The air purifier expedited the removal time at least 6.3 times faster than the case with no air purifier in the generation zone. Running high-speed air purifier at the beginning of the operation is the most effective scenario in reducing airborne particle concentrations. The air purifier at one corner could not eliminate the concentration peak in the other corner of the room except for the case when the door was closed and the air purifier was running at the highest speed from the beginning of the operation.

- It is recommended to keep the door closed during the operation, otherwise, particles may enter the hallway through the open door. These particles may transmit diseases if they carry infectious microorganisms. In the dental offices without air purification devices, it is recommended to open the window(s) when possible to promote natural ventilation, however, it may cause accumulation of particles in a corner. In addition, staff should leave the room after the operation and close the door for particles to settle or exit the window(s). Admittedly, the surfaces should be cleaned because after that settled particles on.

Appendix B: Measuring the performance of alternative face-piece filtering respirators

B.1 Summary

In response to the unsustainable supply chain to provide single-use of face-piece filtering respirators (FFRs) and their shortage during the COVID-19 pandemic, decontamination, and reuse of masks or searching for alternatives are the options to prevent diseases transmission and control the outbreak. Moreover, the performance of FFRs plays an essential role in disease transmission. This research is aimed to provide a quantitative study on the performance of alternative masks to improve face-seal leakage. Alternative masks provide total inward leakage of less than 10% owing to the extended area in the face/mask interface. In addition, the effects of brace on the performance of FFRs are determined, using brace can improve the leakage through N95 up to 30%. The effect of single-cycle UV treatment on the face-seal leakage and performance of N95 masks are also investigated in this study.

B.2 Introduction

Respiratory masks are widely used in various healthcare environments to prevent transmission of infectious diseases and protect frontline workers [231, 232]. During COVID-19 outbreak guidelines and protocols established to prevent disease transmission and protect health care workers. Centers for Disease Control and Prevention (CDC) and the Public Health Agency of Canada (PHAC) have recommended health care workers to use personal protection equipment (PPE) such as N95 [233, 234]. In response to the unsustainable supply chain to provide single-use of FFRs [235] and their shortage during the COVID-19 pandemic, decontamination and reuse of mask or searching for alternatives are the options to prevent diseases transmission and control the outbreak.

A wide variety of FFR-decontamination methods has been investigated so far. A guideline is also provided for FFR-decontamination in critical situations by CDC. Radiation (UV-C, microwaves), moist heat (autoclaves), and chemical methods (bleach, ethanol, hydrogen peroxide)[236-239] are from those methods, although each of them has pros and cons, regardless of their effectiveness to remove infectious pathogens.

Among FFR-decontamination methods, chemical disinfection causes physical damage to FFRs [240], and residual chemicals on the FFRs after disinfection raised safety concerns [241, 242]. Using the autoclave method, the filtration performance of some types of FFRs drops significantly after autoclaving more than twice [243]. Moreover, significant degradation is reported with the autoclave method [244]. Microwaves and heat are effective and accessible disinfection methods to inactivate viruses, however, it causes physical damage on some mask types [244]. A single-cycle of decontamination using UV light is recommended in the literature, however, UV disinfection is not accessible to all institutions. A review of this method suggests further research on determining the impact of UV on mask fit [237].

Generally, the performance of FFRs is evaluated by three main indexes including filter efficiency, the face-seal leakage, and the pressure drop. N95 FFRs that are approved by the National Institute for Occupational Safety and Health (NIOSH) has a filtration efficiency of at least 95% for 75±20nm particles at 85 l/min flow rate, which represents breathing under heavy work. Despite the 95% filtration efficiency, wearing FFRs with loos fitting does not provide expected protection. According to the Occupational Safety and Health Administration (OSHA) protection factor (reverse of leakage) for FFRs should be higher than 10 [245].

Face-seal is reported as a more critical index than filter efficiency [246]. The research on the artificially leaked masks reveals that leaked masks with higher filtration efficiency are less protective

than the masks with lower filtration efficiency and no leakage [247]. Indeed, penetration through leakage may be much higher than the penetration through mask fabric [248-250], however, the penetration through face-seal leakage depends on particle size [251], leakage size and flow rate [252]. N95 mask no longer performs at 95% efficacy, while the leakage is greater than 0.1% of the mask surface area [248]. In addition to leakage through normal breathing, during coughing with wearing an N95 mask, air can expel up to 15 cm laterally [253, 254]. Thus, infection transmission is possible even if the patient wears an N95 mask. Although health care workers and most of the people with various face shapes around the world wear FFRs during outbreaks, loose-fitting or leakage is inevitable in the majority of them. Robust training and workplace verification of mask-wearing have been recommended in the literature [255, 256], however, a large proportion of individuals failed N95 masks fit test even after training [257].

Resistance to flow or pressure drop is another important index for mask performance. NIOSH requires that pressure drop should not exceed 35 mm H2O at 85 LPM [258]. Generally, the filters media with higher efficiency, provide higher pressure drop [259], however, higher pressure drop leads to leaking the exhaling air from mask/face interface. The exhaling air tends to exit the mask in the less resistant path, therefore leaking from the mask/face interface is more possible than penetration through the filter with higher resistance [260]. Although respiration with a mask does not limit the performance of individuals, it limits working time [261, 262]. The working hours are limited due to the physiological and psychological limitations caused by pressure drop; Higher pressure drop leads to Flow resistance results in the formation of dead volume of the lung as well as respirator causing a deficiency in oxygen inhalation [263]. Since the indexes to determine the performance of FFRs are interdependent, optimized indexes should be considered in mask design [264].

Face/mask interface is the boundary between the respiratory tract and the ambient atmosphere and plays the most important role in the performance of FFRs to control infection transmission. One of the solutions to improve leaking through the face/mask interface is using a brace [265] due to providing better fitting with the face, however, they do not use widely. Another solution is using the masks with an extended area in the face/mask interface. This research is aimed to provide a quantitative study on the performance of alternative masks to improve face-seal leakage. In addition to the alternative mask's role through shortage, this study can provide the basis of new mask design to improve FFRs performance. Anastacia or CPR masks combined with high-efficiency filters may improve the leakage through the interface. Anastacia or CPR masks as the alternatives are available through shortage, the plastic part is washable and the filter part is very cheap and can be replaced frequently. The effect of a brace in also investigated in this study as another solution to improve the performance of N95 to be used by a wide variety of individual face shape. The effect of single-cycle UV treatment on the face-seal leakage and performance of N95 masks are also investigated in this study.

B.3 Materials and Methods

B.3.1 Respiratory masks

Six combinations of 3 masks (Figure B- 1a-c) with 2 filters (Figure B- 1d, and e) were tested in this study. Reusable Anaesthesia Mask (Intersurgical, Alterna Clearflex Silicon mask), Disposable Anaesthesia Mask (Intersurgical, medium adult), and CPR Mask were combined with Medium Efficiency Filter (Intersiurgical, electrostatic), and Low Volume Breathing Filter (Drager, electrostatic). Moreover, N95 (3M™, 8210) was used for comparison with six alternative masks, investigating the effect of rubber brace (Figure B- 1f) and UV treatment.

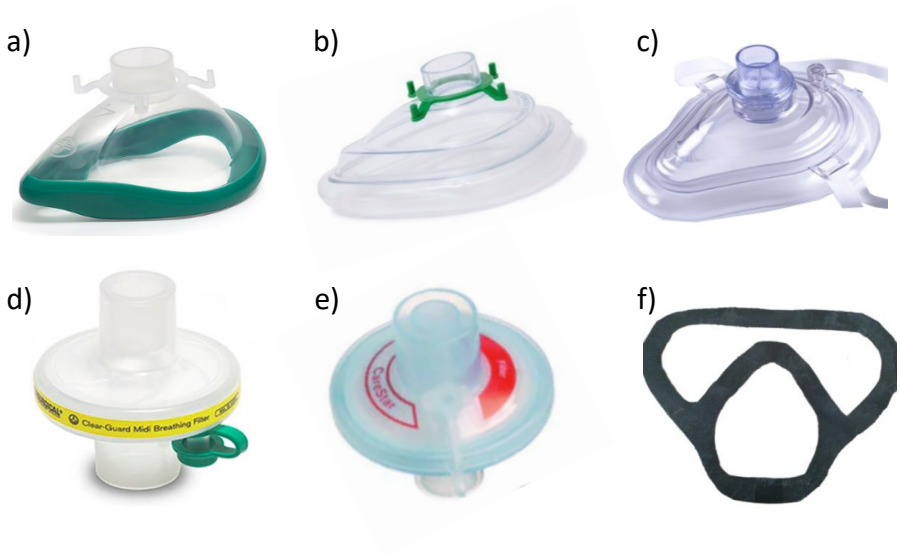

Figure B- 1 a) Reusable Anaesthesia Mask (M1), b) Disposable Anaesthesia Mask (M2) and c) CPR Mask (M3), d) Medium Efficiency Filter (F1), e) Low Volume Breathing Filter (F1), f) rubber brace

B.3.2 Experimental design

B.3.2.1 Experimental setup for filtration efficiency with NaCl nanoparticles and pressure drop

Figure B- 2 shows the experimental setup for filtration efficiency. A filtered air supply (TSI, Model 3074) is employed to provide dry, filtered air at a regulated pressure. The clean and dry air is fed to the particle generation system. Constant output atomizer (TSI model 3076) was employed to generate polydisperse NaCl particles, larger than 10 nm. NaCl material (Sigma-Aldrich) is mixed with fresh distilled water at 0. 1 g/liter. The generated passed through a radioactive neutralizer (Staticmaster Model P-2031) followed by the test filters. In this setup for the filtration test, a cone shape filter holder with an inner diameter of 25 mm is employed upstream of the measuring system. The measuring system for sizing and quantifying nanoparticles is the scanning mobility particle sizer coupled with a Faraday cup electrometer (SMPS+E, GRIMM Model 5.706). A thermal mass flow meter (TSI model 3063)

meeting the criteria of the isokinetic sampling measured the mainstream flow rate. The pressure gauge (Omegadyne, Model DPG409) was employed to measure pressure drop over the filter. The efficiency is measured for filter fabric with 1 in diameter at an air flow rate of 1.5 LPM, which corresponds to a face velocity of 5.09 cm/s.

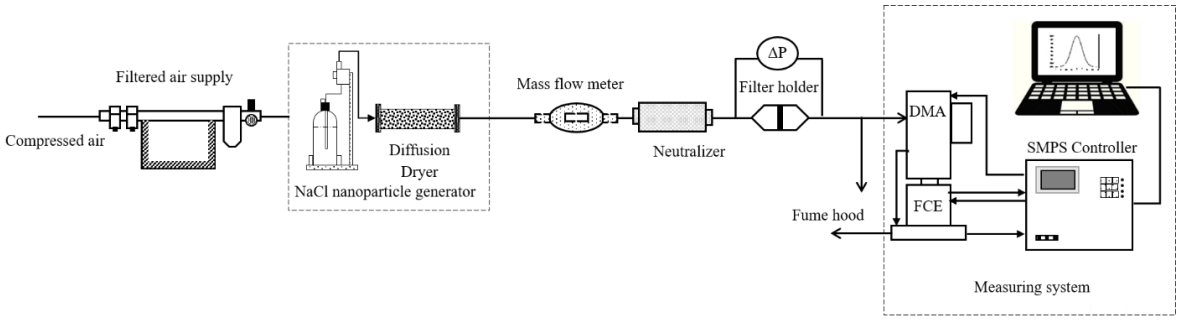

Figure B- 2 Experimental setup for filtration efficiency with NaCl nanoparticles

B.3.2.2 Experimental setup for face-seal leakage

Figure B- 3 shows the setup to test the performance of filtering face-piece respirators (FFRs). This setup is consistent with the OSHA-Accepted Fit Test Protocols. A filtered air supply (TSI, Model 3074) is employed to provide dry, filtered air at a regulated pressure. The clean and dry air is fed to the particle generation system. A fluidized bed aerosol generator (TSI, 3400A) was employed to generate dry powder in the size range of 0.5-5 μm. The generated particles are entered into a chamber ($24in \times 24in \times 24in$) with a constant rate and equal to the chamber outflow. Four fans were placed at each corner of the chamber on the floor to assure the aerosols were well mixed. Before each test, the dispersion airflow from the particle generator was adjusted and operated for 15–30 min to achieve uniform aerosol concentration in the chamber.

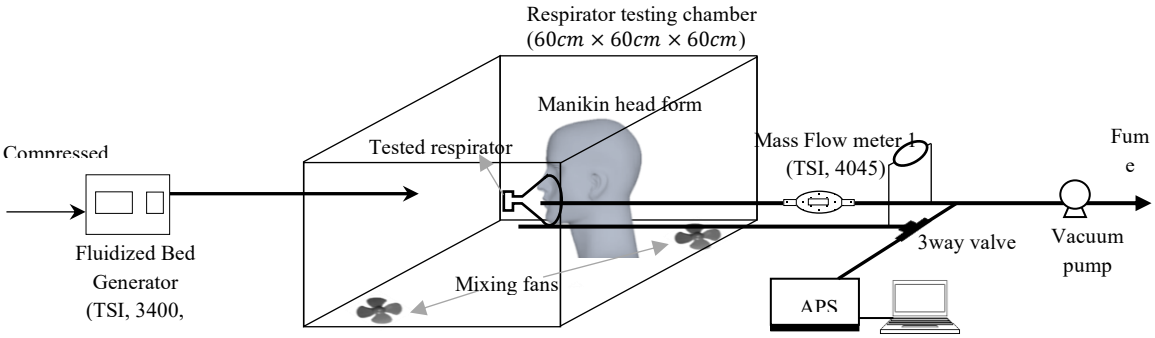

Figure B- 3 Experimental setup for testing the performance of the dust mask mounted on the manikin face

FFRs were mounted on a medium-sized hard plastic manikin head-form. The manikin is placed inside a chamber and a metal tube is inserted to the manikin head-form to simulate the upper respiratory tract. One end of this tube is connected to the mouth area and the other end is connected to the vacuum pump. The vacuum pump was used to simulate inhalation with a constant flow. The flow rate of 30 LPM was chosen as it represents the breathing flow rate for light work and monitored by a mass flow meter (TSI Model 3063). Three-way value enables sampling and sending the air to the measuring system. An aerodynamic particle sizer spectrometer (APS, TSI 3321) was used for measuring the sizes and concentrations of particles.

To take the samples outside of the respirator (inside the chamber), the sampling probe was set close to the nose area. Through the adjustment of the three way-valve, aerosol from either inside or outside of the respirator was sampled into the measuring system. The length of tubes for sampling inside or outside the respirator is equal to have the same particle loss in both. The pressure gauge (Omegadyne, Model DPG409) was employed to measure pressure drop over the respirator.

To measure the FFRs performance for particle size 10-150 nm, a constant output atomizer (TSI model 3076) was employed to generate polydispersed NaCl particles. NaCl material (Sigma-Aldrich) is mixed

with fresh distilled water at 0.1 g/liter. These aerosol particles were then passed through a diffusion dryer (TSI Model 3062) to reduce air humidity. Furthermore, the measuring system for sizing and quantifying nanoparticles is the scanning mobility particle sizer coupled with a Faraday cup electrometer (SMPS+E, GRIMM Model 5.706).

B.3.3 Test conditions

In the first part of this study, the performance of alternative masks with a combination of 3 masks and two filters are measured and compared to the performance of N95. Two different manikins are used to consider different face shapes. Both of them have a soft surface, simulating face skin. The first manikin (manikin A) is covered by a flexible thin silicon sheet and represents 3.5 % of US respirator wearers according to The NIOSH Bivariate Panel (NIOSH Panel) [266] by evaluating face width and face length indexes. The second manikin (manikin B) is made of soft silicone and represents 8.7 % of US respirator wearers.

In the second part of the study, the effect of brace on total inward leakage of N95 masks was determined. Rubber brace consists of two loops. The inner loop is fitted over the mask and the outer loop rests over the crown of the head to create a better seal.

In the third part of the study, the effect of UV treatment on the performance of N95 masks was investigated. N95 masks were treated with UV disinfector (PrescientX, Terminator COV), then filtration efficiency, pressure drop, and total inward leakage were quantified.

Droplets, released by breathing, talking, and coughing may contain viruses. The size of this droplet could be from 0.01 to hundreds of microns [267]. Considering dehydrated virus-containing droplets, filtration efficiency for nano sizes particles is measured. The filtration efficiency was determined by

measuring upstream (C_{up}) and downstream (C_{down}) number concentrations over the filter's fabric, given as:

$$\eta = 1 - \frac{C_{down}}{C_{up}} \times 100\% \quad \text{(B-1)}$$

The total inward leakage was also determined by measuring number concentration inside (C_{in}), and outside (C_{out}) of the mask when the mask is mounted on the manikin.

$$TIL = \frac{C_{in}}{C_{out}} \times 100\% \quad \text{(B-2)}$$

The overall performance of filter and mask is evaluated by the quality factor by Considering both filtration efficiency and pressure drop or total inward leakage and pressure drop [154]:

$$Q_F = \begin{cases} -\frac{\ln(1-\eta)}{\Delta P}, & filter \\ -\frac{\ln(TIL)}{\Delta P}, & mask \end{cases} \quad \text{(B-3)}$$

where ΔP is the pressure drop.

B.4 Results and discussion

B.4.1The performance of alternative masks

Figure B- 4.a demonstrates the filtration efficiency of filters F1 and F2 with NaCl nanoparticles. For both filters, the efficiency has a minimum value for the particles with about 30 nm size. According to this figure, the efficiency of filter 1 is about 10% higher than filter 2 for 10-150 nm particles. Since the pressure drop is close for both filters (0.06 in H_2O), filter 1 has a higher quality factor (Figure B- 4.b). The efficiency would be lower in higher face velocities [154]. The efficiency itself is not the only index to evaluate the performance of FFRs, thus the pressure drop and TIL of the FFRs are investigated in the following.

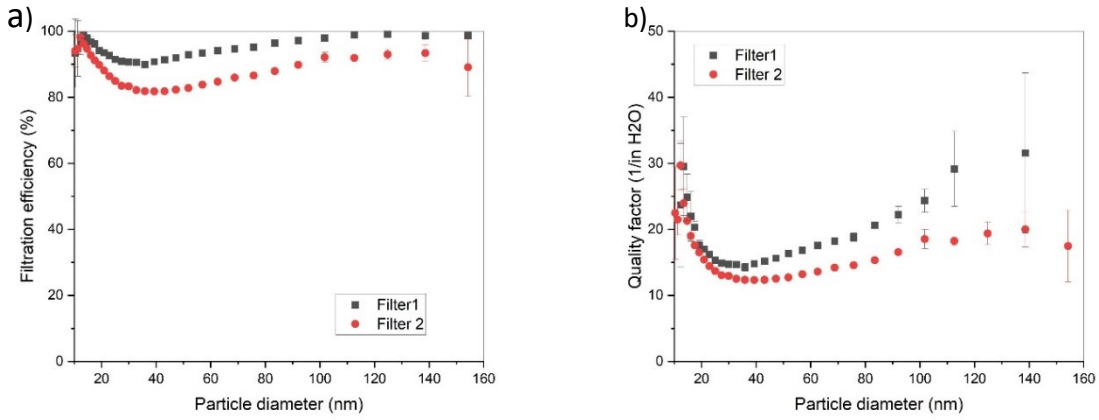

Figure B- 4 a) Filtration efficiency and b) quality factor of filter 1 and filter 2

Figure B- 5 demonstrates the pressure drop over filters for a range of face velocities (5-60 cm/s). For the masks with regular surface area (195 cm^2), the range of 30-85 LPM inhalation flow rates corresponds to 2.564 to 7.265 cm/s face velocity. Regarding the smaller size of the filters in alternative masks (19.635 cm^2), the correspondence face velocity is 10 times higher, 25.465 to 72.150 cm/s. According to Figure B- 5, the pressure drop is equal for both filters.

Resistance is a very important index to evaluate the performance of FFRs, since higher resistance may lead to lower pulmonary ventilation, which leads to the formation of dead spaces in FFRs and an increase of local CO2 concentration. High CO2 concentration causes a deficiency of inhaled oxygen or dyspnea [260]. NIOSH requires that pressure drop should not exceed 1.38 in H_2O at 85 LPM [258]. The pressure drop of the filter for breathing flow rates up to 50 (Face velocity 40 cm/s) is less than 1.38 in H_2O. Thus comparing to the NIOSH limitation, the pressure drop of alternative masks is within the acceptable range for low flow rates corresponding to light work.

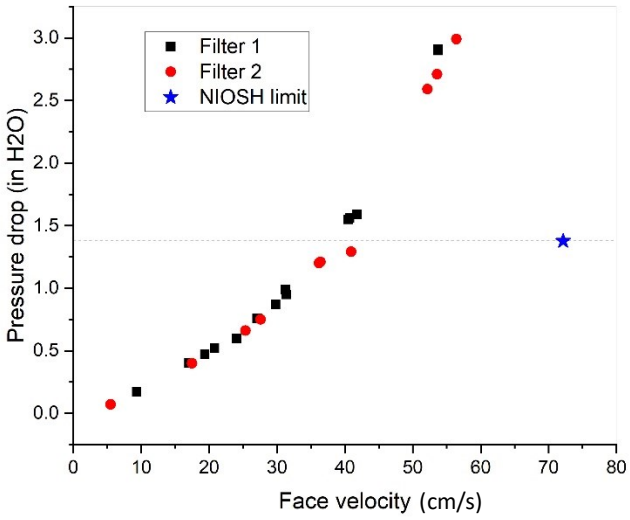

Figure B- 5 Pressure drop over filter 1 and 2 compared to NIOSH limit

Leakage or penetration through the face/mask interface is another important index that should be considered along with the penetration due to the efficiency[249]. Total inward leakage is measured for 6 alternative masks using two manikin shapes in Figure B- 6. Figure B- 6a and b demonstrate TIL and quality factor using manikin A. In comparison with N95, 3 tested masks have a good fitting with manikin face, due to a wider contact area between mask and manikin face. Total inward leakage is less than 10 % for all masks, while the N95 mask has 40% leakage with this manikin. The penetration through M1 and M2 is less than 2 % for particles larger than 1 μm. It can be observed that M1 and M2 provide better fitting with the manikin A in comparison with M3. Lower pressure drop due to the loose-fitting of M3 causes higher quality factor for this mask. Therefore, mask M3 has better performance due to the lower pressure drop and lower total inward leakage.

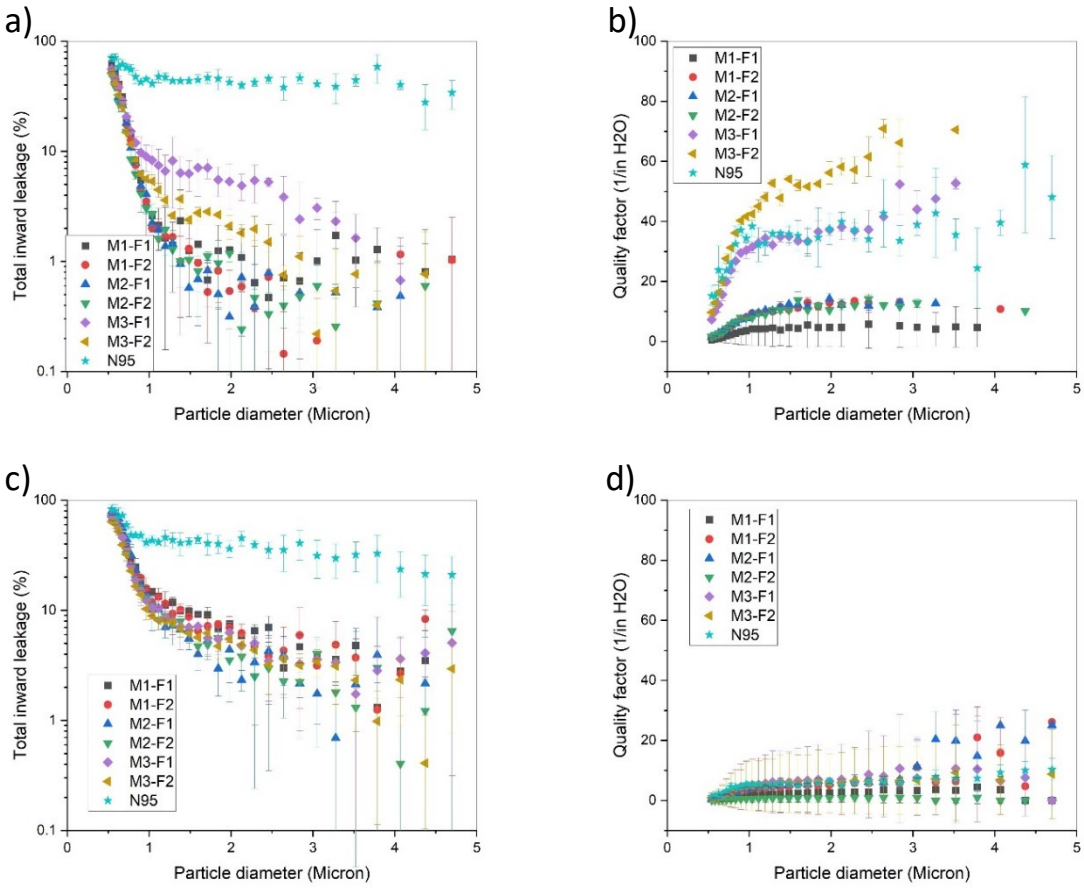

Figure B- 6 Measured a) total inward leakage and b) quality factor with manikin A and c) total inward leakage and d) quality factor with manikin B for combinations of 3 masks with 2 filters

Figure B- 6c and d demonstrate total inward leakage and quality factor of 6 alternative masks using manikin B. As shown in Figure B- 6 C, the TIL of all alternative masks are similar and less than 10%. By comparing the performance of alternative masks in manikin A with the one in manikin B, it can be inferred that the TIL is less than 10 % with both manikins, however, the M3 has a higher quality factor with manikin A due to the pressure drop. The manikin A has a slimmer face comparing to the manikin B which leads to loose-fitting with the face.

Generally, the thickness of the face/mask interface for the alternative masks is much more than the N95 mask, thus leakage is much lower in measurements. New mask design with face/mask interface similar to the alternative masks and a larger filter area than those used in this study, can improve the leakage and pressure drop through the filter area.

B.4.2 Effects of brace on the performance of N95 masks

The effects of brace on the performance of the N95 mask is investigated in Figure B- 7. The total inward leakage of the N95 mask is compared to the N95 tightened with a (Figure B- 7a). The TIL is due to the penetration through the face/mask interface as well as penetration through the filter. It can be observed that TIL is up to 30 % improved by using the brace. Improved TIL caused by brace is not size dependant; the line of total inward leakage is shifted upward using the brace. The optimized size of brace for different head shapes may lead to lower leakage values. By using the brace, the protection factor (reverse of leakage) can reach 10, which is acceptable by OSHA. Due to the better fitting, the pressure drop over filter is increased, however, the quality factors improved, as shown in Figure B- 7b. This result may shed light on the significant role of the brace to be approved by NIOSH or Food and Drug Administration (FDA) [265].

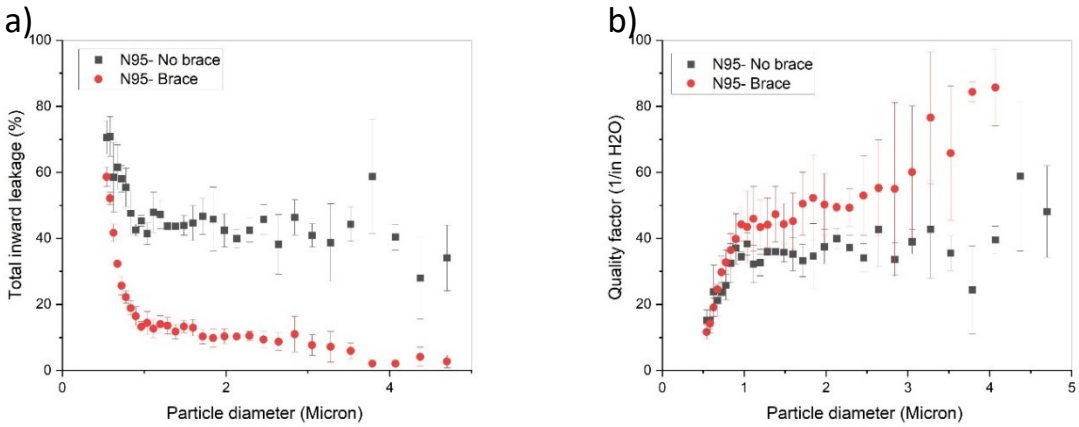

Figure B- 7 a) Total inward leakage and b) quality factor for N95 mask and N95 tightened with a brace

B.4.3 Effect of UV treatment on the performance of N95 masks

The effect of single-cycle UV treatment as one of the disinfection methods on filter performance is investigated in this section. Filtration efficiency and quality factor of N95 and UV treated N95 are compared in Figure B- 8. As shown in Figure B- 8a, less than 1.5 % filtration efficiency reduction is observed with the UV treated N95. The filtration efficiency of UV treated N95 to capture 45 nm particles is 1.5 % lower than N 95. Frequent treatment may cause a drastic reduction in filtration efficiency.

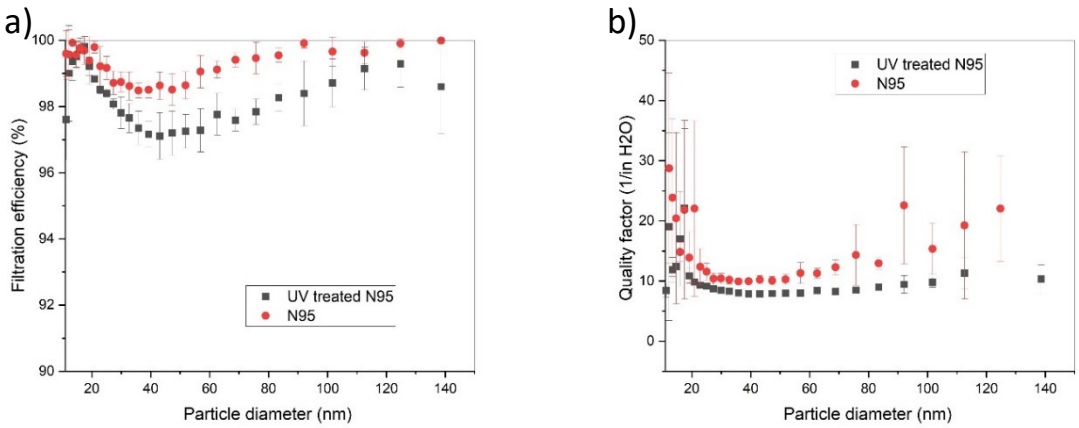

Figure B- 8 a) Filtration efficiency and b) quality factor of N95 and UV treated N95

The pressure drop over filter for N95 and UV treated N95 is shown in Figure B- 9 for a wide range of inhalation flow rates from 30 LPM (light work) to 85 LPM (heavy work)[268]. Considering 195 cm^2 mask surface area, 30-85 LPM corresponds to 2.564 to 7.265 cm/s face velocity. Single-cycle UV treatment does not change the structure of filter and subsequent pressured drop. The quality factor of N95 is compared with the one in UV treated N95 in Figure B- 8.b. The effect of UV treatment on the pressure drop is not significant and higher quality factor with non-treated N95 is due to the higher filtration efficiency.

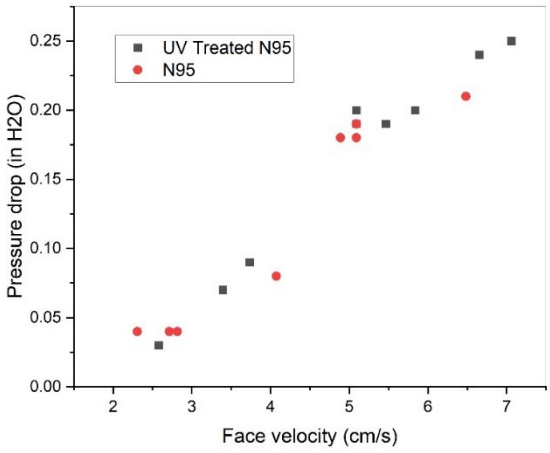

Figure B- 9 The pressure drop of N95 and UV treated N95 masks

The total inward leakage of the UV treated N95 mask is compared to the N95 in Figure B- 10. In both cases, the brace is used. Less than 10 % reduction in the total inward leakage in UV treated N95 mask is observed. Frequent treatment may cause a drastic reduction in total inward leakage.

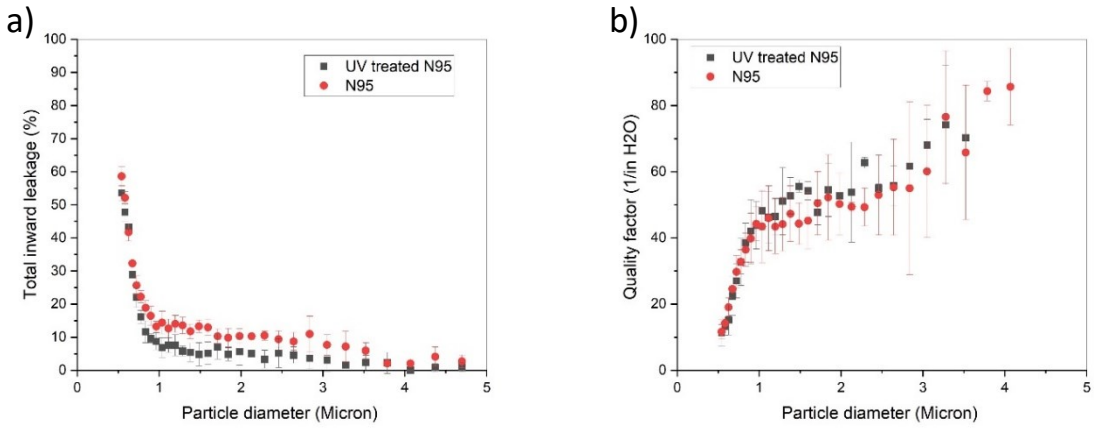

Figure B- 10 a) Total inward leakage and b) quality factor for N95 and UV treated N95 masks

B.5 Conclusions

In the present study, the measured total inward leakage of the alternative masks is less than 10%. The total inward leakage of the alternative masks is much higher than the N95 mask on manikins, due to their larger thickness of the face/mask interface, however, the pressure drop exceeds NIOSH limit in high flow rates or heavy work. New mask design with face/mask interface similar to the alternative masks and a larger filter area than those used in this study, may improve the leakage and pressure drop through the filter area.

It was observed that TIL is improved by using the brace up to 30 %. The optimized size of brace for different head shapes may lead to lower leakage values. Using the brace the protection factor (reverse of leakage) can reach 10, which is acceptable by OSHA. This result may shed light on the significant role of the brace to be approved by NIOSH or FDA [265].

The filtration efficiency of UV treated N95 to capture 45 nm particles is 1.5 % lower than N 95. Moreover, Less than 10 % reduction in the total inward leakage in UV treated N95 mask is observed. Frequent treatment may cause a drastic reduction in filtration efficiency. Single-cycle UV treatment does not change the structure of filter and subsequent pressured drop.